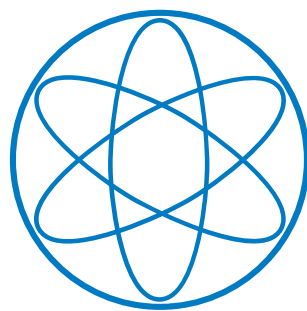


FAKULTÄT FÜR PHYSIK  
DER TECHNISCHEN UNIVERSITÄT MÜNCHEN

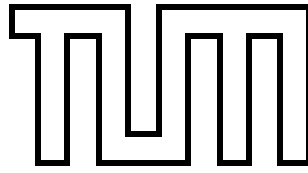
Condensed Matter & Many-Body Theory

# **Many-Body Physics with Circuit Quantum Electrodynamics**

Martin H. Leib







# FAKULTÄT FÜR PHYSIK

DER TECHNISCHEN UNIVERSITÄT MÜNCHEN

Lehrstuhl für Theoretische Physik (T34)-Vielteilchenphänomene

## Many-Body Physics with Circuit Quantum Electrodynamics

Martin H. Leib

Vollständiger Abdruck der von der Fakultät für Physik der Technischen Universität München zur Erlangung des akademischen Grades eines Doktors der Wissenschaften genehmigten Dissertation.

Vorsitzender: Univ.-Prof. Dr. Rudolf Gross

Prüfer der Dissertation : 1. Prof. Dr. Michael J. Hartmann  
Heriot Watt University, Edinburgh / UK  
2. Univ.-Prof. Dr. Wilhelm Zwerger

Die Dissertation wurde am 18.03.2015 bei der Technischen Universität München eingereicht und durch die Fakultät für Physik am 15.04.2015 angenommen.



---

## Publication List

Below is the complete list of publications that have been published in peer reviewed journals during the course of the doctoral thesis at hand. Publications [9] and [8] deal with the simulation of Bose-Hubbard physics with superconducting circuits and are covered in chapter 5 and section 6.3 respectively. Publication [5] is a follow up to publication [8] which deals with the coupling between sites and is covered in the same section 6.3. Publications [4] and [3] deal with the nonlinear coupling between sites either for the simulation of many-body physics (c.f. publication [3]) or the implementation of an entangling gate for itinerant microwave photons (c.f. publication [4]). The nonlinear coupling mechanism underlying both of these publications is presented in chapter 7 combined with brief introductions to the specifics of the publications. Publication [1] is a follow-up to publication [3]. And finally publication [2] deals with the coplanar waveguide intersected by many Josephson junctions and its driven-dissipative dynamics. This publication is covered in section 6.4. The diagonalization-techniques of publications [8] and [3] have been proven to be unifiable. Therefore their treatment has been unified in hindsight in section 6.1.

Publications [6] and [7] deal with the ultrastrong coupling in circuit QED and therefore deviate from the underlying theme of many-body physics in circuit QED systems. For the sake of consistency they are omitted in this thesis

- [1] *“Steady-state phase diagram of a driven QED-cavity array with cross-Kerr nonlinearities”* Jiasen Jin, Davide Rossini, Martin Leib, Michael J. Hartmann and Rosario Fazio **PRA** 90 023827
- [2] *“Synchronized Switching in a Josephson Junction Crystal”* Martin Leib and Michael J. Hartmann **PRL** 112 223603
- [3] *“Photon solid phases in driven arrays of non-linearly coupled cavities”* Jiasen Jin, Davide Rossini, Rosario Fazio, Martin Leib and Michael J. Hartmann **PRL** 110 163605
- [4] *“A Quantum Single Photon Transistor in Circuit Quantum Electrodynamics”* Lukas Neumeier, Martin Leib and Michael J. Hartmann **PRL** 111 063601
- [5] *“Many Body Physics with Coupled Transmission Line Resonators”* Martin Leib and Michael J. Hartmann **Phys. Scr.** 2013 014042

- 
- [6] *“Thermal emission in the ultrastrong coupling regime”* A. Ridolfo, Martin Leib, S. Savasta and Michael J. Hartmann **Phys. Scr.** 2013 014053
- [7] *“Photon Blockade in the Ultrastrong Coupling Regime”* Alessandro Ridolfo, Martin Leib, Salvatore Savasta and Michael J. Hartmann **PRL** 109 193602
- [8] *“Networks of nonlinear superconducting transmission line resonators”* Martin Leib, Frank Deppe, Achim Marx, Rudolf Gross and Michael J. Hartmann **New J. Phys.** 14 075024
- [9] *“Bose-Hubbard dynamics of polaritons in a chain of circuit QED cavities”* Martin Leib and Michael J. Hartmann **New J. Phys.** 12 093031

---

## Acknowledgments

I want to thank Michael Hartmann for his supervision of the Phd thesis at hand. He was always there for my questions and helped me in every possible way. My colleagues Peter Degenfeld and Simon Rips contributed as well to this work and I highly appreciate the discussions about physics with them as well as the simple fun we had together. I want to thank Arne Kordts and especially Lukas Neumeier for constantly questioning the foundations of my knowledge. They solidified my knowledge about physics and unpretentiously revealed the voids in it. I also want to thank my brother and my parents for supporting me in any way possible. And last but not least I want to thank Vroni for being the tower of strength in my life, taming my chaotic style and making me want to be better today than I was yesterday.

---



# Contents

<b>Publication List</b>	<b>v</b>
<b>Acknowledgements</b>	<b>vii</b>
<b>Outline of the Thesis</b>	<b>xi</b>
<b>I. Principles of circuit QED</b>	<b>1</b>
<b>1. Historical Introduction</b>	<b>3</b>
1.1. Macroscopic Coherence . . . . .	3
1.2. Quantum Information Processing with Superconducting Qubits . . . . .	4
1.3. Quantum Optics with Superconducting Circuits . . . . .	6
1.4. Many-Body Physics with Superconducting Circuits . . . . .	8
<b>2. From Maxwell to Kirchhoff</b>	<b>9</b>
2.1. Plane Wave Propagation in Axially Symmetric Media . . . . .	11
2.2. TEM Wave Propagation . . . . .	11
2.2.1. Lumped Element Representation . . . . .	13
2.3. TE/TM Wave Propagation . . . . .	15
2.4. Planar Transmission Lines . . . . .	16
2.4.1. Low Frequency Solutions . . . . .	18
<b>3. Lumped Element Circuits</b>	<b>21</b>
3.1. Hamiltonians of Electrical Circuits . . . . .	21
3.1.1. Energy of Capacitive and Inductive Branches . . . . .	21
3.1.2. Spanning Tree and Node Fluxes . . . . .	25
3.2. Boundary Conditions . . . . .	28
3.3. Transfer Matrix Picture . . . . .	32
<b>4. Quantization of Electrical Circuits</b>	<b>37</b>
4.1. LC Oscillator . . . . .	38
4.2. Coplanar Waveguide Resonator . . . . .	39
4.3. Charge Qubit . . . . .	41
4.3.1. Transmon . . . . .	45
<b>II. Many-Body Physics in circuit QED</b>	<b>47</b>

<b>5. Bose Hubbard Physics with circuit QED Arrays</b>	<b>51</b>
5.1. Transmon-QED and the Bose-Hubbard Model . . . . .	51
5.1.1. The full Hamilton operator . . . . .	51
5.1.2. Approximations to single-site terms . . . . .	52
5.1.3. Approximations to couplings between resonators . . . . .	53
5.1.4. The polariton modes . . . . .	54
5.1.5. Validity of the approximations . . . . .	56
5.2. Polariton statistics in the driven dissipative regime . . . . .	59
5.2.1. Polariton density . . . . .	61
5.2.2. Density-density correlations . . . . .	63
5.2.3. Meanfield approximation for two coupled modes with small nonlin- earity . . . . .	69
<b>6. Josephson Junction Intersected Resonators</b>	<b>71</b>
6.1. Model Assumptions for the Josephson Junction Intersected Resonator . . . . .	71
6.2. Spectrum Calculation with Transfer Matrix Technique . . . . .	73
6.3. Single Josephson Junction . . . . .	76
6.3.1. Spectrum . . . . .	78
6.3.2. Derivation of the Kerr-nonlinearity . . . . .	79
6.3.3. Experimental limitations and prerequisites . . . . .	82
6.3.4. Networks . . . . .	83
6.4. Multiple Josephson Junctions . . . . .	86
6.4.1. Spectrum . . . . .	86
6.4.2. Quantisation . . . . .	89
6.4.3. Degeneracy Point . . . . .	92
6.4.4. Driven Dissipative Dynamics . . . . .	95
6.4.5. Experimental Parameters . . . . .	98
<b>7. Nonlinear Coupling</b>	<b>101</b>
7.1. Cross-Kerr Nonlinearities . . . . .	103
7.2. Quantum Single-Photon Transistor . . . . .	107
<b>8. Outlook</b>	<b>111</b>
8.1. Future directions of circuit quantum electrodynamics . . . . .	111
8.2. Quantum Graph models and Transfer Matrices . . . . .	112
<b>Bibliography</b>	<b>115</b>

# Outline of the Thesis

## **Part I: Principles of Superconducting Circuits**

### CHAPTER 1: HISTORICAL INTRODUCTION

This chapter presents an historical overview of the past 20 years since the beginning of the research in coherent superconducting circuits. It is written for the historically interested reader who is already familiar with the concepts of superconducting circuits.

### CHAPTER 2: FROM MAXWELL TO KIRCHHOFF

Here we present the approximations that are necessary to reduce the theoretical description of the three-dimensional electrodynamical problem to electrical circuits.

### CHAPTER 3: LUMPED ELEMENT CIRCUITS

In chapter 3 we present methods to find the Hamiltonian description of electrical circuits in terms of independent variables.

### CHAPTER 4: QUANTIZATION OF ELECTRICAL CIRCUITS

In the last chapter of the first part of the thesis we present the implications of the quantization of electrical circuits.

## **Part II: Many-Body Physics with Superconducting Circuits**

### CHAPTER 5: BOSE-HUBBARD PHYSICS WITH CIRCUIT QED ARRAYS

In chapter 5 we present our proposal for a simulator of Bose-Hubbard Physics of a array of resonators each coupled to a transmon qubit

### CHAPTER 6: JOSEPHSON JUNCTION INTERSECTED RESONATORS

In chapter 6 we examine resonators that are intersected by Josephson junctions. These resonators give rise to a alternative realization of a simulator of Bose-Hubbard physics as well as a novel synchronization phenomenon

### CHAPTER 7: NONLINEAR INTERACTIONS

In the last chapter we present a coupling scheme involving Josephson junctions. This coupling scheme enables the engineering of cross-Kerr and assisted tunneling terms.



**Part I.**

**Principles of Circuit Quantum  
Electrodynamics**



# 1. Historical Introduction

## 1.1. Macroscopic Coherence

The interest in coherent superconducting electronics began to rise in the early to mid 80s as a testbed for the theoretical idea of macroscopic coherence. The apparent differences between the laws of quantum mechanics and our personal experience in the “classical” world had already inspired the famous thought experiment of Schrödinger and his cat. However Schrödingers cat is only the distillate of the unbridgeable gap between the “quantum” and the “classical” world and does not show a path out of the quandary. One possible way to marry the “quantum” and the “classical” world would be a superior theory that reduces to the laws of quantum mechanics and classical physics in circumstances where the respective validity is empirically established. This however immediately implies the existence of a transition area where the superior theory supposedly reveals itself. That is why physicists began the search for ever increasingly large objects that show “intuition defying” quantum mechanical effects. Which quantum mechanical effects we consider to be “intuition defying” is in itself an open question. One would not consider the existence of an insulator however large it may be as “intuition defying” even though we use quantum mechanical principles to understand its existence. This interesting question has been addressed most prominently by Leggett (e.g. [51]). The search for macroscopic objects that show quantum mechanical effects inevitably led to superconductivity with its macroscopic number of Cooper pairs condensed into a single state. First experiments considered the current biased Josephson junction with its tilted washboard potential for the phase difference between the two sides of the junction. The Josephson junction is initialized in a zero voltage state in one of the metastable minima of the washboard potential. Depending on the temperature, the Josephson junction can either tunnel out of the minimum or is thermally excited and leaves the minimum and the Josephson junction switches to the finite voltage state ( e.g. [87]). The zero voltage and finite voltage state are macroscopically distinct states and the mechanism of transition between the two can be seen to be classical for thermal excitation or quantum mechanical for low temperatures where quantum mechanical tunneling is the dominant channel for relaxation. Two of the main players of circuit quantum electrodynamics nowadays, John Martinis and Michel Devoret, also entered the stage of superconducting electronics as leading authors on a publication concerning macroscopic quantum tunneling (cf. [18]).

Another possible way out of the quantum-classical conundrum would be if quantum mechanics itself is the superior theory that reduces to the laws of classical mechanics in appropriate situations. Dissipation is thought to be the key factor that drives the quantum to classical transition. That macroscopic objects seem to behave classical might be a consequence of the interaction with the many degrees of freedom of the environment. The seminal paper of Caldeira and Leggett which addresses the quantum mechanical description of dissipation in the framework of quantum mechanics (cf.[13]) was specially tailored

to describe the tunneling in the current biased Josephson junction.

Experiments with superconducting circuits quickly moved on to precursors of the charge qubit (e.g. [65]) where the anticrossing of different charge states were probed spectroscopically. Instead of probing the charge states, which only differ by one Cooper pair and may therefore again be called only microscopically distinct, one considered the flux trapped by a superconducting ring interrupted by Josephson junctions as a macroscopical observable. For certain values of the external flux threaded through the superconducting ring the experiments showed an anticrossing implying a superposition of macroscopical large currents flowing clockwise and anti-clockwise in the superconducting ring. The superconducting rings used in these experiments (e.g. [85, 30]) were precursors of the current flux qubits used for example in the state of the art quantum annealing processor of D-Wave (e.g. [44]). Up to this point, all experiments involved spectroscopical measurements, the first time-resolved experiments were performed at a reiteration of the current biased Josephson junction (cf. [61]) where the authors observed Rabi oscillations between two metastable states in the washboard potential of the current biased Josephson junction. The setup which came to be known as phase qubit had the big advantage of a built-in readout. For readout a current pulse would tilt the washboard potential increasingly to get a high probability for the excited qubit state to tunnel out and leave the Josephson junction in the finite voltage state which could be read out with a superconducting quantum interference device (SQUID) magnetometer because the Josephson junction was embedded in a loop. The very high confidence at that time in the capabilities of superconducting circuits is perfectly shown in the last sentence of the abstract which states that the “qubit circuit is the basis of a scalable quantum computer”. Up to this time it is not clear if this is actually true, although the charge qubits, in the variety of the transmon, seem to be in the lead for the race to a fully scalable quantum computer due to their quantum non-demolition readout and excellent coherence properties.

However this last sentence in the abstract already anticipates one of the main directions of research for superconducting electronics: the implementation of the DiVincenzo criteria (cf. [22]) in superconducting electronics.

## 1.2. Quantum Information Processing with Superconducting Qubits

The first hurdle to be taken on the way to the superconducting quantum computer was to increase the overall performance and precision of gates for individual superconducting qubits. The NEC group from Japan managed to generate deterministically superpositions between different charge states with non-adiabatic gate voltage sweeps (cf. [66]). Readout was performed through a highly resistive probe junction which in turn limited the coherence of the charge qubit. Since then many improvements have been made to the individual qubits, most prominently the operation of the charge qubit in the phase regime, the transmon qubit (cf. [48]). Additionally new qubit circuits were invented, which should overcome the shortcomings of the standard qubits (phase-, flux- and charge qubits) while maintaining their strengths, like the Quaronium (cf. [86]), Fluxonium (cf. [58]) and a superconducting qubit with hard-wired topological protection (cf. [32]).

As a next step interaction between two superconducting qubits was established. At first



charge- (at the RIKEN, Japan institute cf.[72]) and phase-qubits (at University of Maryland cf.[6]) were coupled together because they can be coupled with a simple capacitive coupling. Because of the advances in measurement technology, time resolved measurements of the excitations oscillating back and forth between the qubits could be performed. Coupling flux qubits together took about two years longer with the theoretical proposal in 2004 (cf. [74]) and its experimental realization in 2005 by the Delft group (cf. [57]). Two flux qubits are coupled inductively with a SQUID loop encircling both qubits. By current biasing the coupling SQUID one can change the coupling strength which can not be done with the hard wired capacitive coupling. The D-wave chip still uses this kind of SQUID, inductive, coupling between its qubits. The RIKEN group in Japan circumvented the restriction with the constant capacitive coupling by tuning their charge qubits in and out of resonance. This way they could switch on and off the exchange of excitations between the qubits and thereby implement conditional gate operations. The same level of control was shown four years after that in a flux qubit setup with constant coupling and constant qubit frequencies (cf. [73]). The gate was implemented by sequentially driving transitions in the two-qubit system with suitably tuned microwave radiation.

The watershed moment in the history of superconducting electronics had already happened by then. In 2003 a cavity quantum electrodynamics architecture (QED), with a charge qubit acting as an atom and an microwave resonator acting as a cavity had been proposed as an building block for quantum information processing (cf. [91] and a year later with a 1-d instead of a 3-d resonator cf. [9]). A year later this was realized by a group at yale university (cf. [89]) for a charge qubit coupled to a microwave resonator. At the same page in the magazine "nature" before this aforementioned publication there is a considerably less well known publication implementing the cavity QED paradigm with a flux qubit coupled to a superconducting harmonic oscillator realized by a joint effort of groups in Delft and at NTT and NEC in Japan. The big success of the superconducting electronics version of the cavity QED paradigm which came to be known as circuit QED is rooted in the large dipole moment of the charge qubit and the small mode volume of a coplanar waveguide resonator. The figure of merit in a cavity QED setup is the cooperativity  $g^2/(\gamma\kappa)$ , the ratio of the coupling between atom and cavity squared and the product of the decay rates of the atom  $\gamma$  and the cavity  $\kappa$ . While the decay rates of the superconducting qubit and the resonator are held considerably low because of the superconducting gap, the coupling can be extremely high for charge qubits and coplanar waveguide resonators. The coupling is proportional to the product of the dipole moment of the charge qubit and the zero point field fluctuation of the resonator which is in turn inversely proportional to the mode volume of the resonator. The one-dimensional coplanar waveguide resonator features an exceptionally small mode volume especially compared to the three-dimensional cavities used in conventional cavity QED. An interesting side note though is that 3-d resonators have been reintroduced sometimes nowadays because of their better isolation from the electrodynamic environment. The loss in zero point field fluctuation because of the larger mode volume is compensated with the further increase of the dipole moment of the coupled charge qubit (cf. [71]).

The circuit QED architecture while not being particularly related to quantum information processing still enabled the implementation of prerequisites for quantum computation with superconducting qubits. The strong coupling limit of cavity QED  $g^2/(\kappa\gamma) \gg 1$  could be easily reached in circuit QED setups. Another way of defining the strong coupling

limit is to say that the joint excitation of atom and cavity, the upper and lower polariton, should be well separated in a spectral measurement. The cooperativity in circuit QED setups however can be as strong as to be able to separate peaks in the spectrum for different eigenenergies of the joint Hamilton operator for detuned charge qubit and coplanar waveguide resonator. The coplanar waveguide resonator resonance is shifted by a multiple of its linewidth upon a change between the two computational states of the charge qubit. This “strong dispersive coupling”- regime enables a readout of the charge qubit which measures the phase of the reflection or transmission of a microwave signal driving the coplanar resonator (cf. [88]). This measurement technique enables a quantum non-demolition readout of the charge qubit which is a required prerequisite to perform quantum error correction. The resonator while being a readout device provides protection from the electromagnetic environment at the same time. Further refinements of this measuring technique involved the utilization of slightly nonlinear resonators (cf. [80]) for increased visibility. The same technique has also been adapted for flux qubits with the readout SQUID acting as nonlinear readout resonator (cf. [55]). But the coplanar waveguide resonator is not only useful as a readout device and protection from the electromagnetic environment but is also used to couple remote superconducting qubits. Two charge qubits have been coupled dispersively to a resonator that interact via virtual excitations of the resonator (cf. [56]). The qubits were coupled dispersively to the resonator to prohibit loss through the resonator. The resonator loss was due to its strong coupling to the readout circuitry. This restriction does not apply if one tries to couple two phase qubits that are coupled capacitively to a coplanar waveguide resonator (cf. [82]). In this setup the resonator actually has a higher resilience against decay as the phase qubits and excitations are transferred between the qubits through non-virtual population of the resonator. Measurements are performed with the phase qubits own readout circuitry.

### 1.3. Quantum Optics with Superconducting Circuits

The huge success of the circuit QED architecture not only brought up quantum information processing applications but also gained interest in the quantum optics community which quickly adopted superconducting electronics as a testbed for multiple quantum optics phenomena. As a first example we mention the implementation of a circuit QED architecture with a flux qubit which is coupled ultrastrongly to the coplanar waveguide resonator (cf. [67]). While still being related to the quantum optics paradigm of cavity QED it extends the range of coupling between atom and cavity beyond any attainable range in “classical” quantum optics setups with atoms in cavities for photons in the visible frequency range. This was made possible by a conducting link between flux qubit and coplanar waveguide resonator. The spectrum of the combined setup showed effects beyond the generic rotating wave approximation of the Jaynes Cummings model.

Instead of controlling the state of the superconducting qubit in a circuit QED setup one reversed the scope to generate highly non-classical states in the coplanar waveguide resonator with the help of the superconducting qubit. Fock states up to six microwave photons (cf. [37]) were generated and a microwave source with deterministic, on-demand release of itinerant single photon pulses was implemented (cf. [38]). In the spirit of the beginnings of coherent superconducting electronics, the foundations of quantum mechanics

were again tested. The group at UCSB showed the violation of the Bell inequalities with two phase qubits coupled through a resonator (cf. [3]). One year later the Yale group build a circuit QED setup with four Transmon qubits and showed three qubit entanglement (cf. [20]). The entangling gates were implemented with the help of non-computational states of the Transmon qubit and joint readout was performed by the dispersively coupled common resonator. A group in Paris succeeded in showing the violation of a Leggett Garg inequality. While the violation of a Bell type inequality shows the unique quantum correlations in space, a violation of a Leggett Garg inequality shows unique quantum correlations in time. A oscillating single degree of freedom, rabi oscillations in a Transmon qubit, is measured at successive times and shows the “state collapse” characteristics unique to the measurement postulate of quantum mechanics.

Instead of coupling the superconducting qubit to a resonator one could also couple the superconducting qubit to a infinite coplanar waveguide. Microwaves impinging on a flux qubit would excite the qubit which in turn reemits into the coplanar waveguide which is known as resonance fluorescence (cf. [4]). Superconducting qubits are not restricted to their computational states and the design flexibility allows for almost arbitrary energy level schemes. In addition to the above mentioned resonance fluorescence phenomenon also the Autler-Townes effect in a three level phase qubit has been measured (cf. [81]). And electromagnetically induced transparency has been shown in a flux qubit circuit with a ladder type energy level scheme (cf. [1]).

In the last five years a couple of hybrid structures emerged combining the power of superconducting electronics with another technology. One upcoming trend for hybrid systems is the combination with mechanical oscillators. These microelectromechanical systems (MEMS) combine for example a phase qubit with a small mechanical drum made out of piezoelectric material (cf. [70]). The oscillation of the drum generates electrical pulses that can couple to the phase qubit. The mechanical drum had an eigenfrequency in the microwave regime which enabled the cooling to the mechanical groundstate just by embedding the drum in the superconducting chip that is cooled in the dilution refrigerator. The phase qubit was used to detect and manipulate the state of the mechanical drum. A beam oscillating at radio-frequency could be cooled close to its groundstate by coupling it to a superconducting resonator. The smaller oscillation frequency, compared to the drum, prohibits the cooling to the ground state by conventional refrigeration techniques. However by driving the superconducting resonator slightly red-detuned, the resonator tends to extract excitations from the oscillating beam, thereby cooling it. Superconducting circuits also have been coupled successfully to electron spins in nitrogen vacancy centers in diamond (cf. [49]) and electron spins in ruby (cf. [79]). The main interest for research in this direction is to combine the record breaking coherence times of solid state spin qubits as a quantum memory with the flexibility in quantum information processing of superconducting qubits.

The connections between quantum optics and superconducting electronics goes well beyond the mapping of atoms to superconducting qubits and cavities to coplanar waveguide resonators, which is perfectly shown in the case of the dynamical casimir effect. The dynamical casimir effect is the generation of photons by an acceleratedly moving mirror in free space. The observation of the dynamical casimir effect is very difficult since the mirror has to be moved at speeds close to the speed of light in free space, which is challenging for a massive object like a mirror. The speed of microwaves traveling along a coplanar

waveguide is very close to the speed of light in free space. However the implementation of a moving mirror in superconducting electronics has proven to be considerably simpler than a massive mirror for optical frequencies. A half infinite coplanar waveguide terminated in a variable flux threaded SQUID has been proposed as the analog of a half infinite vacuum terminated by a moving mirror (cf. [42]). By varying the flux threaded through the loop, the “mirror” at the end starts to move, enabling very high speed movement of one of the boundary conditions of the half infinite vacuum represented by the half infinite coplanar waveguide. In 2011 a group Chalmers university succeeded in measuring the photons generated by the moving SQUID “mirror” (cf. [90]).

### 1.4. Many-Body Physics with Superconducting Circuits

Circuit QED is currently on the verge of crossing the border between few- to many body physics [39]. The well established building blocks of superconducting qubits and resonators are coupled capacitively, inductively or both to form larger systems [84]. This opens up a exciting realm of completely new physical phenomena. The truncation of the microscopic Hamilton operators for the basic building blocks of coherent superconducting circuits to generic model Hamilton operators like harmonic oscillators and two-level systems is very well established quantitatively. In the near future experimental setups will combine these building blocks with coupling strengths small enough not to invalidate the approximations made for the building blocks. Combined with the design flexibility in their spatial arrangement and coupling, these systems are the ideal experimental platform to simulate almost arbitrary generic Hamilton operators. We propose two setups to simulate Bose-Hubbard physics with the generic exchange interaction between the sites, c.f. chapters 5 and 6. Additionally we propose a coupling scheme to expand the coupling toolbox to nonlinear interactions, c.f. chapter 7.

These capabilities immediately place superconducting circuits into a class with quantum simulators of cold atoms in optical lattices and ions in penning traps. Compared to these systems composed of single atoms, the superconducting circuits that are composed of a macroscopic number of atoms are subject to stronger influence of the fluctuating environment. Two level-defects in the dielectric substrate and spins trapped on the surface of the chip degrade the coherence and have to be taken into account in the theoretical models. Therefore the dynamics of microwave excitations in superconducting circuits is a ideal testbed for non-equilibrium physics rather than the simulation of groundstate-phase transitions as done with cold atoms in optical lattices. Subject to a coherent injection of microwave photons, by a coherent microwave drive, and subsequent dissipation of microwave photons due to the coupling to the environment, steady states emerge that show reminiscences of the underlying groundstate phase transition, c.f. sections 5.2 and 6.4.

## 2. From Maxwell to Kirchhoff

This entire chapter is devoted to the path from a full electromagnetic field description of microwave circuits governed by the Maxwell equations to a description in terms of electrical circuits governed by the Kirchhoff rules. A electrical circuit description of a given setup encompasses a network representation consisting of an arbitrary amount of nodes connected by edges. Each edge represents a two terminal device. In our work we deal with three different kinds of two-terminal devices: capacitors, inductors and Josephson junctions. Every two-terminal device is characterized by a unique relationship between the current flowing through the device  $I$  and the voltage difference at its two outlets  $V$ . These relationships together with the Kirchhoff rules form a complete set of equations of motion for the currents and voltage drops across all two-terminal devices in the electrical circuit. This modular architecture of the theory entails the great advantage of flexibility. Once all the relationships for the two terminal devices are known, which often affords a description of the two-terminal device in terms of electromagnetic fields, we can quickly combine these building blocks with arbitrary complexity without having to solve for the electromagnetic fields of the whole electrical circuit again.

Kirchhoff rules however strictly only apply in static situations. They are consequences of the continuity equation of electrical charge:  $\nabla \vec{J} + \partial_t Q = 0$  with current-  $\vec{J}$  and charge density  $Q$ . If you consider the node of a electrical circuit, integrate the continuity equation in a sphere which is small enough to only include the node and neglect temporary accumulation of charge on the node, we come up with the first Kirchhoff rule:  $\sum_{k \in \text{node}} I_k = 0$ , the sum of all currents flowing to the node of a electrical circuit vanishes. This is valid as long as the characteristic timescale for changes in the current is not fast enough to introduce charge accumulation on the node. We can circumvent however this difficulty by introducing an additional capacitor connected to ground for the node. For the second Kirchhoff rule it is more challenging to push the high frequency limit. For the second Kirchhoff rule we integrate  $\nabla \times \vec{E} = -\mu \partial_t \vec{H}$  over a surface framed by a mesh of the electrical circuit. If we again neglect the temporal accumulation of flux threaded through the mesh we come up with the second Kirchhoff rule:  $\sum_{k \in \text{loop}} V_k = 0$ , the sum of all electrical voltage drops around every loop of the electrical circuit is zero. Lets suppose our circuit oscillates with frequency  $\omega$  in a steady state. Then the integral over the curl of the electric field can be approximated to  $\int_S \partial_t \vec{H} \leq S \omega \text{Max}_S(|\vec{H}|) = S 2\pi/\lambda \text{Max}_S(|\vec{H}|)$ , with  $S$  the surface framed by the mesh and  $\lambda$  the wavelength. In other words: the second Kirchhoff rule is applicable, if the physical size of the electrical circuit is small compared to the wavelength of the excitations of the circuit.

A typical low-frequency ( $\approx 30\text{MHz}$ ) resonating circuit consists of a inductor coil and a parallel plate capacitor. If we reduce the size of the whole device by a factor of 100 we would multiply the eigenfrequency by the same factor. The internal damping rate, measured in units of the eigenfrequency, of the wiring of the resulting microwave resonating circuit would however increase 10-fold. If we instead reduce the number of turns in the coil

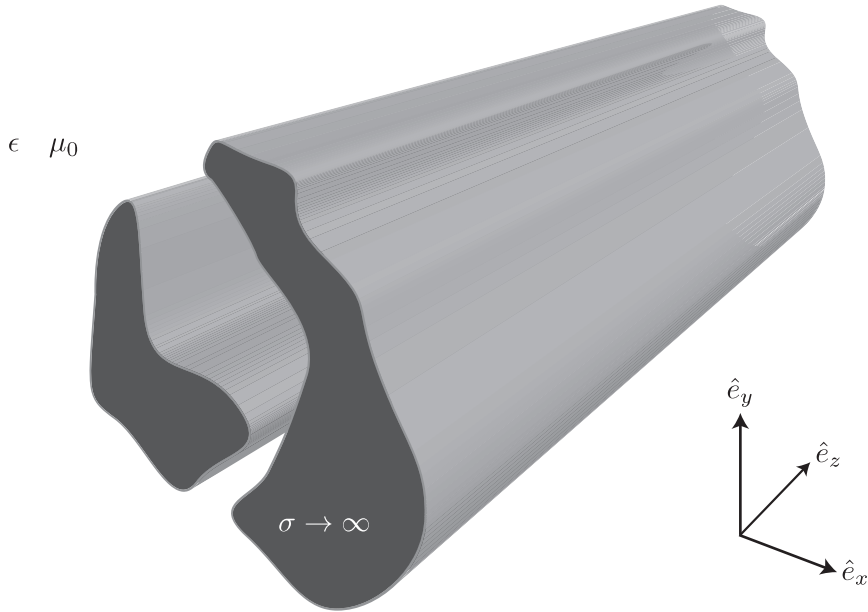


Figure 2.1.: Transmission line setup. Two axially symmetric conductors in a linear isotropic dielectric with scalar permittivity  $\epsilon$  and scalar permeability  $\mu$

and increase the distance of the parallel plate capacitor, while leaving the dimension of the wiring untouched, we end up with a hairpin-shaped circuit, resonating in the microwave regime with approximately unaltered internal damping rate. The resulting electrical circuit however would be of the size of the wavelength of the microwaves itself. Two main differences compared to low-frequency circuits will arise from this. Firstly the circuit will start acting as an antenna and if we do not provide some means of shielding the circuit there will be considerable radiative loss. Secondly the concept of inductors and capacitors as physical and separated objects will fade and be replaced by a means to symbolically represent much more complicated structures where a physical object can be inductor and capacitor at the same time. To find the requirements for the existence of these symbolical representations is the purpose of this chapter.

Circuit QED setups typically consist of two different types of structures: coplanar transmission lines and lumped element structures. While the coplanar transmission lines are comparable to the wavelength, the lumped element structures like Josephson artificial atoms, coupling capacitors or Josephson junctions are considerably smaller than the wavelength. For the latter the low-frequency concepts do apply but the open transmission lines and transmission line resonators do need a special treatment. As it turns out the axial symmetry and the shielding by the groundplane are necessary ingredients to reintroduce the low-frequency concepts of capacitance per unit length of transmission line, or characteristic capacitance, and the inductance per unit length, or characteristic inductance.

In the following we concentrate on the circuit representation of coplanar transmission lines and take the existence of circuit representations for the objects that are smaller than the wavelength, for the reasons cited above, for granted.

## 2.1. Plane Wave Propagation in Axially Symmetric Media

We consider a setup with arbitrarily shaped conductors surrounded by a uniform linear medium with scalar permittivity  $\epsilon$  and scalar permeability  $\mu$ . The only requirement for the setup is to be symmetric with respect to translations in one direction. We arrange our cartesian coordinates such that the  $z$ -axis is the direction of axial-symmetry, c.f. figure 2.1. We express the Maxwell equations in SI units in terms of the fundamental electric and magnetic fields,  $\vec{\mathcal{E}}$  and  $\vec{\mathcal{B}}$ , and their macroscopic or coarse grained versions electric displacement and magnetic intensity,  $\vec{\mathcal{D}} = \epsilon\vec{\mathcal{E}}$  and  $\vec{\mathcal{H}} = (1/\mu)\vec{\mathcal{B}}$ , which include the effects of electric and magnetic polarization in various, linear media,

$$\nabla \times \vec{\mathcal{H}} = \vec{\mathcal{J}} + \epsilon \frac{\partial \vec{\mathcal{E}}}{\partial t} \qquad \nabla \times \vec{\mathcal{E}} = -\mu \frac{\partial \vec{\mathcal{H}}}{\partial t} \quad (2.1a)$$

$$\nabla \cdot \vec{\mathcal{B}} = 0 \qquad \nabla \cdot \vec{\mathcal{D}} = \mathcal{Q}. \quad (2.1b)$$

We are not interested in a general solution to the set of Maxwell equations for the given situation but rather concentrate on plane wave steady state solutions oscillating with frequency  $\omega$  and traveling in  $z$ -direction with wavevector  $\beta$ ;  $\vec{\mathcal{E}}(x, y, z) = \vec{E}(x, y)e^{i(\omega t - \beta z)}$ ,  $\vec{\mathcal{H}}(x, y, z) = \vec{H}(x, y)e^{i(\omega t - \beta z)}$ ,  $\vec{\mathcal{J}}(x, y, z) = \vec{j}(x, y)e^{i(\omega t - \beta z)}$  and  $\mathcal{Q}(x, y, z) = \rho(x, y)e^{i(\omega t - \beta z)}$ . With this ansatz and the assumption of spatially independent  $\epsilon$  and  $\mu$  the Maxwell equations are already considerably simplified,

$$\begin{pmatrix} \partial_y H_z + i\beta H_y \\ -i\beta H_x - \partial_x H_z \\ \partial_x H_y - \partial_y H_x \end{pmatrix} = \begin{pmatrix} j_x + i\omega\epsilon E_x \\ j_y + i\omega\epsilon E_y \\ j_z + i\omega\epsilon E_z \end{pmatrix} \quad \begin{pmatrix} \partial_y E_z + i\beta E_y \\ -i\beta E_x - \partial_x E_z \\ \partial_x E_y - \partial_y E_x \end{pmatrix} = -i\omega\mu \begin{pmatrix} H_x \\ H_y \\ H_z \end{pmatrix} \quad (2.2a)$$

$$\partial_x H_x + \partial_y H_y - i\beta H_z = 0 \qquad \partial_x E_x + \partial_y E_y - i\beta E_z = \frac{\rho}{\epsilon}. \quad (2.2b)$$

Keep in mind that these are not fully valid across dielectric-metal boundaries. For the derivation of the boundary conditions we have to fall back on equations (2.1a).

## 2.2. TEM Wave Propagation

As it turns out not all components of the electromagnetic field are needed to construct solutions to equations (2.2a) and (2.2b). We first consider vanishing axial components of the electromagnetic fields  $E_z = B_z = 0$ . In this case  $E$  and  $H$  are transversal to the direction of propagation hence the name **Transverse ElectroMagnetic (TEM)** wave. The equations (2.2a) and (2.2b) further simplify in this particular case to,

$$\begin{pmatrix} i\beta H_y \\ -i\beta H_x \end{pmatrix} = \begin{pmatrix} j_x + i\omega\epsilon E_x \\ j_y + i\omega\epsilon E_y \end{pmatrix} \qquad \begin{pmatrix} E_y \\ E_x \end{pmatrix} = Z_0 \begin{pmatrix} -H_x \\ H_y \end{pmatrix} \quad (2.3a)$$

$$\partial_x H_y - \partial_y H_x = j_z \qquad \partial_x E_y - \partial_y E_x = 0 \quad (2.3b)$$

$$\partial_x H_x + \partial_y H_y = 0 \qquad \partial_x E_x + \partial_y E_y = \frac{\rho}{\epsilon}. \quad (2.3c)$$

Evaluated outside the conductor regions,  $\vec{j} = 0$ , equations (2.3a) tell us that  $\vec{E}$  and  $\vec{H}$  are always perpendicular to each other in the dielectric and determine the wave impedance, which is the ratio of the magnitudes of electric field and magnetic intensity  $|E|/|H| = \sqrt{\mu/\epsilon} =: Z_0$ . Equations (2.3a) further establish the dispersion relation  $\beta = \omega\sqrt{\epsilon\mu} = k_0$  which is the same for a plane wave traveling in a isotropic and uniform medium with scalar permittivity  $\epsilon$  and permeability  $\mu$  without any incorporated conductors. For finite conductivity  $\sigma$  ( $\vec{j} = \sigma\vec{E}$ ) we have a different dispersion relation in the conductor. The electromagnetic field has to be phase matched for all times at the dielectric-conductor boundary to fulfill the boundary conditions. This is not compatible with the two different dispersion relations and consequently no TEM mode exists. Below we will find a TEM mode with the assumption of perfect conductors  $\sigma \rightarrow \infty$  and in the case of planar transmission lines (c.f. section 2.4), where we encounter a boundary between air and dielectric, we will resort to a low frequency approximation.

Every closed line integral, in the  $x$ - $y$ -plane, of the electric field vanishes as can be seen in equation (2.3b) for the electric field. This opens up the opportunity to derive the electric field from a two-dimensional potential  $\vec{E} = -\nabla\Phi$ . This potential function has to fulfill a Laplace equation  $\Delta\Phi = 0$  in the dielectric which can be derived from equation (2.3c). In order to solve for  $\Phi$  we additionally need boundary conditions.

For finite conductivity  $\sigma$ , oscillating electromagnetic fields can only penetrate the conductor up to a skin depth of  $\delta_S = \sqrt{2/(\omega\mu\sigma)}$ . For the superconductors used in circuit QED setups we can safely assume the conductivity to be infinite  $\sigma \rightarrow \infty$  and all electromagnetic fields are expelled from the interior of the (super-)conductor due to shielding from induced surface currents  $\vec{j}_S = \vec{n} \times \vec{H}$  and surface charges  $\rho_S = \epsilon\vec{n} \cdot \vec{E}$ , where  $\vec{n}$  is a unit vector perpendicular to the boundary between conductor and dielectric. Therefore the potential  $\Phi$  is constant throughout the conductor. The two homogeneous Maxwell equations tell us that there is no tangential electrical field at the dielectric-conductor boundary  $\vec{n} \times \vec{E} = 0$  and that the component of the magnetic density normal to the dielectric-conductor boundary vanishes  $\vec{n} \cdot \vec{H} = 0$ . The vanishing of the tangential component of the electric field is fulfilled because of the constant potential  $\Phi$  throughout the conductor and also the boundary condition for the normal magnetic density is fulfilled by virtue of the fact that  $\vec{E}$  and  $\vec{H}$  are always perpendicular to each other.

To find the TEM mode for a given setup with dielectric and conductors the solution process is to assign to every conductor a fixed potential and solve the Laplace equations with this fixed boundary condition. With the potential we can derive the electric field  $\vec{E} = -\nabla\Phi$  and immediately infer the magnetic density with equations (2.3a). With this we can already tell that there will be no TEM mode in a waveguide with only one conductor, since there only exist constant solutions for the Laplace equations if the potential  $\phi$  has to be equal to the same constant  $V_0$  on the whole boundary and therefore the electric field would vanish. We need to have at least two different conductors to get a TEM mode. Further on we will restrict our considerations to waveguides with only two conductors, which are also called transmission lines, like the one depicted in figure (2.1). From the uniqueness of the solution of the Laplace equation for fixed boundary conditions we can further deduce that there will be only one TEM mode for a given two conductor setup.



### 2.2.1. Lumped Element Representation

The ultimate goal of this chapter is to replace the description of microwave circuits in terms of Maxwell equations with the simplified, and most importantly modular, theory of electrical circuits with capacitors and inductors and the associated Kirchhoff rules. To this end we have to decide whether a description of the given setup in terms of a electrical circuit actually exists and if so what the layout of the electrical circuit would be. This decomposition of the given setup into a network of two terminal devices will include capacitors and inductors and later on also Josephson junctions. Capacitors and inductors are fully described with one parameter, the capacitance  $C$  and the inductance  $L$  respectively. The parameters  $C$  and  $L$  constitute a relationship between the current  $I$  that is flowing through the device and voltage drop  $V$  at the two terminals and encode the microscopic details of the electromagnetic field description,

$$I = C \frac{dV}{dt} \qquad V = L \frac{dI}{dt}. \qquad (2.4)$$

The concept of capacitance  $C$  and inductance  $L$  is therefore tightly bound to the concept of electrical voltage. The difference in Voltage  $V_{a,b}$  between two points  $a$  and  $b$  is defined as the line integral of the electric field along an arbitrary path connecting the two points  $V_{a,b} = \int_a^b \vec{E} \cdot d\vec{l}$ . The definition for the voltage difference between two points has to be independent of the chosen path for the integral of the electric field. This only holds for electrical fields with vanishing curl. The electrical field for our TEM mode does not have vanishing curl, however the axial component of its curl vanishes. Consequently all path integrals of the electrical field are independent of the specific path as long as the line defined by start and end points is parallel to the axial direction. Therefore it does make sense to introduce the concept of voltage for the TEM mode in the axial direction of the transmission line. We define capacitances  $c$  and inductances  $l$  per unit length for infinitesimal small slices of the transmission line. The determination of  $l$  and  $c$  for the given TEM mode can be accomplished with the following two alternative definitions of capacitances and inductances,

$$C = \frac{Q}{V} \qquad L = \frac{\Psi}{I}, \qquad (2.5)$$

where we substitute the total induced charge  $Q$  with the charge per unit length of transmission line  $q$  and the total generated flux or equivalently flux linkage  $\Psi$  with the flux linkage per unit length  $\psi$  to get the characteristic capacitance  $c$  and inductance  $l$ . The total charge per unit length on one conductor can be determined with the help of the second equation (2.3c) and a two-dimensional Gauss integral,

$$\int_S \partial_x E_x + \partial_y E_y dx dy = \int_{\delta S} \hat{n} \cdot \vec{E} dl = \int_S \frac{\rho}{\epsilon} dx dy = \frac{q}{\epsilon}, \qquad (2.6)$$

where  $S$  is a surface in the  $x$ - $y$ -plane with the boundary  $\delta S$  encircling one conductor while not touching the other and  $\hat{n}$  the unit vector pointed outward of  $S$ . The charge on the other conductor is  $-q$  as can be seen from the integration of the inverse of surface  $S$  which ends up in the same line integral along  $\delta S$  only now with  $\hat{n}$  in the opposite direction. All in

all this provides us with the definition for  $c$  computable with the help of the field theory solution,

$$c = \frac{q}{V} = \frac{\epsilon \int \hat{n} \cdot \vec{E} dl}{\int_{c_1}^{c_2} \vec{E} \cdot d\vec{l}}, \quad (2.7)$$

with  $c_1$  and  $c_2$  arbitrary points, which are in the same  $x$ - $y$ -plane, on conductor 1 and conductor 2 respectively.

For the characteristic inductance we follow a similar procedure. The total current flowing on one conductor may be found by integrating the first equation (2.3b),

$$I = \int_S j_z dx dy = \int_S \partial_x H_y - \partial_y H_x dx dy = \int_{\delta S} \vec{H} \cdot d\vec{l} = \frac{1}{Z_0} \int_{\delta S} \hat{n} \cdot \vec{E} dl = \frac{q}{\epsilon Z_0}, \quad (2.8)$$

and again the current flowing on the other conductor is  $-I$ . The flux linkage is the total flux generated by the current  $I$ . The magnetic flux lines resemble concentric deformed circles around both conductors. If we integrate the total flux in between the conductors we integrate the total magnetic flux. If we choose our path  $\Gamma$  of integration between both conductors along a line of electric force than we immediately know that the magnetic field is always perpendicular to the path of integration by virtue of equation (2.3a). Therefore the flux per unit length of transmission line is,

$$\psi = \mu \int_{\Gamma} \hat{n} \cdot \vec{H} dl = \mu \int_{\Gamma} |\vec{H}| dl = \frac{\mu}{Z_0} \int_{\Gamma} \vec{E} \cdot d\vec{l} = \frac{\mu}{Z_0} V, \quad (2.9)$$

and consequently the inductance per unit length of transmission line is  $l = (\mu V)/(Z_0 I)$ . With these two equations we can establish a connection between the electromagnetic field description and the description in terms of circuit theory for a TEM mode,

$$Z_c = \frac{V}{I} = \frac{\epsilon |\vec{E}|}{c |\vec{H}|} = \frac{\epsilon}{c} Z_0 = \sqrt{\frac{l}{c}} \quad v = \sqrt{\frac{1}{\mu\epsilon}} = \sqrt{\frac{1}{lc}}. \quad (2.10)$$

The quotient between the voltage and current, the characteristic impedance, is the wave impedance multiplied by  $\epsilon/c$  and the phase velocity of the current-voltage wave on the transmission line coincides with the phase velocity of a plane wave in the dielectric.

With the help of the above derived characteristic capacitance  $c$  and inductance  $l$  for TEM wave propagation on a transmission line we can now devise a one-dimensional electrical circuit model that supports wave propagation with the above derived velocity  $v = 1/\sqrt{lc} = 1/\sqrt{\epsilon\mu}$  and characteristic impedance  $Z_c = V/I = \sqrt{l/c}$ . The electrical circuit consists of inductors connected in series and each node in between the inductors connected in parallel with a capacitor to a second conductor (c.f. figure 2.2). We can now derive the wave equation with the help of Kirchhoff rules and the relationships for the voltage drop and current flowing through the inductors and capacitors (c.f. equation 2.4). The current flowing on any arbitrary node at  $z$  must vanish,

$$-\mathcal{J} - c dz \partial_t \mathcal{V} + \mathcal{J} + \partial_z \mathcal{J} dz = 0 \quad \Leftrightarrow \quad \partial_z \mathcal{J} = c \partial_t \mathcal{V},$$

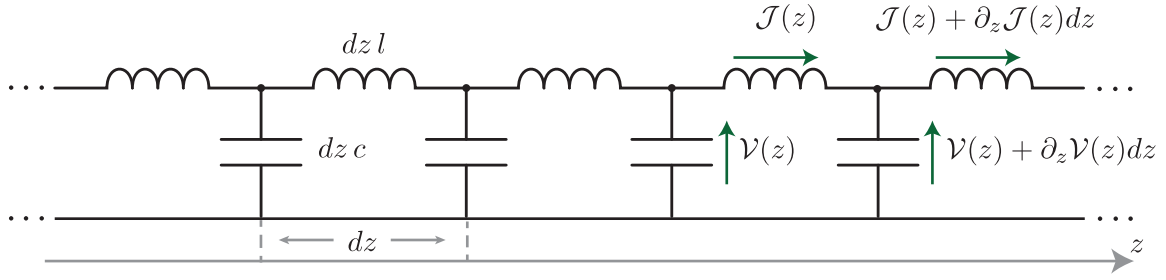


Figure 2.2.: Lumped element representation of the TEM mode of a transmission line. Each mesh represents a piece of transmission line of length  $dz$  with capacitance  $c dz$  and inductance  $l dz$ . The direction for the definition of the time dependent current  $\mathcal{J}$  and voltage  $\mathcal{V}$  is given by the green arrows.

where we keep only terms linear in the infinitesimal piece of transmission line  $dz$ . And the voltage drops around the mesh at the same node also vanish,

$$-\mathcal{V} - l dz \partial_t \mathcal{J} + \mathcal{V} + \partial_z \mathcal{V} = 0 \quad \Leftrightarrow \quad \partial_z \mathcal{V} = l \partial_t \mathcal{J}.$$

With these two equations we can already derive the wave equations for the voltage and current of the transmission line,

$$\partial_z^2 \mathcal{J} - lc \partial_t^2 \mathcal{J} = 0 \quad \partial_z^2 \mathcal{V} - lc \partial_t^2 \mathcal{V} = 0. \quad (2.11)$$

A general solution to this wave equation can be formulated in terms of forward-  $\vec{f}(z - t/v)$  and backward propagating pulses  $\overleftarrow{f}(z + t/v)$ ,

$$\mathcal{J} = \vec{\mathcal{J}} \vec{f}(z - \frac{t}{v}) + \overleftarrow{\mathcal{J}} \overleftarrow{f}(z + \frac{t}{v}) \quad \mathcal{V} = \vec{\mathcal{V}} \vec{f}(z - \frac{t}{v}) + \overleftarrow{\mathcal{V}} \overleftarrow{f}(z + \frac{t}{v}).$$

To fulfill the relation between current and voltage  $\partial_z \mathcal{J} = -c \partial_t \mathcal{V}$  we realize that the forward and backward amplitudes of current and voltage on the line are not independent but rather related to each other via the characteristic impedance  $\vec{V}/\vec{J} = -\overleftarrow{V}/\overleftarrow{J} = Z_c$ . The characteristic impedance is therefore not the ratio of voltage to current at every arbitrary point on the transmission line but rather the ratio between the constant forward propagating amplitudes of voltage and current or the negative ratio of the constant backward propagating amplitudes of voltage and current. This issue did not come up in our field theoretic description because we were only dealing with forward propagating harmonic waves.

### 2.3. TE/TM Wave Propagation

TE and TM wave propagation have a lot of similarities the only difference is the vanishing of the axial field component of  $\vec{E}$  for TE modes compared to the vanishing axial component of  $\vec{H}$  for TM modes. We restrict this description to the TE wave mode. For vanishing

axial electric field component  $E_z = 0$  we may again reformulate our electromagnetic field equations (2.2a) and (2.2b) with the help of the same ansatz for the electromagnetic fields, currents and charges as above for the TEM mode, to,

$$\begin{pmatrix} \partial_y H_z \\ \partial_x H_z \end{pmatrix} = \begin{pmatrix} j_x + i\frac{k_c^2}{\beta} H_y \\ -j_y + i\frac{k_c^2}{\beta} H_x \end{pmatrix} \quad \begin{pmatrix} E_y \\ E_x \end{pmatrix} = \frac{k_0}{\beta} Z_0 \begin{pmatrix} -H_x \\ H_y \end{pmatrix} \quad (2.12a)$$

$$\partial_x H_y - \partial_y H_x = j_z \quad \partial_x E_y - \partial_y E_x = -i\omega\mu H_z \quad (2.12b)$$

$$\partial_x H_x + \partial_y H_y = i\beta H_z \quad \partial_x E_x + \partial_y E_y = \frac{\rho}{\epsilon}, \quad (2.12c)$$

where  $k_c^2 = k_0^2 - \beta^2$  and  $k_0 = \omega v$  the plane wave wavevector in the dielectric. Similar to TEM wave propagation we again deduce that, in the dielectric,  $\vec{E}$  and  $\vec{H}$  are perpendicular to each other from equations (2.12a). The wave impedance however is altered  $Z_h := (k_0/\beta)Z_0$  and now depends via  $\beta$  on the specific layout of the conductors and dielectric in contrast to the TEM mode where the wave impedance is simply the wave impedance of a plane wave in a dielectric without any conductors. For TE modes the axial magnetic intensity component  $H_z$  assumes the role of a potential function for the magnetic intensity in the x-y-plane in the dielectric as can be seen in the first equation (2.12a). If we differentiate the first component of the first equation (2.12a) with respect to  $y$  and the second component with respect to  $x$  and use the first equation (2.12c) we can derive the Helmholtz eigenvalue equation for  $H_z$ ,

$$\partial_x^2 H_z + \partial_y^2 H_z + k_c^2 H_z = 0. \quad (2.13)$$

This eigenvalue problem generates eigenfunctions  $H_{z,n}$  and eigenvalues  $k_{c,n}$ ; the different TE modes of the given setup. With these we can derive the full magnetic intensity and the electric field with the help of equations (2.12a). The peculiar relation between the wave vector for the plane wave in the bare dielectric  $k_0$ , the wave vector in z-direction  $\beta$  and the eigenvalue  $k_{c,n}$ ,  $k_0^2 = \beta^2 + k_{c,n}^2$ , lends itself to the following intuitive explanation: like the two sides of a right triangle the wave vector in axial direction  $\beta$  and the eigenvalue  $k_{c,n}$  are the components in axial direction and perpendicular to it of the hypotenuse or  $k_0$ . The eigenvalue  $k_{c,n}$  therefore can be understood as the wave vector perpendicular to the axial direction. At the same time  $k_{c,n}$  defines a lower frequency limit  $\omega_{c,n} = k_{c,n}/\sqrt{\epsilon\mu}$  for wave propagation in the specific TE mode  $n$ , with axial wave vector  $\beta_n = \sqrt{k_0^2 - k_{c,n}^2} = \sqrt{\omega^2\epsilon\mu - k_{c,n}^2}$ , which can also be understood intuitively from our wave vector decomposition picture. If the total frequency dependent wave vector  $k_0$  is equal to or even smaller than  $k_c$  than the wave vector in axial direction  $\beta$  is either 0 or even imaginary indicating rapid decay in axial direction of the electromagnetic wave. Therefore wave propagation in a given TE mode  $n$  with a wavevector  $k_0$  below the given cutoff-wavevector  $k_{c,n}$  is not possible

## 2.4. Planar Transmission Lines

A planar transmission line is a quasi two-dimensional metal structure, deposited on a dielectric substrate, which supports microwaves. The main advantage is the ease of fabrication for these setups with all its manufacturing processes lend from low-frequency circuits like central processing units which are now ubiquitous in all modern devices ranging

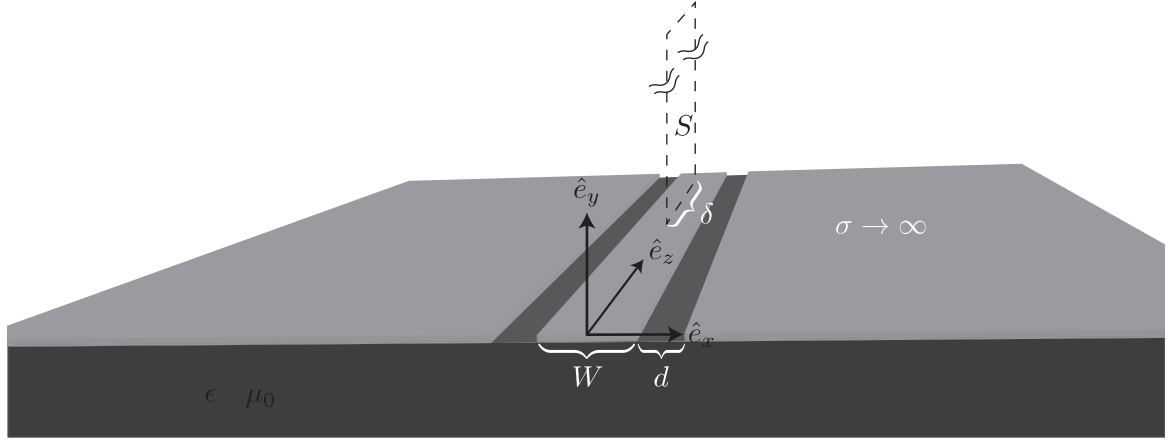


Figure 2.3.: Structure of a coplanar waveguide as an example of a planar transmission line. A metal layer is deposited on a substrate material with central conductor of width  $W$  separated from the surrounding groundplane by a gap of width  $d$

from the smartphones to super-computers. In circuit QED typically aluminium, niobium or titanium-nitride are patterned 200nm thick with optical lithography techniques on a silicon or sapphire substrate which is about  $500 \mu\text{m}$  thick. Therefore we will assume henceforth that the metal layer is infinitely thin and introduce the surface current  $\vec{J}_S = \vec{J}\delta(y)$  and the surface charge  $Q_S = Q\delta(y)$ . And we will assume the substrate dielectric to be infinitely thick, see figure (2.3). For the planar transmission lines it will be advantageous to formulate the problem in terms of the vector potential  $\vec{A}$  and the scalar potential  $\mathcal{F}$ . We may express the fields  $\vec{E}$  and  $\vec{H}$  in terms of these potential functions,

$$\vec{H} = \frac{1}{\mu} \nabla \times \vec{A} \quad \vec{E} = -(\partial_t \vec{A} + \nabla \mathcal{F}) . \quad (2.14)$$

In the Lorenz gauge  $\nabla \cdot \vec{A} + \epsilon\mu \partial_t \mathcal{F} = 0$  we can derive equations of motion for the vector potential  $\vec{A}$  and the scalar potential  $\mathcal{F}$  with the help of the Maxwell equations (2.1a) valid in the dielectric with  $\epsilon \neq \epsilon_0$  and  $\mu = \mu_0$  or in the air filled region above the planar transmission line with  $\epsilon = \epsilon_0, \mu = \mu_0$ ,

$$\Delta \vec{A} + \epsilon\mu \partial_t^2 \vec{A} = 0 \quad \Delta \mathcal{F} + \epsilon\mu \partial_t^2 \mathcal{F} = 0 . \quad (2.15)$$

A general solution can be found by taking the general solutions for the potentials in the dielectric and air individually and subsequent matching of the two solutions at the boundary between air and dielectric. We derive the boundary conditions for the electromagnetic fields with the help of the maxwell equations (2.1a),

$$\hat{e}_y \times \vec{H}|_{y \nearrow 0}^0 = \vec{J}_S \quad \hat{e}_y \times \vec{E}|_{y \nearrow 0}^0 = 0 \quad (2.16)$$

$$\hat{e}_y \cdot \vec{B}|_{y \nearrow 0}^0 = 0 \quad \hat{e}_y \cdot \vec{D}|_{y \nearrow 0}^0 = Q_S , \quad (2.17)$$

where  $(\dots)|_{y \nearrow 0}^0$  denotes the difference between the limit of the expression in brackets approaching from the air region to  $y = 0$  and the corresponding limit approaching from the

dielectric region. The tangential component of the magnetic intensity  $\vec{H}$  exhibits a jump of size  $\vec{j}_S$  upon crossing the boundary between dielectric and air throughout the metal layer and the normal component of the electric intensity exhibits a jump of size  $\rho_S$  at the same boundary layer. This means that there is a kink in the potentials  $\vec{A}$  and  $\mathcal{F}$  at the boundary and the derivatives in  $y$ -direction exhibit a jump at the dielectric-air boundary. With the help of equations (2.14) and the equation for the jump of the tangential component of  $\vec{H}$  we can immediately deduce the jump of the derivative in  $y$ -direction for the tangential components of the vector potential  $\vec{A}$

$$\partial_y A_x|_{y \searrow 0}^0 = -\mu j_{S,x} \quad \partial_y A_z|_{y \searrow 0}^0 = -\mu j_{S,z}. \quad (2.18a)$$

The universal validity of the Lorenz gauge immediately tells us the missing boundary condition for the normal component of the vector potential  $\vec{A}$ ,

$$\partial_y A_y|_{y \searrow 0}^0 = -\mu (\epsilon_0 \partial_t \mathcal{F}|_{y \searrow 0} - \epsilon \partial_t \mathcal{F}|_{y \nearrow 0}). \quad (2.18b)$$

And finally the boundary for the scalar potential  $\mathcal{F}$  may be inferred from the jump of size  $\rho_S$  of the normal component of the electric density  $\vec{D}$ ,

$$\epsilon_0 (\partial_t A_y + \partial_y \mathcal{F})|_{y \searrow 0} - \epsilon (\partial_t A_y + \partial_y \mathcal{F})|_{y \nearrow 0} = -\rho_S \quad (2.18c)$$

### 2.4.1. Low Frequency Solutions

In order to find steady state solutions oscillating with  $\omega$  propagating in axial direction with wavevector  $\beta$  for the above equations of motion for the potentials (2.14) subject to boundary conditions (2.18) we again make the ansatz  $\vec{A}(x, y, z, t) = \vec{A}(x, y, \omega) e^{i(\omega t - \beta z)}$ ,  $\mathcal{F}(x, y, z, t) = \phi(x, y, \omega) e^{i(\omega t - \beta z)}$ ,  $\vec{j}_S(x, z, t) = \vec{j}_S(x, \omega) e^{i(\omega t - \beta z)}$  and  $\rho_S(x, z, t) = \rho_S(x, \omega) e^{i(\omega t - \beta z)}$ , where we considered the possibility that the transversal wave functions depend on the frequency  $\omega$ . However we only want to take low-frequency contributions of this effect into account and expand every potential, the surface charge and surface currents in terms of frequency  $\omega$ ,

$$\vec{A} = \vec{A}^{(0)} + \omega \vec{A}^{(1)} + \omega^2 \vec{A}^{(2)} + \dots \quad \phi = \phi^{(0)} + \omega \phi^{(1)} + \omega^2 \phi^{(2)} + \dots \quad (2.19)$$

$$\vec{j}_S = \vec{j}_S^{(0)} + \omega \vec{j}_S^{(1)} + \omega^2 \vec{j}_S^{(2)} + \dots \quad \rho_S = \rho_S^{(0)} + \omega \rho_S^{(1)} + \omega^2 \rho_S^{(2)} + \dots \quad (2.20)$$

Further on we are going to restrict our calculations to lowest order in frequency  $\omega$ . Keep in mind that  $\beta$  is at least of first order in  $\omega$  similar to TEM (2.2) and TE/TM (2.3) modes in transmission lines or waveguides. With this our equations of motion for the potentials in the air and dielectric, not considering the metal layer, reduce to,

$$(\partial_x^2 + \partial_y^2) \vec{A}^{(0)} = 0 \quad (\partial_x^2 + \partial_y^2) \phi^{(0)} = 0. \quad (2.21)$$

The surface currents  $\vec{j}_S$  and surface charges  $\rho_S$ , which aren't covered in the above equations, act as sources for the potentials  $\vec{A}^{(0)}$  and  $\phi^{(0)}$ . The Lorenz gauge condition  $\partial_x A_x + \partial_y A_y - i\beta A_z + i\omega \epsilon \mu \phi = 0$  and continuity equation for electric charge  $\partial_x j_{S,x} - i\beta j_{S,z} = -i\omega \rho_S$  in zero order grant us further insight into the physics of the low frequency solution,

$$\partial_x A_x^{(0)} + \partial_y A_y^{(0)} = 0 \quad \partial_x j_{S,x}^{(0)} = 0. \quad (2.22)$$

Current can not flow across the wedges of the metal layer in  $x$ -direction. Together with the vanishing of the partial derivative with respect to  $x$  for the current component perpendicular to the direction of the transmission line we can show that the current perpendicular to the waveguide is negligible in a low frequency situation,  $j_{S,x} = 0$ . This implies the vanishing of the  $A_x^{(0)}$  component since the source for the  $A_x$  component is negligible. If the  $A_x^{(0)}$  component is zero everywhere then the zero order Lorenz condition tells us that the  $A_y^{(0)}$  component is constant in  $y$ -direction. If we are very far away from the surface of the planar transmission line the  $A_y$  component will be zero and consequently has to vanish everywhere. And finally we reduced the above vector equation for  $\vec{A}^{(0)}$  to a scalar equation for the remaining  $A_z^{(0)}$  component,

$$(\partial_x^2 + \partial_y^2) A_z^{(0)} = 0 \quad (\partial_x^2 + \partial_y^2) \phi^{(0)} = 0, \quad (2.23)$$

subject to the zero order boundary conditions  $A_z^{(0)}|_{y \searrow 0} = -\mu j_{S,z}$  and  $\epsilon_0 \partial_y \phi^{(0)}|_{y \searrow 0} - \epsilon \partial_y \phi^{(0)}|_{y \nearrow 0} = -\rho_S^{(0)}$ .

### Lumped Element Approximation

Similar to our calculations for the TEM wave propagation we are now going to derive the connection between the static capacitance  $c$  and inductance  $l$  per unit length of transmission line and the low frequency field description of the planar transmission line. We start by integrating the first order continuity equation for the charge and get,

$$\int_{-\frac{w}{2}}^{\frac{w}{2}} -i\beta j_{S,z} dx = \int_{\frac{w}{2}}^{-\frac{w}{2}} -i\omega \rho_S dx$$

$$\Leftrightarrow \beta I = \omega q \quad (2.24a)$$

which establishes the relationship between the total current  $I$  and the charge per unit length  $q$  on the central conductor. Since we assumed the central conductor to be perfectly conducting  $\sigma \rightarrow \infty$ , the tangential component of the electrical field has to vanish even in a non-static situation. For the axial component this provides us with the following equation,

$$E_z^{(1)} = -i\omega A_z^{(0)} + i\beta \phi^{(0)} = 0$$

$$\Leftrightarrow \omega A_z^{(0)} = \beta \phi^{(0)} = \beta V, \quad (2.24b)$$

where we have introduced the electrical voltage  $V$  of the central conductor with respect to the surrounding groundplane which can be defined unambiguously because of the negligible axial component of the curl of the electrical field. The electrical Voltage is constant in every slice of transmission line because of the infinite conductivity. This immediately also applies to the axial component of the the vector potential  $A_z$ . Keep in mind that the electrical voltage  $\mathcal{V}$  oscillates in axial direction proportional to  $e^{-i\beta z}$  but even though the electrical field vanishes in the conductor because the oscillating axial vector potential  $A_z$  compensates. Next we compute the characteristic inductivity of the planar transmission

line. To this end we have to integrate the entire flux generated by a piece of transmission line of length  $\delta$  and divide afterwards by  $\delta$  to get the flux linkage  $\psi$ . The surface area for the flux integral is depicted in figure 2.3,

$$\psi = \frac{1}{\delta} \int_0^{\delta} \int_0^{\infty} \vec{B} \cdot \hat{e}_x \, dydx = \frac{1}{\delta} \int_0^{\delta} \int_0^{\infty} (\nabla \times \vec{A}) \cdot \hat{e}_x \, dydx = \frac{1}{\delta} \oint_{\delta S} \vec{A} d\vec{l} = A_z. \quad (2.24c)$$

Since there is no  $A_y$  component the vertical edges of the integral around the edge of  $S$  do not contribute. The axial component of the vector potential  $A_z$  vanishes for increasing distance to the surface of the planar transmission line. Therefore we conclude that the flux linkage  $\psi$  is equal to the axial component  $A_z$  of the vector potential on the central conductor since this is the only non-vanishing part of the closed path integral of the vector potential encircling  $S$ . The characteristic capacitance and inductance of the planar transmission can be determined to,

$$c = \frac{q}{V} \qquad l = \frac{\psi}{I} = \frac{A_z}{I}. \quad (2.24d)$$

With the help of all equations (2.24) we can derive the following important relations,

$$\beta^2 = \omega^2 lc \qquad \frac{V}{I} = \sqrt{\frac{l}{c}}, \quad (2.25)$$

which show us that the propagation constant  $\beta$  and the characteristic impedance  $Z_c = V/I$  can be fully described with the knowledge of the characteristic capacitance  $c$  and inductance  $l$  which are borrowed from a description in terms of static fields.  $c$  and  $l$  are the characteristic capacitance and inductance of the planar transmission line with the central conductor at a constant  $\mathcal{V}$ , especially in axial direction constant, and with a constant current  $\mathcal{I}$  along the axial direction.



## 3. Lumped Element Circuits

### 3.1. Hamiltonians of Electrical Circuits

To reach our ultimate goal of quantization of electrical circuits we opted to first figure out the correct Hamiltonian of an electrical circuit and then quantizing the theory by promoting observables to operators with commutators derived from the Poisson brackets of their classical counterparts. The derivation of the Hamiltonian of an electrical circuit entails a slight difficulty because it is necessary to introduce a set of independent generalized coordinates. If we would introduce the current through each branch of the electrical circuit as a generalized coordinate to fully describe the state of the electrical circuit we would immediately see that not all currents flowing to a node of the electrical circuit are independent but rather are dependent because of the node-currents Kirchhoff rule. We circumvent this difficulty by introducing node fluxes.

#### 3.1.1. Energy of Capacitive and Inductive Branches

All electrical circuits considered in this work consist of networks of capacitive and inductive branches. Capacitive and inductive branches are fully described by their constitutive relations,

$$V_b = f(Q_b) \qquad I_b = g(\phi_b), \qquad (3.1)$$

respectively.  $V_b$  is the voltage difference between two sides of the branch and  $I_b$  is the current flowing through the branch. Every branch has an arbitrarily chosen direction which is necessary to unambiguously define the sign of the voltage difference and sign of the current flowing through the branch. Branch voltages and branch currents can be defined via line integrals of the electric  $\vec{E}$  and magnetic  $\vec{B}$  fields,

$$V_b = \int_{\Gamma} \vec{E} \cdot d\vec{l} \qquad I_b = \frac{1}{\mu} \oint_{\Omega} \vec{B} \cdot d\vec{l}, \qquad (3.2)$$

where the path  $\Gamma$  is chosen outside any conductor linking both ends of the branch and the path  $\Omega$  encircling the whole branch. The unambiguity and therefore validity of these definitions has already been established in the previous chapter 2. The branch charge  $Q_b$  and branch flux  $\phi_b$  can be defined to,

$$Q_b = \int_{-\infty}^t I_b(t') dt' \qquad \phi_b = \int_{-\infty}^t V_b(t') dt', \qquad (3.3)$$

under the assumption that in the infinite past all electromagnetic fields vanished. The branch flux  $\phi_b$  is a generalization of the flux linkage introduced solely for inductive branches

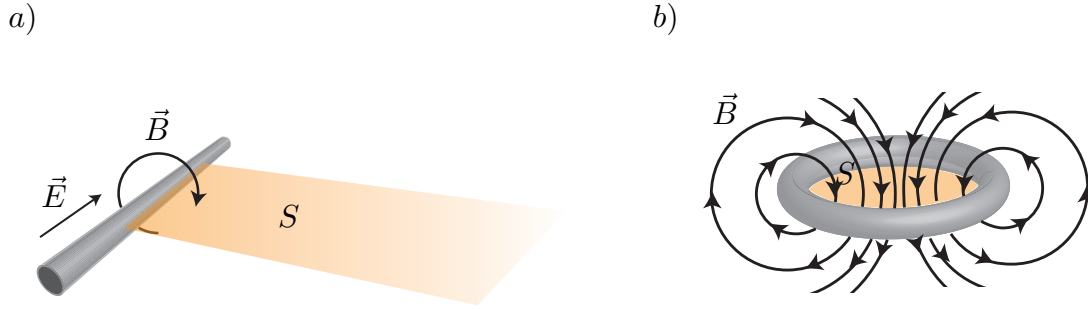


Figure 3.1.: Sketch to see the equivalence of branch flux  $\phi_b$  and flux linkage  $\psi$  for inductive elements a) A simple piece of wire can act as an inductive element due to the field generated around the wire. b) Orange shaded area for the calculation of the flux linkage of a single-turn coil

in chapter 2. In contrast to the flux linkage  $\psi$  the branch flux  $\phi_b$  can also be applied to capacitive branches since it is defined via the voltage drop along a specific branch. For inductive branches it is however the same as the flux linkage as we may convince ourselves with the following two examples. Consider a piece of wire in an electric field  $\vec{E}$  parallel to the wire (c.f. figure 3.1 a). Due to the electric field a current is flowing through the wire and due to the current there is a magnetic field with concentric magnetic field lines in planes perpendicular to the wire. If somehow the electric field would be switched off suddenly, the electrons would slow down and consequently decrease the magnetic field strength. However due to Lenz's law the diminishing magnetic field will try to accelerate the electrons, giving the electrons a kind of "electromagnetic" inertia. In this way every simple piece of wire acts as an inductor. The total generated flux of the piece of wire can be evaluated by integrating the magnetic field penetrating surface  $S$ . The static magnetic field is the result of the building up of the current in the infinite past and with the help of a Maxwell equation we get,

$$\psi = \int_S \vec{B} \cdot d\vec{s} = \int_{-\infty}^t \int_S \partial_{t'} \vec{B} \cdot d\vec{s} dt' = \int_{-\infty}^t \int_S \nabla \times \vec{E} \cdot d\vec{s} dt' = \int_{-\infty}^0 V(t') dt' = \phi_b. \quad (3.4)$$

The same holds for a inductor coil depicted in figure 3.1 b), where the plane of integration has to be changed but otherwise the whole reasoning is unchanged.

The electrical power flowing into a branch of our circuit is irrespective of the type of branch the product of the branch voltage and current  $P_b = V_b I_b = V_b \dot{Q}_b = \dot{\phi}_b I_b$ . The stored electrical energy is the time integral of the power and we get for the stored energy in terms of the branch charge and branch flux respectively,

$$h(Q_b) = \int_{-\infty}^t V_B \dot{Q}_b dt' = \int_0^{Q_b} f(Q'_b) dQ'_b \quad h(\phi_b) = \int_{-\infty}^t \dot{\phi}_b I_b dt' = \int_0^{\phi_b} g(\phi'_b) d\phi'_b, \quad (3.5)$$

where we used the constitutive relations for capacitive and inductive branches (3.1) to reformulate the time integrals. We shortly introduce now all three types of different branches used throughout this work.

**Capacitor** The capacitor appears as characteristic capacitance in the waveguiding elements of circuit QED or as lumped element version as coupling capacitance between transmission line resonators and superconducting qubits. In its lumped element version the coupling capacitance can be as simple as two metal surfaces in close proximity to each other or interdigitated metal fingers for increased capacitance (c.f. figure 3.2). Additionally every physical Josephson junction is also a capacitor (c.f. figure 3.4)

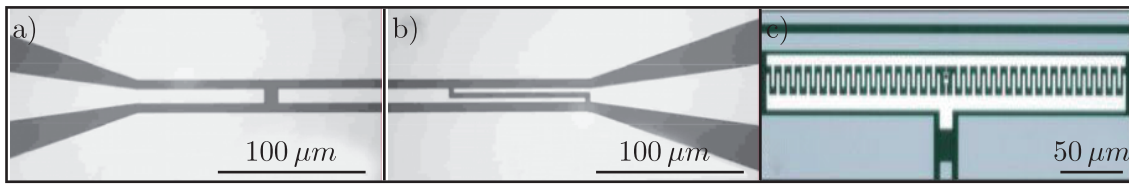


Figure 3.2.: Various versions of capacitors in circuit QED setups. a) and b) coupling capacitors with different capacitance to couple transmission line resonators. c) Interdigitated “finger” capacitor of a transmon qubit and an coupling capacitance to the transmission line. All capacitor designs by the Zürich group led by Andreas Wallraff.

**Inductor** The inductor appears like the capacitor as characteristic inductance in the transmission lines of the circuit QED setup but there is also a lumped element version of the inductor. Lumped element inductors can be realized as flattened coils in the quasi two-dimensional circuit QED setups (c.f. figure 3.3 b) or they can be large Josephson junctions or arrays of Josephson junctions operated in the linear regime (c.f. figure 3.3 a). The realization of a lumped inductor as a Josephson junction is the space-saving alternative to implement an inductor.

**Josephson Junction** The most important element of a circuit QED setup is a Josephson junction. The Josephson junction is the only non-dissipative nonlinear element in the toolbox of the circuit QED engineer. It consists of two superconducting leads in close proximity but separated by a small potential barrier. This barrier can be a piece of non-superconducting metal, a narrow constriction or point contact or as it is the case for Josephson junctions in circuit QED setups a insulating barrier. Josephson junctions in circuit QED setups are made of two aluminum leads with an insulating layer of aluminum oxide. Brian D. Josephson predicted in 1962 that current can flow across a Josephson junction as a consequence of Cooper-pair tunneling without an applied electrical field [45]. A year later Brian D. Josephson’s theory could be verified by Philip Anderson and John Rowell [2]. Every physical Josephson junction is also a capacitor, with capacitance  $C_J$ , because of the close proximity of the two superconducting metal leads. Therefore it is represented in a electrical circuit as a “pure” Josephson element with constitutive relation  $I = I_c \cos((2e/\hbar)\phi_b)$

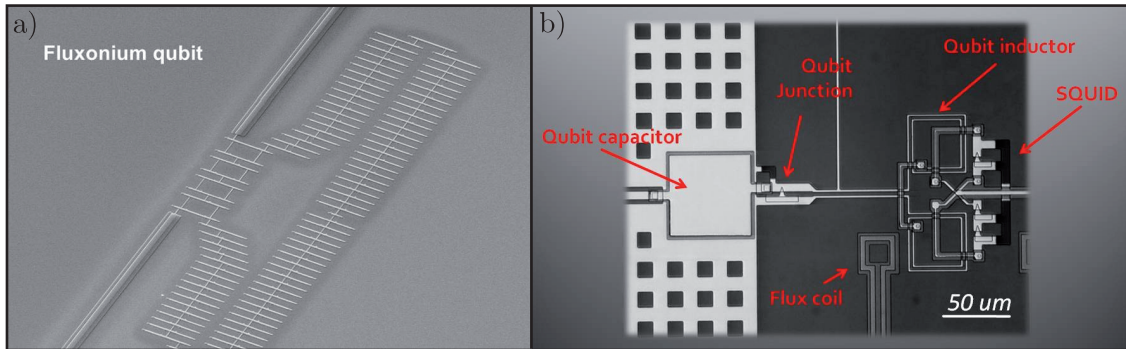


Figure 3.3.: Inductor implementations in circuit QED. a) Fluxonium qubit of the Yale group led by Michel Devoret with a large array of Josephson junctions operating as a giant inductor. b) Phase qubit of the UCSB group led by John Martinis with a lumped element inductor coil in a gradiometric design (coil has a left handed and right handed part) to reduce coupling to spurious stray fields

and a capacitor in parallel. If we neglect for a moment the nonlinearity of the purely inductive part we end up with a LC-circuit whose eigenfrequency is  $\omega_p = 1/\sqrt{C_J L_J}$ , the plasma frequency, with  $L_J = \varphi_0^2/E_J$  the Josephson inductance.  $\varphi_0 = \hbar/(2e)$  is the rescaled quantum of flux. Throughout our work we will often encounter slightly nonlinear Josephson junctions and employ the picture of the Josephson junction as a LC-circuit oscillating with the plasma frequency  $\omega_p$  and a small nonlinearity.

The critical current encodes material properties as well as the specific geometry of the junction. Because of large production variances the critical current can only be determined roughly in advance and never is the result of theoretical considerations but rather a phenomenological constant that gets adjusted to reproduce the experimental results.

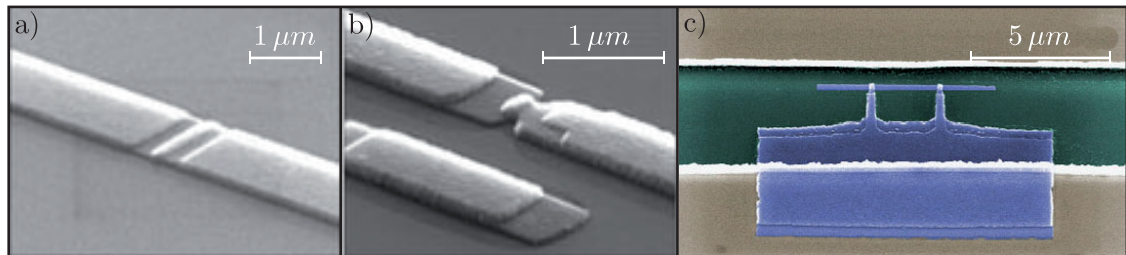


Figure 3.4.: Josephson junctions of circuit QED setups. a) and b) Josephson junctions of the ultrastrong coupling setup of the TU munich group led by Rudolf Gross. c) Charge qubit with two Josephson junctions of the first ever circuit QED experiment of the Yale group led by Robert Schoelkopf and Steven Girvin

We concisely present the type, name, constitutive relation and energy for all types of branches with the symbolic representation in a electrical circuit considered in this work in table 3.1.

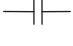


type	name	constitutive relation	energy	symbol
capacitive	capacitor	$V_b = \frac{Q_b}{C}$	$h = \frac{Q_b^2}{2C} = \frac{C}{2} \dot{\phi}_b^2$	
inductive	inductor	$I_b = \frac{\phi_b}{L}$	$h = \frac{\phi_b^2}{2L}$	
	Josephson junction	$I_b = I_0 \cos(\frac{2e}{\hbar} \phi_b)$	$h = -E_J \cos(\frac{\phi_b}{\varphi_0})$	

Table 3.1.: Table for all possible branches with type, name, constitutive relation, energy of the specific branch and the symbolic representation in a electrical circuit.  $E_J = I_c \varphi_0$  is the Josephson energy.

### 3.1.2. Spanning Tree and Node Fluxes

Now that we know the energy of the individual branches we can set up a Lagrangian for every conceivable electrical circuit. We opt to express the state of the electrical circuit in terms of the branch fluxes  $\phi_b$ . With this choice we made the energy accumulated in the capacitive branches to the equivalent of the kinetic energy of a mechanical system since they depend on the time derivative of the branch flux (c.f. table 3.1). The energy stored in the inductive branches is consequently the equivalent of the potential energy of a mechanical system. The Lagrangian of any electrical circuit is therefore the sum of all the capacitively stored energy subtracted by the sum of all inductively stored energy. If we would now attempt to get the Hamiltonian of the system by Legendre transforming the Lagrangian expressed in terms of the branch fluxes we would immediately get into trouble because not all branch fluxes are independent quantities. If we integrate the Kirchhoff rule of the vanishing of the total voltage drop in a mesh of the electrical circuit we see that the same rule holds for the branch fluxes of the mesh,

$$\int_{-\infty}^t \sum_{k \in \text{Mesh}} V_{b|k} = \sum_{k \in \text{Mesh}} \phi_{b|k} = 0. \quad (3.6)$$

Here however we have to make a small adjustment to our lumped element approximation that we established in the previous chapter. Since we are dealing with superconductors in circuit QED the conductivity is infinitely high and any induced ring current in a mesh of the electrical circuit may persist forever. By the time this ring current is induced by a time-dependent magnetic field the Kirchhoff rule of vanishing total voltage in a mesh is violated. The time integral of this violation is exactly the flux penetrating the specific mesh and we may therefore reformulate the Kirchhoff rule for the branch fluxes to be,

$$\sum_{k \in \text{Mesh}} \phi_{b|k} = \Phi \quad (3.7)$$

where  $\Phi$  is the flux threaded through the mesh. We may proceed in the same way with the second Kirchhoff rule. If we integrate the current flowing on a node for all times the result

### 3. Lumped Element Circuits

---

should be 0 since there is no excess charge on the node,

$$\int_{-\infty}^t \sum_{k \in \text{node}} I_{b|k} = \sum_{k \in \text{node}} Q_{b|k} = 0 \quad (3.8)$$

if there were excess charge accumulation on a junction in the physical circuit we could incorporate this effect into the symbolic circuit representation by adding a capacitive branch to the node.

We now change to a set of generalized coordinates that automatically fulfills the above reformulated Kirchhoff rules. First we choose one of the nodes of the electrical circuit to be our virtual ground. Its node flux will be the reference flux for all other node fluxes and therefore is not a degree of freedom of the circuit anymore. Starting from our virtual ground we choose a connected set of branches, the spanning tree  $T$ , which connects every node of the circuit with the ground node in exactly one way. The node flux of a specific node is the sum of all branch fluxes, also considering the direction of the branch, connecting the node to ground,

$$\phi_{n|j} = \sum_k S_{j,k} \phi_{b|k}, \quad (3.9)$$

where  $S_{j,k}$  is 1,  $-1$  or 0 depending on whether branch  $k$  connects node  $j$  to ground in the correct direction, in opposite direction or is not part of the path between the node and ground at all. The remaining branches are called closure branches  $C$  and always connect two nodes on the spanning tree. The mesh that is defined by the closure branch and the spanning tree connecting both nodes, which might include the ground node itself, is called irreducible loop. To be able to express the above derived Lagrangian in terms of node fluxes we also need to know how we get a specific branch flux in terms of the node fluxes. If the specific branch is part of the spanning tree, the branch flux is the difference between the node fluxes that define the branch. If the branch is a closure branch, then the branch flux is the difference of the confining node fluxes plus the flux threaded through the associated irreducible loop,

$$\phi_{b|k \in T} = \phi_{n|j} - \phi_{n|j'} \quad \phi_{b|k \in C} = \phi_{n|j} - \phi_{n|j'} + \Phi_k. \quad (3.10)$$

To further illustrate this procedure we now want to calculate a specific example. Consider the electrical circuit depicted in figure 3.5. The green branches are the arbitrarily chosen spanning tree for the likewise arbitrarily chosen ground node. A flux is threaded through the irreducible loop defined by the closure branch between node 2 and 3. Observe here that there can not be a flux threaded through the loop defined by the closure branch between node 1 and 2 since this loop is open because of the capacitor between the ground node and node 1. The flux can not be determined because of the open loop as well as no persistent current can flow. A physical Josephson junction is between the ground node and node 2 represented in the electrical circuit by a pure Josephson inductor and a capacitor in parallel. With the direction of the branches and the spanning tree chosen according to figure 3.5 this

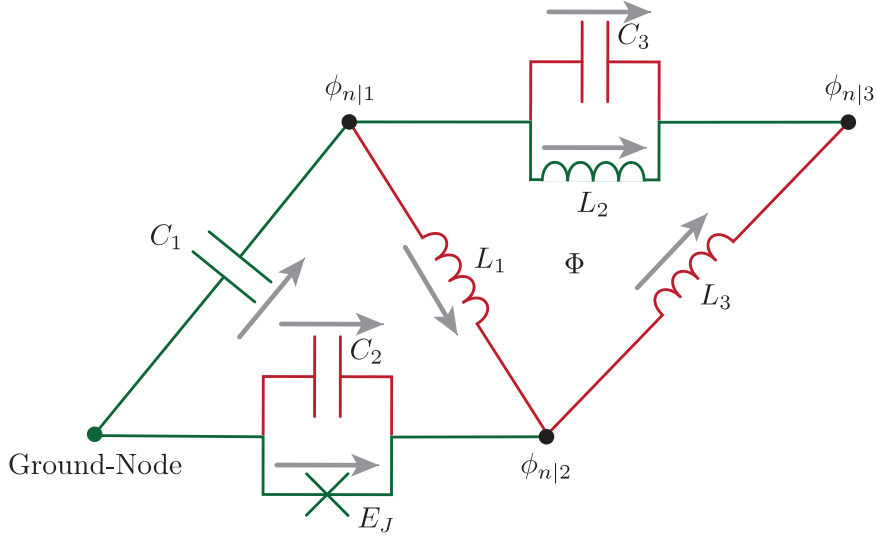


Figure 3.5.: Electrical circuit consisting of three active nodes and one ground node. The arbitrarily chosen spanning tree is marked by the green branches. Red branches are the closure branches. The irreducible loop defined by the closure branch between node 2 and node 3 is threaded by a flux  $\Phi$ . Between the ground node and node 3 is a physical Josephson junction represented in the electrical circuit by the “pure” Josephson element and a capacitor in parallel

leads us to the following Lagrangian,

$$\begin{aligned} \mathcal{L} = & \frac{C_1}{2} \dot{\phi}_{n|1}^2 + \frac{C_2}{2} \dot{\phi}_{n|2}^2 + \frac{C_3}{2} (\dot{\phi}_{n|3} - \dot{\phi}_{n|1})^2 - \\ & - \frac{(\phi_{n|2} - \phi_{n|1} + \Phi)^2}{2L_1} - \frac{(\phi_{n|3} - \phi_{n|1})^2}{2L_2} - \frac{(\phi_{n|3} - \phi_{n|2})^2}{2L_3} + E_J \cos\left(\frac{\phi_{n|2}}{\varphi_0}\right). \end{aligned} \quad (3.11)$$

With the Lagrangian we can compute the generalized momenta,

$$\frac{\partial \mathcal{L}}{\partial \dot{\phi}_{n|1}} = q_1 = C_1 \dot{\phi}_{n|1} + C_3 (\dot{\phi}_{n|1} - \dot{\phi}_{n|3}) \quad (3.12)$$

$$\frac{\partial \mathcal{L}}{\partial \dot{\phi}_{n|2}} = q_2 = C_2 \dot{\phi}_{n|2} \quad (3.13)$$

$$\frac{\partial \mathcal{L}}{\partial \dot{\phi}_{n|3}} = q_3 = C_3 (\dot{\phi}_{n|3} - \dot{\phi}_{n|1}), \quad (3.14)$$

and the Hamiltonian,

$$\mathcal{H} = \frac{(q_1 + q_3)^2}{2C_1} + \frac{q_2^2}{2C_2} + \frac{q_3^2}{2C_3} + \frac{(\phi_{n|2} - \phi_{n|1} + \Phi)^2}{2L_1} + \frac{(\phi_{n|3} - \phi_{n|1})^2}{2L_2} + \frac{(\phi_{n|3} - \phi_{n|2})^2}{2L_3} - E_J \cos\left(\frac{\phi_{n|2}}{\varphi_0}\right). \quad (3.15)$$

The first part of the Hamiltonian is the stored electrical energy expressed in node charges while the second part is the stored magnetic energy. The node charge  $q_n$  is the sum of the charges of all capacitive branches connected to the specific node.

The choice of the spanning tree and the ground node corresponds to the choice of a gauge in electromagnetic field theory.

## 3.2. Boundary Conditions

A typical circuit QED setup will consist of elements comparable to the size of the microwaves that guide waves like coplanar waveguides and coplanar waveguide resonators and elements that are much smaller than the wavelength of the commonly used microwaves like coupling capacitors, superconducting qubits and lumped element LC circuits. To accommodate our theory to this situation in circuit QED we have to introduce the description of the state of the coplanar waveguide in terms of the “node” flux field. This way we get a coherent description of lumped elements as well as elements guiding waves. And we have to derive boundary conditions for the “node” flux field that eventually will describe the scattering of waves in the coplanar waveguides at the discontinuities represented by the lumped elements of the circuit QED setup. The introduction of boundary conditions at first may seem alien to the Hamilton formalism introduced above in section 3.1 however boundary conditions will naturally emerge if we take a step back and thoroughly investigate the transition from the lumped element representation of the coplanar waveguide to the continuum limit of equations 2.11.

We start with the simplest possible discontinuity of a coplanar waveguide, the open circuited end (c.f. figure 3.6). The coplanar waveguide is subdivided in lumps of length  $\Delta$  with an in series inductance of  $\Delta l$  and a parallel capacitance to the groundplane of  $\Delta c$ . The spanning tree for the description in terms of node fluxes is chosen to take the surrounding groundplane to be the ground node. The surrounding groundplane which can be a quite large object is in the circuit representation just one node. This is because we assume the groundplane to be at the same electrical potential throughout the setup for all times. This is a prerequisite which requires in some cases careful engineering because the central line in a coplanar waveguide may cut the groundplane in two separate planes which have to be connected again by conductive air bridges to circumvent parasitic slotline modes where the two sides of the groundplane are at different electrical potential. The only branch of the spanning tree follows the central conductor with the inductances which renders the capacitive branches to be closing branches. With this choice of spanning tree



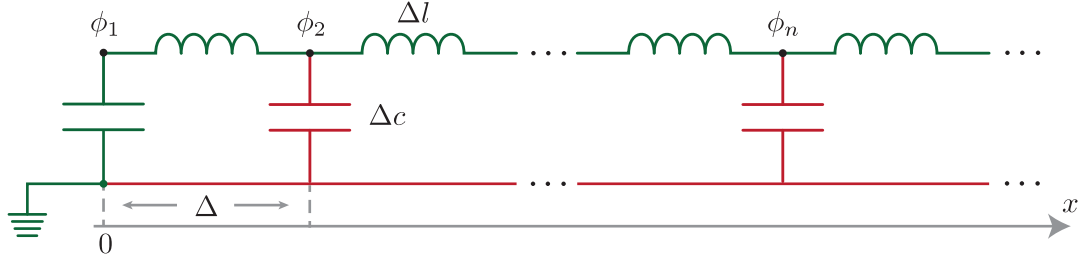


Figure 3.6.: Electrical circuit model for the open circuited coplanar waveguide. Every active node in the circuit is symbolized by a black circle. Spanning tree branches are green and closure branches red, the ground node is green. Every active node represents a piece of coplanar waveguide of length  $\Delta$  with capacitance  $\Delta c$  and inductance  $\Delta l$ . The ground node represents the entire surrounding groundplane of the coplanar waveguide resonator.

the Lagrangian expressed in terms of the node fluxes reads  $\mathcal{L} = \mathcal{L}_{\text{bulk}} + \mathcal{L}_{\text{boundary}}$  where,

$$\mathcal{L}_{\text{bulk}} = \sum_n \frac{\Delta c}{2} \dot{\phi}_n^2 - \frac{(\phi_n - \phi_{n-1})^2}{2\Delta l} \quad \mathcal{L}_{\text{boundary}} = \frac{\Delta c}{2} \dot{\phi}_1^2 - \frac{(\phi_2 - \phi_1)^2}{2\Delta l}, \quad (3.16)$$

with the subtle difference being that the first node flux only couples to one neighbor  $\phi_2$  and not to two like all other node fluxes. This affects the Lagrangian equations of motion for the node fluxes substantially,

$$\frac{d}{dt} \frac{\partial \mathcal{L}}{\partial \dot{\phi}_n} - \frac{\partial \mathcal{L}}{\partial \phi_n} = \Delta c \ddot{\phi}_n + \frac{-\phi_{n-1} + 2\phi_n - \phi_{n+1}}{2\Delta l} = 0 \quad (3.17)$$

$$\frac{d}{dt} \frac{\partial \mathcal{L}}{\partial \dot{\phi}_1} - \frac{\partial \mathcal{L}}{\partial \phi_1} = \Delta c \ddot{\phi}_1 + \frac{\phi_1 - \phi_2}{2\Delta l} = 0. \quad (3.18)$$

When we again perform the continuum limit  $\Delta \rightarrow 0$  we have to replace the node fluxes with a flux field  $\phi_n \rightarrow \phi(x)$  and the first flux node becomes the boundary value for the flux field  $\phi_1 \rightarrow \phi|_{x=0}$ . The different structure of the equations of motion for the node fluxes generates a wave equation for the flux function in the bulk,

$$\partial_t^2 \phi(x, t) - \frac{1}{lc} \partial_x^2 \phi(x, t) = 0, \quad (3.19)$$

which is enabled by the special structure of the second, inductive, term of the equation of motion for the bulk node fluxes in combination with the  $\Delta$  in the first, capacitive, term. At the boundary however the capacitive term vanishes and we get the following condition,

$$\frac{1}{l} \partial_x \phi(x)|_{x=0} = I|_{x=0} = 0, \quad (3.20)$$

which tells us the physical obvious fact that current can not flow through the open circuited end of the coplanar waveguide. In this way the correct boundary conditions emerge as the “frozen” equations of motion for node fluxes at the boundary in the continuum limit.

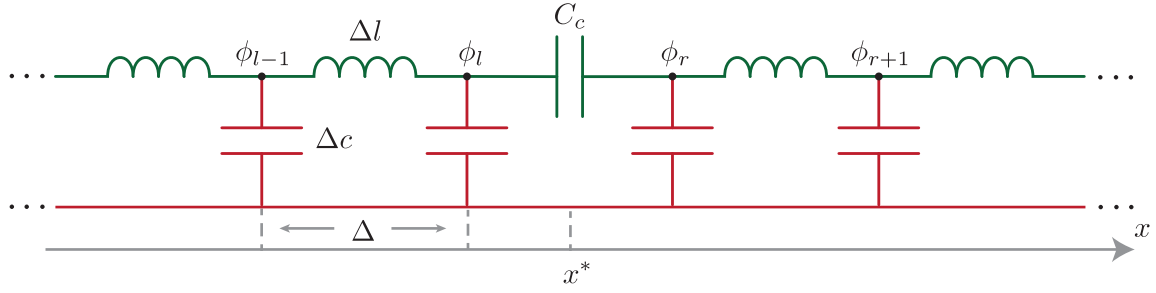


Figure 3.7.: Electrical circuit model of a coupling capacitor  $C_c$  at position  $x^*$  in a coplanar waveguide. Active nodes are black circles, spanning tree branches are green and closure branches red

Further on we use the same spanning tree as above and omit the calculation of the equations of motion in the bulk since they show no difference to the above example. We may expand on the above scheme with two additional examples which we often encountered in the course of our work. The first is the capacitive coupling  $C_c$  between two half infinite coplanar waveguides (c.f. figure 3.7) encountered in the coupling of a coplanar waveguide resonator to a half infinite coplanar waveguide to excite or detect the field in the resonator. The Lagrangian for the node fluxes directly adjacent to the coupling capacitance is,

$$\mathcal{L}_{cc} = \frac{\Delta c}{2} (\dot{\phi}_l^2 + \dot{\phi}_r^2) + \frac{C_c}{2} (\dot{\phi}_l - \dot{\phi}_r)^2 - \frac{(\phi_l - \phi_{l-1})^2}{2\Delta l} - \frac{(\phi_{r+1} - \phi_r)^2}{2\Delta l}. \quad (3.21)$$

The Euler Lagrange equations of motion are,

$$\frac{d}{dt} \frac{\partial \mathcal{L}}{\partial \dot{\phi}_l} - \frac{\partial \mathcal{L}}{\partial \phi_l} = \Delta c \ddot{\phi}_r + C_c (\ddot{\phi}_l - \ddot{\phi}_r) + \frac{\phi_l - \phi_{l-1}}{2\Delta l} = 0 \quad (3.22)$$

$$\frac{d}{dt} \frac{\partial \mathcal{L}}{\partial \dot{\phi}_r} - \frac{\partial \mathcal{L}}{\partial \phi_r} = \Delta c \ddot{\phi}_l + C_c (\ddot{\phi}_l - \ddot{\phi}_r) + \frac{\phi_r - \phi_{r+1}}{2\Delta l} = 0. \quad (3.23)$$

And after performing the continuum limit,  $\Delta \rightarrow 0$ ,  $\phi_l \rightarrow \phi|_{x \nearrow x^*}$  and  $\phi_r \rightarrow \phi|_{x \searrow x^*}$ , we get,

$$C_c (\partial_t^2 \phi|_{x \searrow x^*} - \partial_t^2 \phi|_{x \nearrow x^*}) + \frac{1}{l} \partial_x \phi|_{x \nearrow x^*} = 0 \quad (3.24)$$

$$C_c (\partial_t^2 \phi|_{x \searrow x^*} - \partial_t^2 \phi|_{x \nearrow x^*}) + \frac{1}{l} \partial_x \phi|_{x \searrow x^*} = 0. \quad (3.25)$$

The capacitor therefore may introduce a discontinuity of the flux function. Subtracting the two equations we see that the current going into the capacitor from the left has to be equal to the current leaving the capacitor to the right,

$$\frac{1}{l} \partial_x \phi|_{x \nearrow x^*} = \frac{1}{l} \partial_x \phi|_{x \searrow x^*}. \quad (3.26)$$

$C_c (\partial_t \phi|_{x \searrow x^*} - \partial_t \phi|_{x \nearrow x^*})$  is the charge on the capacitor and the boundary conditions state that the current flowing through the coupling capacitor  $C_c$  is the time derivative of this charge.

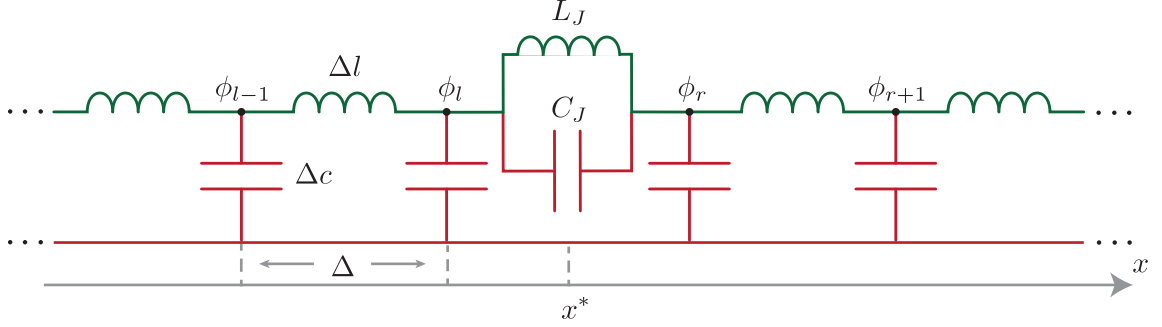


Figure 3.8.: Electrical circuit model for the linearized Josephson junction with capacitance  $C_J$  and Josephson inductance  $L_J$  at position  $x^*$  in a coplanar waveguide. Active nodes are black circles, spanning tree branches are green and closure branches red. Since the irreducible loop between the capacitor and inductor of the Josephson junction is not a physical loop in the setup but a symbolical representation of a physical Josephson junction, it can not be threaded by an external flux.

The last example involves the the interruption of the central line of the coplanar waveguide with an LC-circuit (c.f. figure 3.8). This example is of special importance to our work since it is the linearized version of a Josephson junction that interrupts the central line of the waveguide resonator. The Lagrangian for the LC circuit is,

$$\mathcal{L}_{JJ} = \frac{\Delta c}{2} (\dot{\phi}_l^2 + \dot{\phi}_r^2) + \frac{C_J}{2} (\dot{\phi}_r - \dot{\phi}_l)^2 - \frac{(\phi_l - \phi_{l-1})^2}{2\Delta l} - \frac{(\phi_{r+1} - \phi_r)^2}{2\Delta l} - \frac{(\phi_r - \phi_l)^2}{2L_J}. \quad (3.27)$$

The linear part of the Josephson junction introduces a flux drop or discontinuity in the flux function similar to the capacitor. After performing the continuum limit we end up with the following boundary conditions,

$$C_J (\partial_t^2 \phi|_{x \searrow x^*} - \partial_t^2 \phi|_{x \nearrow x^*}) + \frac{\phi|_{x \searrow x^*} - \phi|_{x \nearrow x^*}}{L_J} = \frac{1}{l} \partial_x \phi|_{x \nearrow x^*} \quad (3.28)$$

$$C_J (\partial_t^2 \phi|_{x \searrow x^*} - \partial_t^2 \phi|_{x \nearrow x^*}) + \frac{\phi|_{x \searrow x^*} - \phi|_{x \nearrow x^*}}{L_J} = \frac{1}{l} \partial_x \phi|_{x \searrow x^*}, \quad (3.29)$$

which again state that the current going into the LC-circuit coming from the left has to equal the current leaving the LC-circuit to the right  $(1/l)\partial_x \phi|_{x \searrow x^*}/(1/l)\partial_x \phi|_{x \nearrow x^*}$ . Additional to that however they tell us that the sum of the currents flowing through the capacitor  $C_J (\partial_t^2 \phi|_{x \searrow x^*} - \partial_t^2 \phi|_{x \nearrow x^*})$  and the inductor  $(\phi|_{x \searrow x^*} - \phi|_{x \nearrow x^*})/L_J$  have to be equal to the current flowing through the LC-circuit. This is the Kirchhoff rule for the embedded LC-circuit and it is a consequence of the introduction of the node fluxes that it naturally emerges as one of the “frozen” equations of motion.

### 3.3. Transfer Matrix Picture

We want to introduce a additional way of representing the flux field on the coplanar waveguide which provides computational advantages over the previous approach where the flux field is merely a real number associated to every point  $x$  of the coplanar waveguide. An eigensolution to the wave equation (c.f equation 3.19) with frequency  $\omega$  can be written in terms of forward  $\overrightarrow{\phi}$  and backward  $\overleftarrow{\phi}$  propagating plane waves,

$$\phi(x, t) = \overrightarrow{\phi}(kx - \omega t) + \overleftarrow{\phi}(kx + \omega t), \quad (3.30)$$

with

$$\overrightarrow{\phi}(kx - \omega t) = ae^{i(kx - \omega t)} \quad \overleftarrow{\phi}(kx + \omega t) = be^{-i(kx + \omega t)}. \quad (3.31)$$

The forward and backward propagating plane wave are linearly independent solutions to the wave equation and to emphasize this fact we may write them as the components of a two dimensional representation  $\vec{\phi}$  of the flux function,

$$\phi(x, t) \hat{=} \vec{\phi}(x, t) = \begin{pmatrix} \overrightarrow{\phi}(x, t) \\ \overleftarrow{\phi}(x, t) \end{pmatrix} = \begin{pmatrix} ae^{i(kx - \omega t)} \\ be^{-i(kx + \omega t)} \end{pmatrix}. \quad (3.32)$$

With this representation we are able to devise a couple of two-dimensional matrices that help us manipulate the two-dimensional flux function  $\vec{\phi}$  and will ultimately become the subject of investigation themselves in chapter 6. At first we introduce the translational matrix  $T(\delta)$  which propagates the flux function for the distance  $\delta$  in positive direction along the coplanar waveguide,

$$\vec{\phi}(x + \delta, t) = T(\delta)\vec{\phi}(x, t) \quad T(\delta) = \begin{pmatrix} e^{ik\delta} & 0 \\ 0 & e^{-ik\delta} \end{pmatrix}. \quad (3.33)$$

We may reexamine the boundary conditions for the flux function investigated in the previous section 3.2 in the framework of the two-dimensional flux function representation. We start with the open-circuited end of a coplanar waveguide. The current has to vanish at the end of the coplanar waveguide which imposes the condition  $(1/l)\partial_x\phi|_{x=0}$  on the flux function. Expressed in terms of forward and backward propagating amplitudes of the two-dimensional flux function this amounts to,

$$\overrightarrow{\phi}'(kx - \omega t)|_{x=0} - \overleftarrow{\phi}'(kx + \omega t)|_{x=0} = 0, \quad (3.34)$$

where  $\overrightarrow{\phi}'$  and  $\overleftarrow{\phi}'$  is the derivative of the forward and backward propagating amplitude with respect to the argument of the function. Notice here that we did not have to utilize the special plane wave form. A arbitrary signal propagating towards the open circuited end of the coplanar waveguide is reflected since the spatial derivative of the forward and backward propagating flux amplitudes has to be the same for all times.

The boundary condition for an open circuited end of a coplanar waveguide establishes a relationship between forward and backward propagating amplitudes of a single flux function. On the contrary the boundary condition of a coplanar waveguide interrupted by a capacitor or LC-circuit will establish relationships between the forward and backward propagating amplitudes of the flux functions directly to the right and left of the capacitor or LC-circuit. Comparable to a scattering problem we will therefore introduce a scattering matrix which will “propagate” the flux function directly left of the disruption to the immediate right of the disruption. We introduce the forward amplitudes,  $a_r$  and  $a_l$ , and backward amplitudes,  $b_r$  and  $b_l$ , directly to the right and left of the disruption,

$$\vec{\phi}|_{x \searrow x^*} = \begin{pmatrix} ae^{i(kx-\omega t)} \\ be^{-i(kx-\omega t)} \end{pmatrix} |_{x \searrow x^*} = \begin{pmatrix} a_r \\ b_r \end{pmatrix} \quad (3.35)$$

$$\vec{\phi}|_{x \nearrow x^*} = \begin{pmatrix} ae^{i(kx-\omega t)} \\ be^{-i(kx-\omega t)} \end{pmatrix} |_{x \nearrow x^*} = \begin{pmatrix} a_l \\ b_l \end{pmatrix}, \quad (3.36)$$

and reexpress the boundary conditions for the coplanar waveguide interrupted by a capacitor (c.f. equation 3.24) with them,

$$-C_c \omega^2 (a_r + b_r - a_l - b_l) + \frac{ik}{l} (a_l - b_l) = 0 \quad (3.37)$$

$$-C_c \omega^2 (a_r + b_r - a_l - b_l) + \frac{ik}{l} (a_r - b_r) = 0. \quad (3.38)$$

The boundary equations may be reformulated to,

$$\begin{pmatrix} a_r \\ b_r \end{pmatrix} = \underbrace{\begin{pmatrix} 1 + \frac{ik}{2C_c l \omega^2} & -\frac{ik}{2C_c l \omega^2} \\ \frac{ik}{2C_c l \omega^2} & 1 - \frac{ik}{2C_c l \omega^2} \end{pmatrix}}_A \begin{pmatrix} a_l \\ b_l \end{pmatrix}, \quad (3.39)$$

to get the matrix that propagates the two-dimensional flux function from the left of the capacitor to its right  $A$ . Notice here that we get the inverse of the matrix  $A$  upon inverting the sign of the wavevector  $k$  which reflects the mirror symmetry of the setup. Given the scattering matrix  $A$  of the coplanar waveguide interrupted by a capacitor we may examine the following situation: lets suppose a plane wave impinges on the capacitor from the left. The plane wave is reflected and and transmitted because of the capacitor and we want to calculate the reflection and transmission coefficients. We choose the forward and backward amplitudes according to our considerations above,  $a_l = 1$ ,  $b_l = R$ ,  $a_r = T$  and  $b_r = 0$ . And solve for the reflection and transmission coefficient  $R$  and  $T$  with the help of  $A$ ,

$$R = \frac{k}{k + i2C_c l \omega^2} \quad T = \frac{2C_c l \omega^2}{2C_c l \omega^2 - ik} \quad R + T = 1. \quad (3.40)$$

### 3. Lumped Element Circuits

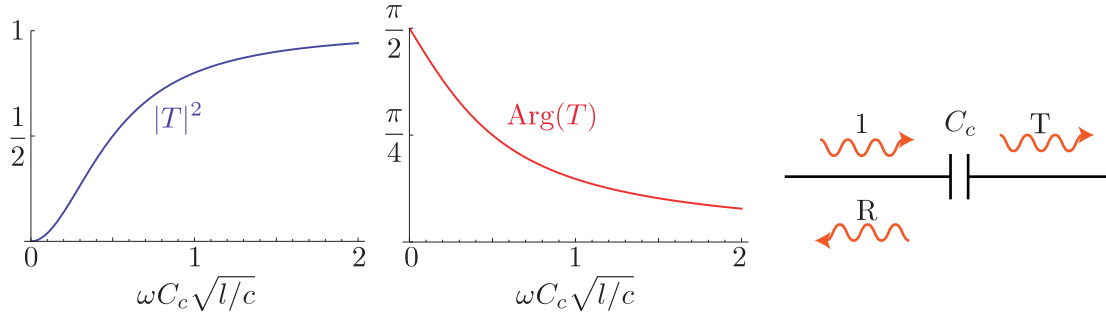


Figure 3.9.: Magnitude and phase of the transmission coefficient for plane waves on a coplanar waveguide with frequency  $\omega$  impinging on a capacitor with capacitance  $C_c$ . The circuit for coplanar waveguide in the circuit diagram depicting incoming, reflected and transmitted plane waves is abbreviated by a horizontal line.

For small frequencies  $\omega < 1/(C_c\sqrt{l/c})$  the plane waves are totally reflected at the capacitor with a  $\pi/2$  phase shift. For increasing frequencies the capacitor starts becoming transparent until it virtually disappears and lets the high frequency plane waves pass as if there was no capacitor (c.f. figure 3.9).

We proceed with the coplanar waveguide interrupted by a LC-circuit in the exact same way. The boundary conditions for the LC-circuit (c.f. equation 3.28) expressed in terms of the forward and backward amplitudes  $a_r, a_l$  and  $b_r, b_l$  are,

$$-C_J\omega^2 (a_r + b_r - a_l - b_l) + \frac{a_r + b_r - a_l - b_l}{L_J} = \frac{ik}{l} (a_l - b_l) \quad (3.41)$$

$$-C_J\omega^2 (a_r + b_r - a_l - b_l) + \frac{a_r + b_r - a_l - b_l}{L_J} = \frac{ik}{l} (a_l - b_l) . \quad (3.42)$$

And we reformulate the boundary equations again,

$$\begin{pmatrix} a_r \\ b_r \end{pmatrix} = \underbrace{\begin{pmatrix} 1 + \frac{ikL_J}{2l\left(1-\frac{\omega^2}{\omega_p^2}\right)} & -\frac{ikL_J}{2l\left(1-\frac{\omega^2}{\omega_p^2}\right)} \\ \frac{ikL_J}{2l\left(1-\frac{\omega^2}{\omega_p^2}\right)} & 1 - \frac{ikL_J}{2l\left(1-\frac{\omega^2}{\omega_p^2}\right)} \end{pmatrix}}_S \begin{pmatrix} a_l \\ b_l \end{pmatrix}, \quad (3.43)$$

to get the scattering matrix of a coplanar waveguide interrupted by a LC-circuit,  $S$ , where  $\omega_p = 1/\sqrt{L_J C_J}$  is the frequency of the LC-circuit. We consider the same situation as above of an impinging plane wave that is reflected and transmitted at the LC-circuit. Now the impinging plane wave is reflected if it is on resonance with the LC-circuit at  $\omega = \omega_p$ , with the width of the resonance  $\Delta\omega = \sqrt{(Z_J/(2Z_c))^2 + 4}$  given by the ratio of the characteristic impedances of the LC-circuit  $Z_J = \sqrt{L_J/C_J}$  and the coplanar waveguide  $\sqrt{l/c}$ . The process however can not be explained by the excitation of a harmonic oscillator which then

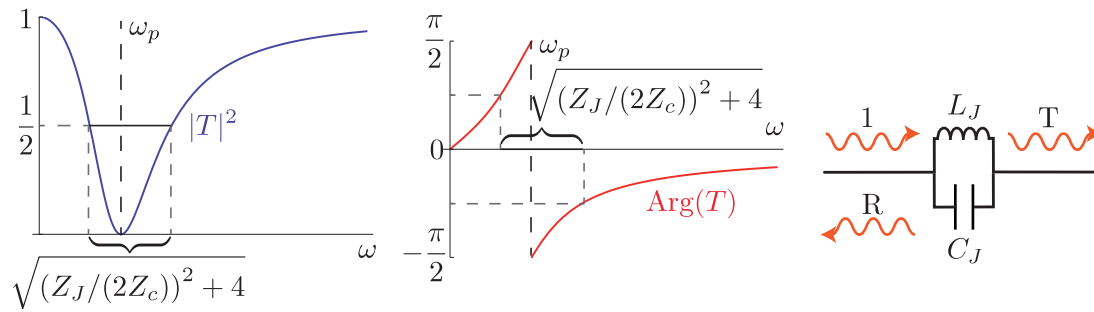


Figure 3.10.: Magnitude and phase of the transmission coefficient for plane waves on a coplanar waveguide with frequency  $\omega$  impinging on a LC-circuit with capacitance  $C_J$  and inductance  $L_J$ . The circuit for coplanar waveguide in the circuit diagram depicting incoming, reflected and transmitted plane waves is abbreviated by a horizontal line.

reemits into both directions of the coplanar waveguide as can be seen by the phase of the reflected and transmitted plane waves. Plane waves rather enter the LC-circuit and pass through the capacitor or inductor depending on the relationship between the plane wave frequency and the LC-circuit frequency. For plane wave frequencies smaller than the LC-circuit frequency  $\omega < \omega_p$  the inductor is virtually transparent and imprints its characteristic phase relations on the reflected and transmitted plane waves. For plane wave frequencies larger than the LC-circuit frequency it is the other way around: the capacitor is virtually transparent, as calculated above, and the plane waves pass through the capacitor as can be seen by the phase of the reflected and transmitted plane waves. To summarize: The resonance phenomenon observed here is the consequence of a combination of a high-pass and low-pass filter rather than the consequence of a sinusoidal excitation of a harmonic oscillator that reemits in the coplanar waveguide.





## 4. Quantization of Electrical Circuits

In the previous chapter we described the state of an arbitrary electrical circuit in terms of node fluxes with the help of a spanning tree. The introduction of node fluxes was necessary to introduce a description of the electrical circuit in terms of independent variables that already fulfill the Kirchhoff rules. With this we were able to Legendre transform and get the canonical conjugate variables of the node fluxes, the node charges, and the Hamiltonian of the electrical circuit. Up to this point however everything we did was classical physics.

The extraordinary good decoupling from external as well as internal degrees of freedom of the Cooper-pair condensate in the superconducting electronics in combination with the low operating temperatures reveals macroscopic variables like node fluxes, node charges, node voltages or branch currents to be quantum observables. Currents that are measured repeatedly prove to be random with probability distributions that are derivable from the laws of quantum mechanics. This means that for example currents can flow clockwise and anti-clockwise at the same time in a superconducting ring and show the counterintuitive correlations of entanglement in different regions of the superconducting circuit.

To get to a quantum theory of electrical circuits we proceed on the well-trodden path of canonical quantization. We promote the node fluxes and node charges to operators with the canonical commutation relations. This chapter illustrates the procedure and the consequences of the quantization of some example electrical circuits which are of importance for the discipline of superconducting circuits as well as for the work presented in the main part of the thesis.

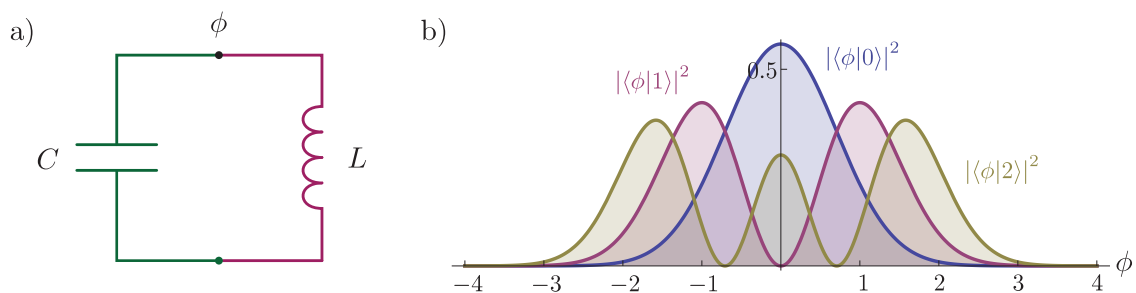


Figure 4.1.: a) Circuit representation of the LC oscillator with spanning tree. b) Probability distributions for the measurements of  $\phi$  provided the state of the LC oscillator is one of its eigenfunctions  $|n\rangle$

## 4.1. LC Oscillator

We start by quantizing the most simple and fundamental electrical circuit, the LC oscillator (c.f. figure 4.1 a). The LC oscillator consists of a capacitor and an inductor in parallel. Electrical charge can accumulate on the capacitor and generate a electrical field between the capacitor plates. A current flows through the inductor, when the capacitor discharges, and builds up a magnetic field. In this way the LC oscillator exchanges back and forth energy stored in a electric and a magnetic field. The Lagrangian of the LC oscillator is,

$$\mathcal{L} = \frac{C}{2} \dot{\phi}^2 - \frac{1}{2L} \phi^2. \quad (4.1)$$

We Legendre transform the Lagrangian to get the Hamiltonian,

$$\mathcal{H} = \frac{q^2}{2C} + \frac{\phi}{2L}, \quad (4.2)$$

with  $q = (\partial\mathcal{L})/(\partial\dot{\phi}) = C\dot{\phi}$  the canonical conjugate momentum of  $\phi$ .  $q$  is in this particular case the excess charge on one of the capacitor plates. To quantize the theory we simply promote the classical observables  $q$  and  $\phi$  to quantum observables  $q \rightarrow \hat{q}$  and  $\phi \rightarrow \hat{\phi}$  with the commutation relation  $[\hat{\phi}, \hat{q}] = i\hbar$  and get the quantum mechanical Hamilton operator,

$$\mathcal{H} \rightarrow H = \frac{\hat{q}^2}{2C} + \frac{\hat{\phi}}{2L}. \quad (4.3)$$

For linear, or nearly linear, systems it can be convenient to introduce lowering and raising operators  $a$  and  $a^\dagger$  with,

$$\hat{\phi} = \sqrt{\frac{\hbar Z_c}{2}} (a + a^\dagger) \quad \hat{q} = -i\sqrt{\frac{\hbar}{2Z_c}} (a - a^\dagger) \quad (4.4)$$

$$a = \frac{1}{\sqrt{2L\hbar\omega}} \hat{\phi} + \frac{i}{\sqrt{2C\hbar\omega}} \hat{q} \quad a^\dagger = \frac{1}{\sqrt{2L\hbar\omega}} \hat{\phi} - \frac{i}{\sqrt{2C\hbar\omega}} \hat{q}, \quad (4.5)$$

where  $Z_c = \sqrt{L/C}$  is the characteristic impedance and  $\omega = 1/\sqrt{LC}$  the resonance frequency of the LC circuit. The experimentally proven fact that superconducting circuits behave quantum mechanically has profound consequences for our expectations on the outcome of experiments. If we would measure the flux  $\phi$  in the inductor of the circuit after having extracted all energy of the system we would still measure random nonzero values for the flux variable with a gaussian probability distribution with the variance given by,

$$\sqrt{\langle 0 | (\hat{\phi} - \langle 0 | \hat{\phi} | 0 \rangle)^2 | 0 \rangle} = \sqrt{\langle 0 | \hat{\phi}^2 | 0 \rangle} = \sqrt{\frac{\hbar Z_c}{2}} =: \phi_{\text{ZPF}}. \quad (4.6)$$

For a typical LC oscillator in circuit QED setups with a characteristic impedance of 100Ω this corresponds to 0.22  $\varphi_0$ , where  $\varphi_0 = \hbar/(2e)$  is the reduced quantum of flux. The variance in the current flowing through the inductor  $I_{\text{ZPF}}$  and the variance of the voltage drop

across the capacitor  $V_{\text{ZPF}}$  of this LC circuit, with a resonance frequency of 6GHz, would be respectively,

$$I_{\text{ZPF}} = \frac{\phi_{\text{ZPF}}}{L} = \sqrt{\frac{\hbar Z_c}{2}} \frac{\omega}{Z_c} = 4.4 \text{ nA} \quad (4.7)$$

$$V_{\text{ZPF}} = \dot{\phi}_{\text{ZPF}} = \frac{i}{\hbar} [H, \phi]_{\text{ZPF}} = \frac{q_{\text{ZPF}}}{C} = \sqrt{\frac{\hbar}{2Z_c}} \omega Z_c = 0.44 \mu\text{V}, \quad (4.8)$$

where  $\hat{O}_{\text{ZPF}}$  means the zero point fluctuations  $\sqrt{\langle 0 | (\hat{O} - \langle 0 | \hat{O} | 0 \rangle)^2 | 0 \rangle}$  of the respective operator  $\hat{O}$ . If we charge the LC circuit microwave photon by microwave photon and thereby climb the equally spaced ladder of Fock states, the probability distributions for measuring specific flux values are given by the famous eigenfunctions of the linear oscillator (c.f. figure 4.1 b). This involves for example the intriguing fact that the probability for measuring zero flux vanishes for states which contain an odd number of microwave photons. It has to be emphasized here however that there are no experiments measuring directly the flux. Typical experiments with superconducting circuits involve spectroscopical measurements that are mostly sensitive to energy eigenvalues rather than specific forms of the eigenfunctions.

## 4.2. Coplanar Waveguide Resonator

Closely related to the LC oscillator is the coplanar waveguide resonator. The coplanar waveguide resonator is simply a finite piece of coplanar waveguide of length  $L$ , typically terminated at both sides with capacitive coupling to half infinite coplanar waveguides for driving and readout purposes. To simplify our description we neglect the capacitive coupling and consider a open-circuited coplanar waveguide resonator. We describe the state of the coplanar waveguide with the above introduced flux function  $\phi(x)$ . The Lagrangian of the coplanar waveguide resonator therefore reads,

$$\mathcal{L} = \int_0^L \frac{c}{2} (\partial_t \phi)^2 - \frac{1}{2l} (\partial_x \phi)^2 dx, \quad (4.9)$$

where  $l$  is the inductance and  $c$  the capacitance per unit length of coplanar waveguide. The flux function consequentially fulfills a wave equation  $\partial_t^2 \phi - v^2 \partial_x^2 \phi = 0$  with phase velocity  $v = 1/\sqrt{lc}$ . We start with an separation of variables ansatz:  $\phi(t, x) = g(t)f(x)$  and reduce the partial differential equation of motion to two ordinary equations of motion  $\ddot{g} - \omega^2 g = 0$  and  $f'' - k^2 f = 0$  with  $\omega^2$  the separation constant or rather  $\omega$  the eigenfrequency of the solution to the wave equation subject to boundary conditions.  $k = \omega/v$  is the wavevector of the solution. The fundamental solution to the ordinary differential equation for  $f$  is,

$$f(x) = ae^{ikx} + be^{-ikx}, \quad (4.10)$$

with forward  $a$  and backward  $b$  propagating amplitudes. Subject to appropriate boundary conditions we will get a set of allowed values for the wavevector  $k_n$  which in turn will provide us with discrete allowed eigenfrequencies  $\omega_n = vk_n$ . We solve for the allowed  $k_n$

with a transfer matrix technique, which will seem like taking a sledgehammer to crack a nut, however it will familiarize us with this technique that we will need below. The open circuited boundary conditions state that no current can flow at the ends of the coplanar waveguide resonator,

$$\frac{1}{l}\partial_x\phi|_{x=0} = 0 \qquad \frac{1}{l}\partial_x\phi|_{x=L} = 0, \quad (4.11)$$

which can be reformulated in terms of the forward and backward propagating amplitudes,

$$a_0 - b_0 = 0 \qquad a_L - b_L = 0, \quad (4.12)$$

where  $a_0, a_L, b_0$  and  $b_L$  are the forward and backward propagating amplitudes at the left and right end of the coplanar waveguide resonator respectively. These two equations can be considered as a system of linear equations. Unfortunately it is underdetermined since we have four variables but only two equations. The forward and backward propagating amplitudes of the right and left end of the resonator are however not independent but can be mapped on each other with the help of the already introduced translational matrix  $T(\delta)$  (c.f. equation 3.33) with  $\delta = -L$ ,

$$\begin{pmatrix} a_0 \\ b_0 \end{pmatrix} = \begin{pmatrix} e^{-ikL} & 0 \\ 0 & e^{ikL} \end{pmatrix} \begin{pmatrix} a_L \\ b_L \end{pmatrix}. \quad (4.13)$$

With this in mind we can reformulate the underdetermined set of equations into a set of equations for  $a_0$  and  $b_0$  only,

$$\begin{pmatrix} 1 & -1 \\ (1 & -1)T(-L) \end{pmatrix} \begin{pmatrix} a_0 \\ b_0 \end{pmatrix} = \begin{pmatrix} 1 & -1 \\ e^{-ikL} & -e^{ikL} \end{pmatrix} \begin{pmatrix} a_0 \\ b_0 \end{pmatrix} = \begin{pmatrix} 0 \\ 0 \end{pmatrix}. \quad (4.14)$$

We only get nontrivial solutions if the determinant of the coefficient matrix vanishes,

$$\begin{vmatrix} 1 & -1 \\ e^{-ikL} & -e^{ikL} \end{vmatrix} = -2i \sin(kL) = 0 \quad \Leftrightarrow \quad kL = n\pi. \quad (4.15)$$

We choose  $a_0$  and  $b_0$  independent of  $n$  and arbitrarily to be  $a_0 = b_0 = 1/2$  and derive the eigenfunctions  $f_n$  by propagating the solution from the left end of the coplanar waveguide resonator to position  $x$  with the help of the translational matrix  $T(\delta = x)$ ,

$$f_n(x) = \frac{1}{2} \begin{pmatrix} 1 & 1 \\ 1 & 1 \end{pmatrix} T(x)|_{k=k_n} \begin{pmatrix} 1 \\ 1 \end{pmatrix} = \cos(k_n x). \quad (4.16)$$

We can express the flux function in terms of the eigenfunctions  $f_n$  and their associated eigenfunctions  $g_n$ ,  $\phi = \sum_n g_n f_n$  which oscillate with frequencies  $\omega_n = (n\pi v)/L = n\omega_0$

that are multiples of the fundamental mode frequency  $\omega_0$ . Plugged into the Lagrangian or Hamiltonian of the coplanar waveguide resonator it decomposes into the individual eigenmodes of the system,

$$\mathcal{L} = \sum_{n=1}^{\infty} \left( \frac{Lc}{4} \dot{g}_n^2 - \frac{Lc}{4} \omega_n^2 g_n^2 \right) \quad \Leftrightarrow \quad \mathcal{H} = \sum_{n=1}^{\infty} \left( \frac{q_n^2}{Lc} + \frac{Lc}{4} \omega_n^2 g_n^2 \right), \quad (4.17)$$

with  $q_n$  the canonical conjugate momentum of the time dependent mode amplitude  $g_n$ . Notice here that  $q_n$  can not be attributed to the excess charge on a physical capacitor. Now we accomplished to decompose the coplanar waveguide resonator into an set of infinite LC oscillators with frequencies  $\omega_n = n\omega_0$  and characteristic impedances  $Z_n = (2/\pi)\sqrt{l/c}(1/n)$ , where  $\sqrt{l/c}$  is the characteristic impedance of the coplanar waveguide. Now we can proceed in an analogous manner to the previous chapter of quantizing the LC oscillator. We introduce lowering and raising operators for all eigenmodes of the coplanar waveguide resonator individually,

$$\hat{g}_n = \sqrt{\frac{\hbar Z_n}{2}} (a_n + a_n^\dagger) \quad \hat{q}_n = -i\sqrt{\frac{\hbar}{2Z_n}} (a_n - a_n^\dagger) \quad (4.18)$$

$$a_n = \sqrt{\frac{Lc\omega_n}{4\hbar}} \hat{g}_n + \frac{i}{\sqrt{Lc\hbar\omega_n}} \hat{q}_n \quad a_n^\dagger = \sqrt{\frac{Lc\omega_n}{4\hbar}} \hat{g}_n - \frac{i}{\sqrt{Lc\hbar\omega_n}} \hat{q}_n. \quad (4.19)$$

The Hamilton operator is now the sum over all Hamilton operators of the individual LC oscillators,

$$H = \sum_{n=1}^{\infty} \hbar n \omega_0 a_n^\dagger a_n. \quad (4.20)$$

Here we already rescaled the energy of the groundstate of the Hamilton operator by omitting the  $1/2$  terms in the Hamilton operators of the individual LC oscillators.

The effective capacitors and inductors of the eigenmodes of the coplanar waveguides do not have any corresponding elements in the setup, they are rather abstract objects to be chosen to reproduce the frequency and characteristic impedance of specific vibrational modes of the coplanar waveguide resonator. Therefore their quantization does not mean that the charge on a capacitor or the current through a inductor is quantized but rather the one dimensional flux field itself becomes a quantum mechanical observable,

$$\hat{\phi} = \sum_{n=1}^{\infty} \cos(n\frac{\pi}{L}x) \sqrt{\frac{\hbar Z_n}{2}} (a_n + a_n^\dagger). \quad (4.21)$$

In figure 4.2 we plot the mean value of the field  $\phi$  and its variance for various states  $|\psi\rangle$ .

### 4.3. Charge Qubit

The charge qubit is a device consisting of two superconducting islands connected by a Josephson junction (c.f. fig.:4.3 a). The two superconducting islands and the Josephson junction form a capacitor with capacitance  $C_J$ . Typically there is a gate capacitor with

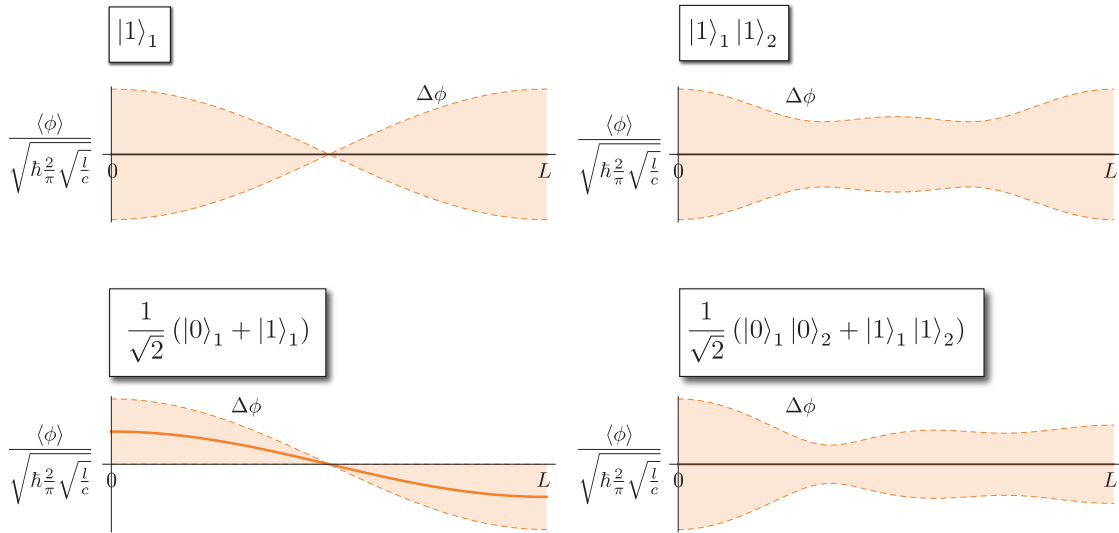


Figure 4.2.: Mean value of the field  $\bar{\phi} = \langle \psi | \hat{\phi} | \psi \rangle$  (red line) and its fluctuations  $\bar{\phi} \pm x \Delta \phi$  (orange shaded area with  $x \in [0, 1]$ ) with variance  $\Delta \phi = \langle \psi | \hat{\phi}^2 | \psi \rangle - \langle \psi | \hat{\phi} | \psi \rangle^2$  for various states  $\psi$  of the coplanar waveguide resonator. Notice that in every eigenstate of the Hamilton operator the mean value vanishes. The Bell state of the fundamental and first excited mode,  $\frac{1}{\sqrt{2}}(|0\rangle_1 |0\rangle_2 + |1\rangle_1 |1\rangle_2)$ , has vanishing mean value while the superposition of the vacuum and first fock state of the fundamental mode,  $\frac{1}{\sqrt{2}}(|0\rangle_1 + |1\rangle_1)$ , shows non-vanishing mean values of the flux field

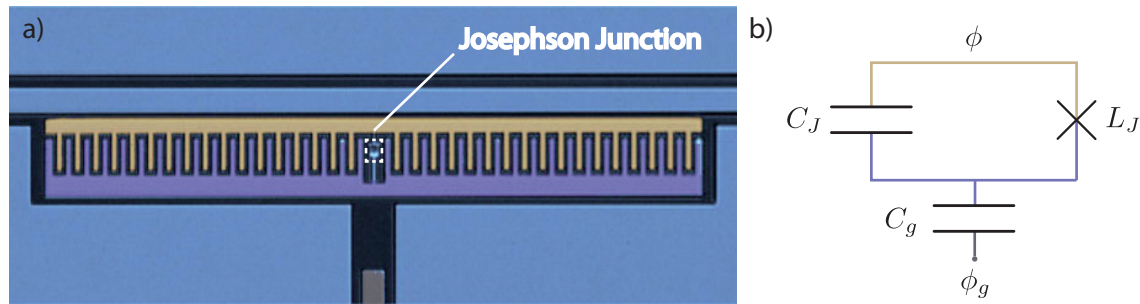


Figure 4.3.: a) Transmon type charge qubit with two superconducting islands, capacitive coupling and Josephson junction between the two islands. The qubit is controlled via a small gate voltage applied from below. b) Circuit representation of the charge qubit a). The coloring is not intended to show the spanning tree of the setup but is chosen to mirror the colored areas of the image to the right with the two superconducting islands and the gate capacitance.

capacitance  $C_g$  which is connected to a power source which can provide ac-drive signals as well as constant dc voltages to operate the charge qubit. Additionally there are trapped charges on the islands or two-level fluctuators in the oxide layer of the Josephson junction which provide uncontrolled noise acting on the charge degree of freedom of the charge qubit. We are going to combine these two effects in the flux of the node that defines the branch of the gate capacitor  $\phi_g$  (c.f. fig:4.3 b). For the purpose of our model of the charge qubit the flux  $\phi_g$  is a parameter rather than a physical observable of the system since we are not interested in the inevitable backaction of the charge qubit on its electromagnetic environment and control circuitry. The Lagrangian of the whole setup therefore reads,

$$\mathcal{L}_{cq} = \frac{C_J}{2} \dot{\phi}^2 + \frac{C_g}{2} (\dot{\phi} - \dot{\phi}_g)^2 + E_J \cos\left(\frac{\phi}{\varphi_0}\right), \quad (4.22)$$

where  $E_J = \varphi_0^2/L_J$  is the Josephson energy. We introduce the total capacitance of the island that is connected to the gate capacitor  $C = C_J + C_g$  and reformulate the Lagrangian to read,

$$\mathcal{L}_{cq} = \frac{C}{2} (\dot{\phi} + V_g)^2 + E_J \cos\left(\frac{\phi}{\varphi_0}\right), \quad (4.23)$$

where  $V_g = -(C_g/C)\dot{\phi}_g$  is the voltage drop at the gate capacitor. The choice of sign for this definition is arbitrary and given by convention. The Hamiltonian for the charge qubit is up to a irrelevant constant,

$$\mathcal{H}_{cq} = \frac{(q - q_g)^2}{2C} - E_J \cos\left(\frac{\phi}{\varphi_0}\right), \quad (4.24)$$

with  $q_g = C_g\dot{\phi}_g$  the induced charge of the gate capacitor. Now we may proceed by promoting  $q \rightarrow \hat{q}$  and  $\phi \rightarrow \hat{\phi}$  to quantum mechanical observables with the commutation relation  $[\hat{\phi}, \hat{q}] = i\hbar$ . There is however a slightly more suitable choice of observables to describe the state of the charge qubit. If we choose to describe the state of the charge qubit in terms of the number of cooper pairs that have tunneled through the Josephson junction  $\hat{n} = \hat{q}/(2e)$  and the phase-drop across the Josephson junction  $\hat{\varphi} = \hat{\phi}/\varphi_0$  rather than the flux, we get the Hamilton operator,

$$H_{cq} = 4E_C (\hat{n} - n_g)^2 - E_J \cos(\hat{\varphi}), \quad (4.25)$$

with the commutation relation  $[\hat{\varphi}, \hat{n}] = i$  and the number of induced Cooper pairs  $n_g = q_g/(2e) = (C_g\dot{\phi}_g)/(2e)$ .

**Spectrum of the charge qubit** The charge qubit is defined by two energy scales, the energy cost of transferring an electron from one of the superconducting islands to the other  $E_C = e^2/(2C_J)$  and the Josephson energy  $E_J$ . The eigenstates of the charge qubit have suppressed quantum fluctuations in their charge quadrature with respect to their fluctuations in the phase variable if the charging energy,  $E_C$ , dominates the Josephson energy and vice versa for the Josephson energy being larger than the charging energy. Let us consider at first the charge qubit where the charging energy is much larger than the Josephson energy  $E_C \gg E_J$ . In this regime the energy is given by the capacitive term in the Hamilton operator (c.f. eq: 4.25). The eigenstates of the Hamilton operator are the eigenstates of the charge operator, or equivalently, the number operator of the Cooper pairs  $|n\rangle$  with  $\hat{n}|n\rangle = n|n\rangle$ .

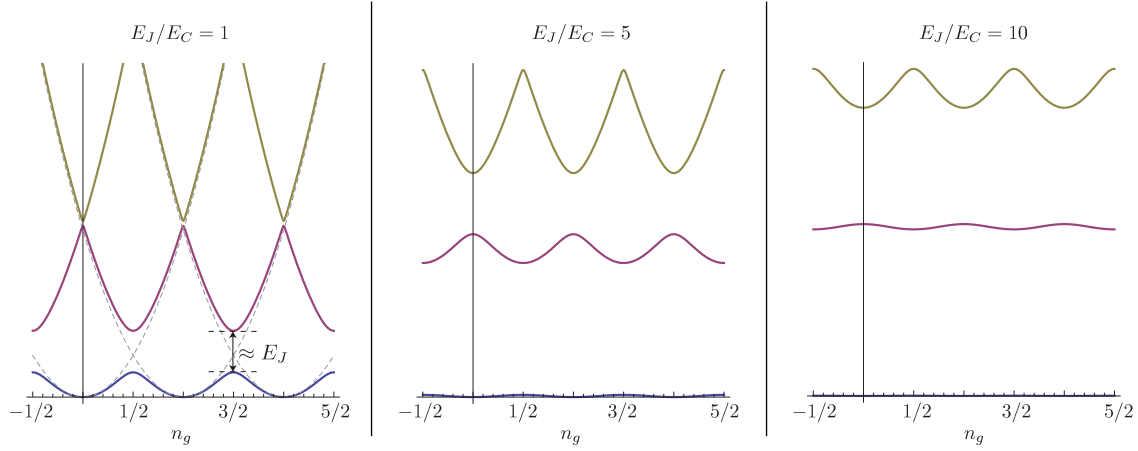


Figure 4.4.: Spectrum of the charge qubit plotted over the number of induced Cooper pairs  $n_g$  for different values of  $E_J/E_C$  ranging from the “charge” regime  $E_J/E_C = 1$  to the beginning of the “transmon”-regime  $E_J/E_C = 10$ . In the charge regime the gap between the groundstate and first excited state at the sweet spot is roughly given by the Josephson energy  $E_J$ . In the transmon regime we observe a rapid decrease of the susceptibility to noise in  $n_g$ , rendering the transmon qubit the state of the art superconducting qubit

As a function of the number of induced Cooper pairs  $n_g$  the eigenenergies are parabolas with origins at integer  $n_g$  and curvature  $4E_C$  (c.f. dashed grey graphs in fig.: 4.4). At half integer  $n_g = (n + 1)(1/2)$  eigenstates  $|n\rangle$  and  $|n + 1\rangle$  are degenerate. If we introduce the Josephson term in the Hamilton operator perturbatively the degeneracy is lifted and we get a avoided crossing every half integer  $n_g$ . For finite  $E_J/E_C$  all eigenenergies and eigenstates as a function of phase  $\varphi$  of the charge qubit can be computed exactly because there exists a mapping to the Mathieu equation and the associated Mathieu functions [47]. The eigenenergies of the charge qubit are,

$$E_n = E_C a_{2[n_g + k(n, n_g)]}(-E_J/(2E_C)) \quad (4.26)$$

with  $a_\nu(q)$  Mathieu’s characteristic value and,

$$k(n, n_g) = \sum_{l=\pm 1} [\text{int}(2n_g + l/2) \bmod 2] \cdot [\text{int}(n_g) + l(-1)^n [(n + 1)\text{div}2]] \quad (4.27)$$

a function to correctly sort band indices  $n$ . At half integer  $n_g = (n+1)(1/2)$  the eigenenergy does not change to first order upon fluctuating  $n_g$ ,  $\partial_{n_g} E_n|_{n_g=(m+1)(1/2)} = 0$  for all integer  $n$  and  $m$ . This is a very desirable feature as  $n_g$  is constantly subjected to uncontrolled noise originating from stray radiation, quasi-particle poisoning or trapped two-level fluctuators in the insulating barrier of the Josephson junction. Therefore charge qubits are operated at the avoided crossing or “sweet spot” as it is typically called. Operation at the sweet spot however requires constant feedback techniques to counteract slow thermal drift of the setup parameters. This nuisance fueled the development of a charge qubit with a



universal sweet spot, i.e. a charge qubit with eigenenergies that do not depend on  $n_g$  at all.

### 4.3.1. Transmon

The fluctuations in the induced number of Cooper pairs  $n_g$  are almost independent of the size of the superconducting islands. Therefore a good idea to decrease the influence of the fluctuations is to increase the size, or rather the mutual capacitance, of the two superconducting islands. There is however a downside to doing this: The nonlinearity of the qubit decreases at the same time, which in turn prolongs addressing the computational states of the qubit and consequentially lengthens the period in which the qubit is subject to detrimental noise. The success of the universal “sweet spot” charge qubit, or Transmon qubit, is rooted in the fact that the susceptibility to external noise in  $n_g$  decreases faster than the nonlinearity. The loss of nonlinearity can be understood as follows: If we increase the ratio of Josephson energy over charging energy the zero point flux fluctuations of the eigenstates decrease and the eigenfunctions do not probe anymore the higher order nonlinear contributions of the cosine in the Josephson term of the Hamilton operator. This already provides us with an strategy to derive a approximate Hamilton operator of the Transmon qubit from the full charge qubit Hamilton operator (eq.: 4.25). We solve the linear part of the Hamilton operator exactly and treat the nonlinear terms of the cosine in the Josephson term as a perturbation,

$$H_{cq} = 4E_C (\hat{n} - n_g)^2 - E_J \cos(\hat{\varphi}) = 4E_C (\hat{n} - n_g)^2 + \frac{1}{2}E_J \hat{\varphi}^2 - E_J \sum_{n=2}^{\infty} (-1)^n \frac{\hat{\varphi}^{2n}}{(2n)!}, \quad (4.28)$$

where we neglected the irrelevant constant part of the Cosine. We truncate the remaining nonlinear terms of the Josephson energy to the leading order quartic term,

$$H_{cq} \approx H'_{\text{Transmon}} = 4E_C (\hat{n} - n_g)^2 + \frac{1}{2}E_J \hat{\varphi}^2 - \frac{E_J}{24} \hat{\varphi}^4, \quad (4.29)$$

and we gauge transform the resulting Hamilton operator with  $U_g = e^{-in_g \hat{\varphi}}$  to get rid of the number of induced cooper pairs  $n_g$  in the capacitive term of the Hamilton operator. We introduce the generic raising and lowering operators,

$$\hat{n} = \frac{i}{2} \sqrt[4]{\frac{E_J}{2E_C}} (b - b^\dagger) \quad \hat{\varphi} = \sqrt[4]{\frac{2E_C}{E_J}} (b + b^\dagger), \quad (4.30)$$

and get the generic harmonic oscillator Hamilton operator with a quartic perturbation,

$$H'_{\text{Transmon}} = \sqrt{8E_C E_J} \left( b^\dagger b + \frac{1}{2} \right) - \frac{E_C}{12} (b + b^\dagger)^4. \quad (4.31)$$

Here we can see the aforementioned peculiar effect that the nonlinearity does not depend solely on the Josephson energy but also on the zero point fluctuations of the phase, which in turn depend on the quartic root of  $E_C/E_J$ . For the quartic leading order nonlinearity this actually means that the strength of the nonlinearity does not depend on the Josephson

energy at all. The nonlinearity of this Hamilton operator  $E_C/12$  will be very small compared to the frequency of the linear part  $\sqrt{8E_C E_J}$  and we can perform an rotating wave approximation to get rid of rotating terms in the nonlinearity,

$$H'_{\text{Transmon}} \approx H_{\text{Transmon}} = \sqrt{8E_C E_J} \left( b^\dagger b + \frac{1}{2} \right) - \frac{E_C}{2} b^\dagger b^\dagger b b. \quad (4.32)$$

Here we neglected a slight renormalization of the harmonic oscillator frequency  $\delta = -E_C/2$ . Now we can directly see the nonlinearity  $U$ , i.e. the difference in the transition energies between the groundstate and the first excited and the first excited and the second excited eigenstate of the Transmon qubit  $\Delta E_{10} - \Delta E_{21} = E_C$ . The nonlinearity in units of the frequency of the Transmon qubit  $\sqrt{8E_C E_J}$  is therefore inversely proportional to the ratio of Josephson energy to charging energy,  $U \propto 1/\sqrt{E_J E_C}$ .

Notice that the gauge transformation to get rid of  $n_g$  is only valid since we broke the discrete translational symmetry of the cosine potential already by truncation. In the Hilbert space of  $2\pi$ -periodic wave functions the translation in  $\varphi$  by  $2\pi$ ,  $U_t = e^{i2\pi\hat{n}}$  is the identity. This property is only retained after our gauge transformation for integer  $n_g$ , i.e.  $U_g$  and  $U_t$  only commute for integer  $n_g$ . Therefore we can not investigate the susceptibility of the charge qubit with respect to fluctuations in  $n_g$  with the truncated Transmon Hamilton operator  $H_{\text{Transmon}}$ . We rather have to resort to a WKB approximation for the exact eigenenergies derived from Mathieu's equation (c.f. eq.: 4.26),

$$E_n(n_g) \approx E_n(n_g = 1/4) - \frac{\epsilon_n}{2} \cos(2\pi n_g), \quad (4.33)$$

with,

$$\epsilon_n \approx (-1)^n E_C \frac{2^{4n+5}}{n!} \sqrt{\frac{2}{\pi}} \left( \frac{E_J}{2E_C} \right)^{\frac{n}{2} + \frac{3}{4}} e^{-\sqrt{8E_J/E_C}}. \quad (4.34)$$

From this we can see that the maximal possible difference in the eigenenergies of the charge qubit decrease exponentially as a function of the ratio of Josephson energy to charging energy rather than polynomially like the nonlinearity.

**Part II.**

**Many-Body Physics with Circuit  
Quantum Electrodynamics**



---

In present-day research the physics of quantum many-body systems has gained a lot of attention. Strongly interacting quantum many body systems can be found in condensed matter physics with allegedly the high temperature superconductor being one or in nuclear physics. The complexity of the microscopic models of these systems however typically prohibits direct theoretical treatment. Therefore ideal many-body Hamilton operators are investigated theoretically as minimal models for collective physical phenomena ranging from quantum phase transitions to quantum transport and nonequilibrium dynamics. Yet also technological applications are being investigated for systems with specifically designed many-body Hamilton operators. Most prominently the quantum computer would constitute, if realized once, a highly controllable interacting many-body system. Connected to quantum computing but also of fundamental interest are quantum many body phenomena like topologically protected quantum states for example in toric code models [46].

There are only few situations with analytical solutions for interacting many-body Hamilton operators. Normally one would use advanced numerical techniques to investigate theoretically the properties of the many-body Hamilton operator, but numerical methods are limited by the exponential growth of the Hilbert space of many-body systems with increasing number of particles. As an alternative approach to circumvent this dilemma, quantum simulators are now being explored intensively, thanks to the seminal comment of Richard Feynman during a keynote speech about “Simulating Physics on Computers” [27]. Quantum simulators are highly controllable quantum systems that emulate the physics of minimal model Hamilton operators that potentially reproduce quantitatively phenomena in physical systems we do not understand yet or even show phenomena hitherto not know at all. Additionally a quantum simulator should give us the opportunity to measure every observable we are interested in, that might not be accessible in the system we are simulating. Present day quantum simulators are therefore often strongly magnified versions of the respective system one is interested in, where for example lattice constants greatly exceed interatomic distances in a crystal. This can either allow to measure spatial correlations or perform manipulations for specific tasks such as quantum computing. Quantum many-body Hamilton operators can for example be simulated with cold atoms trapped by laser fields in various shapes and dimensions [10], in ion traps [29] or arrays of cavity quantum electrodynamics (QED) systems [35, 36, 34].

Almost all simulators mentioned above use massive particles to simulate massive particles. Arrays of cavity quantum electrodynamical systems pursue a different route in simulating many body physics. Photons that can hop between the cavities of the array are supposed to mimic their massive counterparts in the systems we want to simulate. Photons however rarely interact which is why they need to be coupled to nonlinear scatterers that are placed in the cavities. Because of the strong coupling between photons and nonlinear scatterers, polaritons, joint excitations of a photonic mode and an excitation of the nonlinear scatterer, emerge. The polaritons inherit the ability to move around in the array of cavities from the photonic part and an onsite nonlinearity from the nonlinear scatterers. In this context, the nonlinearity can be regarded as an interaction between polaritons in the same cavity. Polaritons however only form in the strong coupling regime, which can be reached by increasing the coupling between the nonlinear scatterer and the photonic mode of the cavity until it exceeds the decay rates of both. This condition is nowadays extremely well met in circuit QED. In circuit QED microwave photons confined by quasi

one-dimensional transmission line resonators can be coupled to Josephson junction based quantum two-level systems (qubits) [89, 9, 17]. The very small mode volume of the one-dimensional transmission line and the very large dipole moment of the Josephson qubit result in exceptionally high coupling rates [67] while the superconducting gap ensures low dissipation. In the following we show that an effective Bose-Hubbard Hamilton operator for polaritons can be engineered in an array of coplanar waveguide resonators that each couple to a transmon qubit [48].

# 5. Bose Hubbard Physics with circuit QED Arrays

## 5.1. Transmon-QED and the Bose-Hubbard Model

To generate a Bose-Hubbard model with polaritons we consider an array of capacitively coupled coplanar waveguide resonators with each resonator itself coupled to a transmon qubit (c.f. figure 5.1). In this section, we first introduce the Hamilton operator that describes this setup and then show how it can be considerably simplified and transformed into a Bose-Hubbard Hamilton operator for two polariton species.

### 5.1.1. The full Hamilton operator

The full Hamilton operator of our setup is a sum of single-site Hamilton operators,  $H_{1\text{-site},i}$ , that each describe a transmon qubit coupled to a coplanar waveguide resonator and terms that describe the capacitive coupling between neighbouring resonators,  $H_{J,i,i+1}$ ,

$$H = \sum_i (H_{1\text{-site},i} + H_{J,i,i+1}) . \quad (5.1)$$

The transmon qubit (c.f. subsection 4.3.1) regime can be accessed by shunting the Josephson junction with an additional large capacitance and thereby lowering the charging energy  $E_C = e^2/(2C_\Sigma)$ . Here,  $C_\Sigma = C_J + C_g + C_B$  is the sum of the junction's capacitance,  $C_J$ , the mutual capacitance with the coplanar waveguide resonator,  $C_g$ , and the shunting capacitance  $C_B$ . Only one of the modes of the coplanar waveguide resonator is frequency-matched to the transmon qubit and by design this mode will have an anti-node at the transmon qubit position. Therefore the Hamilton operator for one mode of the coplanar waveguide resonator coupled to a transmon qubit reads,

$$H_{1\text{-site}} = 4E_C (\hat{n} - n_g^{dc} - n_g^{ac})^2 - E_J \cos(\hat{\varphi}) + \omega_r'' a^\dagger a . \quad (5.2)$$

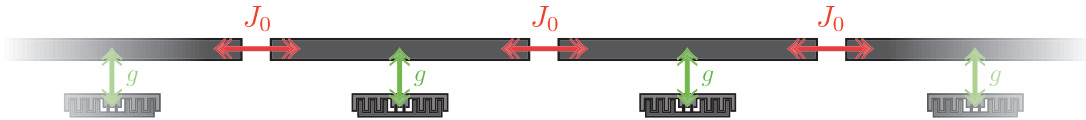


Figure 5.1.: Sketch of the proposed system to simulate Bose-Hubbard physics. Coplanar waveguide resonators are coupled capacitively in a chain and each resonator is coupled to a transmon qubit that gives rise to an on-site interaction for the polaritons. For definitions of  $J_0$  and  $g$ , see equations 5.8 and 5.5.

Here,  $\omega_r''$  is the resonance frequency of the isolated resonator and we have omitted the site-index  $i$  for readability. The transmon qubit is placed in the antinode of the coplanar waveguide resonator's field mode. This gives rise to an additional ac component,

$$n_g^{ac} = \frac{C_g}{(2e)} V_{\text{rms}}^{(0)} (a + a^\dagger), \quad \text{where} \quad V_{\text{rms}}^{(0)} = \sqrt{\omega_r''/C_r}, \quad (5.3)$$

is the root mean square voltage of the vacuum field mode,  $a$  the annihilation operator of photons in the resonator and  $C_r$  the full capacitance of the coplanar waveguide resonator with respect to the groundplane. The offset charge  $n_g^{ac}$  thus induces a coupling between the transmon qubit and photons in the resonator. For circuit QED setups one normally uses  $\lambda$ -resonators with the antinode located at the middle of the resonator.

The energy of the coupling capacitor between neighbouring coplanar waveguide resonators, e.g. sites  $i$  and  $i + 1$ , can be expressed in terms of the difference in the electrostatic potentials across the capacitor,

$$H_{J,i,i+1} = \frac{C_c (\hat{V}_i - \hat{V}_{i+1})^2}{2} = \frac{C_c \omega_r''}{C_r} \frac{1}{2} (a_i^\dagger + a_i - a_{i+1}^\dagger - a_{i+1})^2.$$

Here,  $C_c$  is the capacitance of the capacitor that connects the two resonators. We assume the electrostatic potential in resonator  $i$  to have antinodes at the ends of the resonator and write it in terms of the creation and annihilation operators,  $a_i^\dagger$  and  $a_i$ . We now turn to simplify the Hamilton operator 5.1 by a sequence of approximations.

### 5.1.2. Approximations to single-site terms

We first simplify the single-site terms,  $H_{1\text{-site}}$ , as in equation 5.2. For large  $E_J/E_C$  and low energies, the phase difference between the two islands remains small and we can expand the cosine in 5.2 around  $\varphi = 0$  up to quartic order,

$$H_{1\text{-site}}^{(1)} = 4E_C (\hat{n} - n_g^{dc} - n_g^{ac})^2 - E_J + \frac{E_J}{2} \hat{\varphi}^2 - \frac{E_J}{24} \hat{\varphi}^4 + \omega_r'' a^\dagger a. \quad (5.4)$$

Higher order terms can be neglected, c.f. [48]. In terms of bosonic creation and annihilation operators for the transmon qubit excitations,

$$\hat{n} = \frac{i}{2} \left( \frac{E_J}{2E_C} \right)^{\frac{1}{4}} (b - b^\dagger) \quad \hat{\varphi} = \left( \frac{2E_C}{E_J} \right)^{\frac{1}{4}} (b + b^\dagger)$$

the Hamilton operator 5.4 reads,

$$H_{1\text{-site}}^{(1)} = H_{\text{transmon}} + H_{\text{lin}} + H_{\text{coupling}} + H_{\text{res}}, \quad (5.5)$$

where,

$$H_{\text{transmon}} = \omega_q b^\dagger b - \frac{E_C}{12} (b + b^\dagger)^4$$

$$H_{\text{lin}} = -i4E_C n_g^{dc} \left( \frac{E_J}{2E_C} \right)^{\frac{1}{4}} (b - b^\dagger) + 2 \frac{C_g}{C_\Sigma} e V_{\text{rms}}^{(0)} n_g^{dc} (a + a^\dagger)$$

$$H_{\text{coupling}} = ig(b - b^\dagger)(a + a^\dagger)$$

$$H_{\text{res}} = \omega_r' a^\dagger a.$$



with,

$$\begin{aligned}\omega_q &= \sqrt{8E_C E_J} \\ \omega'_r &= \omega''_r \left( 1 + \frac{C_g^2}{C_\Sigma C_r} \right) \\ g &= \frac{C_g}{C_\Sigma} eV_{rms}^{(0)} \left( \frac{E_J}{2E_C} \right)^{\frac{1}{4}}.\end{aligned}$$

The terms linear in the creation and annihilation operators can be eliminated by performing the unitary transformation

$$\begin{aligned}U &= U_1 \otimes U_2 \\ U_1 &= \exp(ra - ra^\dagger) \\ U_2 &= \exp(i(sb^\dagger + sb)).\end{aligned}$$

that displaces the creation and annihilation operators by the constants  $r$  and  $s$  respectively

$$a \rightarrow U_1 a U_1^\dagger = a + r \qquad b \rightarrow U_2 b U_2^\dagger = b - is.$$

$r$  and  $s$  can now be chosen such that all terms linear in  $a$  and  $b$  cancel in the transformed Hamilton operator. Finally the interaction between the transmon qubit and the field mode of the coplanar waveguide resonator is reduced to an exchange interaction in a rotating wave approximation. To justify this rotating wave approximation we have to ensure that the interaction strength between the transmon qubit and the coplanar waveguide resonator is smaller than the sum of the frequencies of the two,

$$\frac{g}{\omega'_r + \omega_q} \ll 1. \quad (5.6)$$

Parameters extracted from [28] are  $\omega'_r = 43.6\text{GHz}$ ,  $E_C = 0.4\text{GHz}$  and a maximal value for  $E_J/E_C$  of 150. We choose  $C_g eV_{rms}^{(0)}/(C_\Sigma \omega_r) = 0.1$  which is in agreement with the theoretical upper bound in [48] and find  $\frac{g}{\omega'_r + \omega_q} \approx 0.1$ . The single-site Hamilton operator can thus be approximated by,

$$H_{1\text{-site}}^{(2)} = \sqrt{8E_C E_J} b^\dagger b - \frac{E_C}{12} (b + b^\dagger)^4 + g (a^\dagger b + ab^\dagger) + \omega'_r a^\dagger a. \quad (5.7)$$

### 5.1.3. Approximations to couplings between resonators

We now turn to simplify the couplings between neighbouring resonators,  $H_{J,i,i+1}$ . We assume that  $C_c \ll C_r$  which implies that  $C_c \omega''_r / (2C_r)$  is small compared to the isolated cavity frequency  $\omega''_r$ ,  $C_c / (2C_r) \ll 1$  and apply a rotating wave approximation to neglect those terms in the intercavity interaction that don't conserve the total photon number and therefore brake the  $U(1)$  symmetry,

$$H_{J,i,i+1}^{(1)} = J_0 (a_i^\dagger a_i + a_{i+1} a_{i+1}^\dagger) - J_0 (a_i^\dagger a_{i+1} + a_i a_{i+1}^\dagger), \quad (5.8)$$

where  $J_0 = (C_c/C_r)\omega'_r$ . The first term on the right hand side of 5.8 can be absorbed into the single-site Hamilton operators by introducing a shifted resonator frequency

$$\omega_r = \omega_r'' \left( 1 + \frac{C_g^2}{C_\Sigma C_r} + 2 \frac{C_c}{C_r} \left( 1 + \frac{C_g^2}{C_\Sigma C_r} \right) \right), \quad (5.9)$$

and the remaining term in 5.8 describes tunneling of photons between neighbouring resonators. Next, we explain how the simplified Hamilton operator  $H^{(2)} = \sum_i (H_{1\text{-site},i}^{(2)} + H_{J,i,i+1}^{(1)})$  can be transformed to a two component Bose-Hubbard Hamilton operator.

#### 5.1.4. The polariton modes

In the case of circuit QED with transmon qubits the coupling constant between microwave and qubit excitations is the dominating interaction energy of the system. Excitations of the whole system therefore can't be characterized as purely microwave or qubit excitations in general. To obtain a more suitable description we introduce new creation and annihilation operators,

$$c_+ = \cos(\theta)a + \sin(\theta)b \quad c_- = \sin(\theta)a - \cos(\theta)b, \quad (5.10)$$

describing excitations commonly termed polaritons where,

$$\sin(\theta) = \frac{g}{\sqrt{g^2 + (\Delta\omega + \sqrt{\Delta\omega^2 + g^2})^2}} \quad \cos(\theta) = \frac{\Delta\omega + \sqrt{\Delta\omega^2 + g^2}}{\sqrt{g^2 + (\Delta\omega + \sqrt{\Delta\omega^2 + g^2})^2}},$$

with  $\Delta\omega = \omega_r - \omega_q$ . The sine and cosine terms account for the transition of the character of the excitations from microwave to qubit excitations for the  $c_+$ -mode as the ratio  $E_J/E_C$  increases and vice versa for the  $c_-$ -mode. Expressing the Hamilton operator  $H^{(2)} = \sum_i (H_{1\text{-site},i}^{(2)} + H_{J,i,i+1}^{(1)})$  in the polariton modes (c.f. equation 5.10) we get,

$$H^{(2)} = H_{c_+,\text{lin}} + H_{c_-,\text{lin}} + H_{cc} + H_{\text{nl}}.$$

This Hamilton operator consists of two harmonic chains for the  $c_+$  and  $c_-$  polariton modes,

$$H_{c_+,\text{lin}} = \sum_i (\omega'_+ c_{i,+}^\dagger c_{i,+} - J_0 \cos^2(\theta) (c_{i,+}^\dagger c_{i+1,+} + h.c.))$$

$$H_{c_-,\text{lin}} = \sum_i (\omega'_- c_{i,-}^\dagger c_{i,-} - J_0 \sin^2(\theta) (c_{i,-}^\dagger c_{i+1,-} + h.c.)),$$

with  $\omega'_\pm = ((\omega_r + \omega_q) \pm \sqrt{\Delta^2 + g^2})/2$ , a term describing hopping from a  $c_-$ -mode at site  $i$  to a  $c_+$ -mode at site  $i + 1$  and all other possible combinations,

$$H_{cc} = -J_0 \sin(\theta) \cos(\theta) \sum_i (c_{i,+}^\dagger c_{i+1,-} + c_{i,-}^\dagger c_{i+1,+} + h.c.),$$

and a term describing the nonlinearity,

$$H_{\text{nl}} = \frac{-E_c}{12} \sum_i (\sin(\theta) (c_{i,+} + c_{i,+}^\dagger) - \cos(\theta) (c_{i,-} + c_{i,-}^\dagger))^4.$$

We assume the frequencies of the two polariton modes to be well separated, apply another rotating wave approximation where we neglect the term  $H_{cc}$  and convert the nonlinearity term  $H_{nlm}$  into Kerr form and get a renormalization of the polariton frequency and a density-density coupling between the polariton modes. This requires the difference in frequencies for the unperturbed modes  $\omega'_+ - \omega'_- = \sqrt{\Delta\omega^2 + g^2}$  involved to exceed the magnitude of the coupling between the modes and the nonlinearity,

$$\sqrt{\Delta\omega^2 + g^2} \gg J_0 \qquad \sqrt{\Delta\omega^2 + g^2} \gg \frac{E_C}{12}.$$

Plugging in realistic values for the parameters, extracted for example from [28], ( $E_C = 0.4\text{GHz}$ ,  $\omega_r = 43.6\text{GHz}$   $0 < E_J/E_C < 150$ ) we realize that the second inequality is indeed fulfilled. Engineering the capacitance  $C_c$  such that  $J_0$  is of the order of  $E_C/12$ , we can ensure that the first equality is fulfilled as well. The rotating wave approximation eliminates the intermode exchange coupling and we obtain a Bose-Hubbard Hamilton operator for both modes,  $c_+$  and  $c_-$ , with a density-density coupling between them,

$$H^{(3)} = H_{c_+} + H_{c_-} + H_{dd}, \quad (5.11)$$

where

$$\begin{aligned} H_{c_+} &= \sum_i \left( \omega_+ c_{i,+}^\dagger c_{i,+} - J_+ (c_{i,+}^\dagger c_{i+1,+} + h.c.) - \frac{U_+}{2} c_{i,+}^\dagger c_{i,+}^\dagger c_{i,+} c_{i,+} \right) \\ H_{c_-} &= \sum_i \left( \omega_- c_{i,-}^\dagger c_{i,-} - J_- (c_{i,-}^\dagger c_{i+1,-} + h.c.) - \frac{U_-}{2} c_{i,-}^\dagger c_{i,-}^\dagger c_{i,-} c_{i,-} \right) \\ H_{dd} &= - \sum_i 2U_{+-} c_{i,+}^\dagger c_{i,+} c_{i,-}^\dagger c_{i,-}, \end{aligned}$$

with

$$\begin{aligned} \omega_+ &= \omega'_+ + E_C (\cos^4(\theta) + \sin^2(\theta) \cos^2(\theta)) & \omega_- &= \omega'_- + E_C (\sin^4(\theta) + \sin^2(\theta) \cos^2(\theta)) \\ J_+ &= J_0 \cos^2(\theta) & J_- &= J_0 \sin^2(\theta) \\ U_+ &= E_C \sin^4(\theta) & U_- &= E_C \cos^4(\theta) \\ U_{+-} &= E_C \sin^2(\theta) \cos^2(\theta). \end{aligned}$$

We thus arrived at a two component Bose-Hubbard model for the modes  $c_+$  and  $c_-$  with attractive interactions and a density-density coupling between both species. The two species are a mixture of coplanar waveguide resonator field mode and transmon qubit excitations (c.f. equation 5.10) with different weights of the photonic or qubit contribution depending on the value of  $E_J/E_C$ .

For small values of  $E_J/E_C$  the  $c_+$  polaritons become increasingly microwave excitations. Consequently, their tunneling rate  $J_+$  approaches the tunneling rate of bare microwaves,  $J_0$ , and their on-site interaction  $U_+$  vanishes. For large  $E_J/E_C$ , on the other hand,  $J_+$  vanishes and the nonlinearity  $U_+$  approaches the nonlinearity of the transmon qubits,  $E_C$ . For the  $c_-$  polaritons, the roles of both limits are interchanged (c.f. figure 5.2).

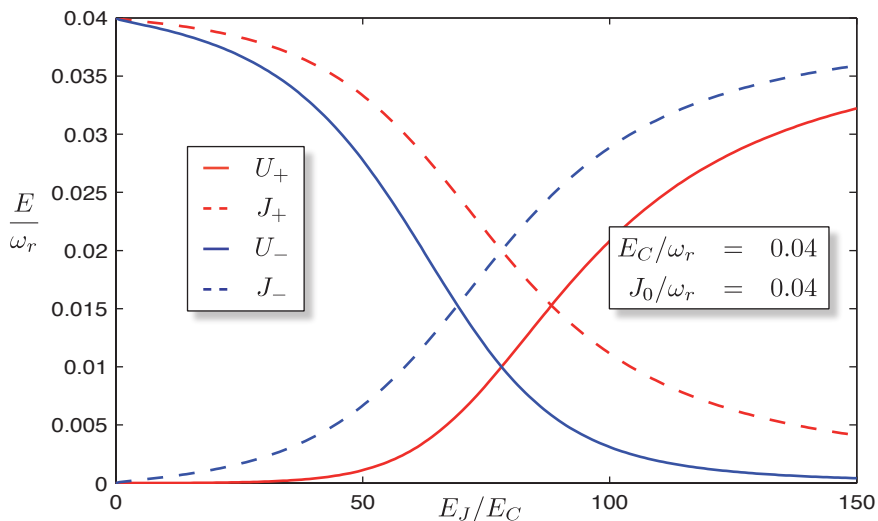


Figure 5.2.: Plot of the effective Bose-Hubbard parameters for the  $c_+$  polariton mode,  $U_+$  and  $J_+$ , and the  $c_-$  polariton mode,  $U_-$  and  $J_-$ . As the character of the polariton modes change as a function of  $E_J/E_C$  from resonator field mode to qubit excitation for the  $c_+$  polariton modes and vice versa for the  $c_-$  polariton modes the Bose-Hubbard parameters change accordingly.

For each value of  $E_J/E_C$ , the separation between the resonance frequencies of  $c_+$  and  $c_-$  polaritons,  $|\omega_+ - \omega_-|$ , is sufficiently large such that, in a scenario where we drive the first resonator by a microwave source, we can always adjust the frequency of the drive to only selectively excite one of the modes. For reasons that will become clear later we choose the  $c_+$ -polaritons to be our quantum simulator for a driven dissipative Bose-Hubbard model.

### 5.1.5. Validity of the approximations

To illustrate the validity of our approximations we compare the eigenenergies of the full Hamilton operator  $H$  (c.f. equation 5.1), approximated under rotating wave assumption (c.f. equation 5.6), with the eigenenergies of the Bose-Hubbard Hamilton operator  $H^{(3)}$  (c.f. equation 5.11). The single-site Hamilton operators summed up in the full Hamilton operator describe the interaction between transmon qubit and coplanar waveguide resonator in a rotating wave approximation. This Hamilton operator has already been used to describe an experiment revealing the nonlinear response of a resonator and transmon qubit system with excellent agreement between theory and experimental data [8]. Therefore comparison of the eigenvalues of our Bose-Hubbard Hamilton operator and the eigenvalues of the full Hamilton operator provides a good means to estimate the effects of the approximations we made. For simplicity we restricted our model to two sites.

Both Hamilton operators conserve the total number of excitations and we can diagonalize them in each subspace with a fixed number of excitations independently. Eigenvalues of the full Hamilton operator in the one excitation subspace are plotted in solid lines in figure 5.3 a). Without transmon qubits, the Hamilton operator of the two resonators has

eigenmodes  $a_{\pm} = (a_1 \pm a_2)/\sqrt{2}$ . In figure 5.3 a) we also plotted the energies of these eigenmodes of the two coupled empty coplanar waveguide resonators marked by two horizontal dash-dotted gray lines and the eigenenergy of the transmon qubit marked by a dash-dotted gray line.

The two eigenenergies approximated by the  $c_-$ -polariton mode (blue lines in 5.3 a) evolve from the transmon qubit energy for small values of  $E_J/E_C$  to the energies of the two coplanar waveguide resonator states for large values of  $E_J/E_C$  thereby confirming our earlier comment that the  $c_-$ -polaritons evolve from pure qubit excitations to microwave excitations. The eigenenergies of the  $c_-$  polaritons are degenerate for small values of  $E_J/E_C$  because the transmon qubits decouple from the coplanar waveguide resonators and thereby also from each other. In figure 5.3 b) we plot differences between the eigenenergies of the full Hamilton operator and the respective eigenenergies of the Bose-Hubbard Hamilton operator. For small values of  $E_J/E_C$  we find aberrations due to the error we make in approximating the Hamilton operator of the transmon qubit  $H_{1-site,i} \rightarrow H_{1-site,i}^{(1)}$ . There are also aberrations in the anticrossing area which are due to the neglected interactions between the  $c_+$ - and  $c_-$ -polaritons.

For the two eigenenergies of the  $c_+$ -polaritons (red lines in figure 5.3 a) there is a rather similar scenario. They approximate the two eigenenergies of the full Hamilton operator that are purely microwave excitations for small  $E_J/E_C$  and evolve into qubit excitations as the ratio of  $E_J/E_C$  increases. There are aberrations in the anticrossing area between the eigenenergies of the full Hamilton operator and the Bose-Hubbard Hamilton operator for the  $c_+$ -polaritons because of the neglected interactions between the  $c_-$ - and  $c_+$ -polaritons, plotted in figure 5.3 b) but there is no aberration for small values of  $E_J/E_C$  caused by errors made in the transmon qubit Hamilton operator because the  $c_+$ -polaritons are pure microwave excitations for small values of  $E_J/E_C$ .

Additionally to the differences between the eigenenergies of the full Hamilton operator and the Bose-Hubbard Hamilton operator in the one excitation subspace we plotted the differences in the two excitation subspace in figure 5.3 c). These eigenenergies can be grouped for the Bose-Hubbard Hamilton operator according to the distribution of excitations among the two polariton species. Differences of eigenenergies for states with two  $c_-$  polaritons are plotted in blue, for two  $c_+$  polaritons in red and for one  $c_-$  polariton and one  $c_+$  polariton in green. In the two excitation subspace we have similar findings as in the single excitation subspace. There are aberrations for the anti-crossing area because of the neglected intermode polariton exchange interaction. In addition, states containing  $c_-$  polaritons have aberrations for small values of  $E_J/E_C$  due to the approximations of the transmon Hamilton operator whereas  $c_+$  polaritons do not.

Therefore the Bose-Hubbard Hamilton operator for the  $c_+$  polaritons mimics the behaviour of the full Hamilton operator for the full range of  $E_J/E_C$ , provided the intersite coupling  $J_0$  is at most of the order of the on-site nonlinearity  $E_C$  and the polariton densities are not too high. To conclude: In a driven dissipative setup where we selectively excite the  $c_+$ -Polaritons we do have a quantum simulator for a Bose-Hubbard Hamilton operator.

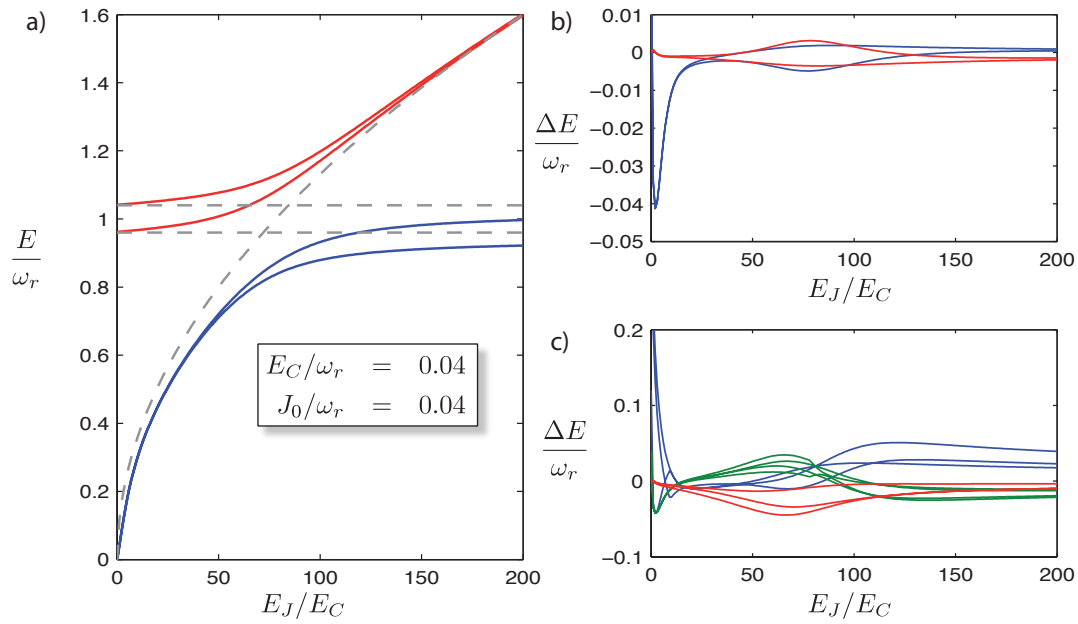


Figure 5.3.: The accuracy of our approximations. Plotted are the first four excited eigenvalues of the full Hamilton operator in figure a). Eigenvalues approximated by the  $c_-$  polaritons are plotted in blue and eigenvalues approximated by the  $c_+$  polaritons in red. Figures b) and c) show the differences between the eigenenergies of the full Hamilton operator  $H$  and the Bose-Hubbard Hamilton operator  $H^{(3)}$ ,  $\Delta E$ , in the one excitation and two excitation subspace respectively. Differences involving eigenstates containing  $c_-$  polaritons are plotted in blue and differences involving eigenstates containing  $c_+$  polaritons are plotted in red. Differences of eigenvalues of the full Hamilton operator and eigenvalues of the Bose-Hubbard Hamilton operator with mixed  $c_+$  and  $c_-$  parts are plotted in green

## 5.2. Polariton statistics in the driven dissipative regime

Quantum phases for the ground state and low temperature thermal states of the Bose-Hubbard Hamilton operator have been studied with ultra-cold atoms trapped in optical lattices [10]. This system has also been employed to study the dynamics of nonequilibrium states that were prepared by sudden quenches of some lattice parameters [33]. In contrast, a realisation in an array of coplanar waveguide resonators allows to investigate the Bose-Hubbard Hamilton operator in a fundamentally different regime, where the resonator array is permanently driven by coherent microwave sources to load it with microwave photons and thus compensate for the photons that are lost due to qubit relaxation and resonator decay. Whereas substantial understanding of equilibrium quantum phase transitions has been achieved, a lot less is known about these non-equilibrium scenarios where the dynamical balance between loading and loss mechanisms leads to stationary states. It is the investigation of these stationary states, that our approach to the simulation of the Bose-Hubbard Hamilton operator is ideally suited for.

Experiments with transmon qubits [48, 57] coupled to a coplanar waveguide resonator are often conducted without directly measuring the state of the qubit but by spectroscopically probing the transmission properties of the resonator. In an experiment the effective Bose-Hubbard Hamilton operator will thus be operated out of thermal equilibrium in a driven dissipative regime [36, 31, 14, 83]. In a suitable setup with a linear chain of resonators one would thus drive the first resonator with a coherent microwave input and measure the properties of the output signal at the opposite end of the chain.

In the regime we consider, this situation can be accurately described by a Bose-Hubbard Hamilton operator for only one species of polaritons with a coherent driving term at the first site and Markovian losses of polaritons due to cavity decay and qubit relaxation at all sites of the chain. In this scenario, the interplay of coherent drive and polariton loss leads to the emergence of steady states, for which we derive the particle statistics and characteristic correlations. In doing so we focus on the polariton statistics, in particular the density and density-density correlations, in the last resonator as these can be measured via the output signal. Our results show a transition from a coherent field to a field with strongly non-classical particle statistics as the ratio of on site interactions to driving strength is increased.

In this section we make use of the above explained mapping of the full Hamilton operator  $H$  to a two component Bose-Hubbard Hamilton operator  $H^{(3)}$  and consider a chain of coupled resonators, where we coherently drive the first resonator and adjust the microwave drive frequency to selectively excite the  $c_+$ -polaritons. In the driven dissipative regime we expect to explore new physics that go beyond the equilibrium features that are commonly examined in many body physics. We thus calculate the polariton density and the density-density correlations  $g^{(2)}$  in a master equation approach and analyse the dependencies on the system parameters  $J_+, U_+$  and the Rabi frequency of the microwave drive  $\Omega$ .

First experimental realisations of coupled coplanar waveguide resonators are expected to consist of only a few resonators. To closely approximate the expected experiments and to speed up numerical calculations, we thus focus on a minimal chain of only two resonators. More specifically, we consider two coplanar waveguide resonators coupled to transmon qubits, where the first coplanar waveguide resonator is driven by a microwave source and the output signal of the second cavity is monitored as a function of the mi-

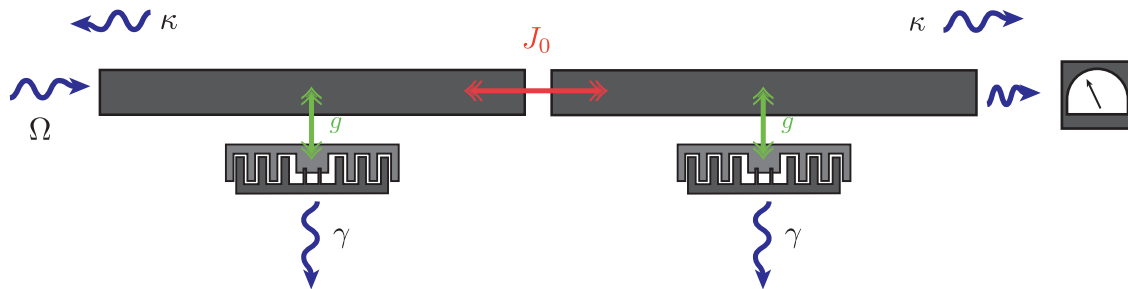


Figure 5.4.: Sketch of experimental setup consisting of two coplanar waveguide resonators coupled to transmon qubits with spectroscopic measurement technique: the first coplanar waveguide resonator is excited by coherent microwave source and the output field at the second cavity is monitored. coplanar waveguide resonators decay at rate  $\kappa$  mainly because of the finite reflectivity of the coupling capacitances and the transmon qubits decay Purcell enhanced at rate  $\gamma$  into modes not confined by the cavity.

crowave drive frequency and the ratio of  $E_J/E_C$  which can be controlled by applying an external magnetic flux to the dc-SQUID loop of the transmon qubits c.f. 5.4. This setup and very similar setups have been investigated in experiments for example [43], and the spectroscopic measurement technique proposed here has already been demonstrated in single site experiments for example in [89].

The output fields emanating from the second resonator are linear functions of the field in the second resonator and thus show the same particle statistics. We therefore calculated the polariton density and the  $g^{(2)}$ -function for the second cavity. To do this, we use a master equation approach in which each element, the coplanar waveguide resonators and the transmon qubits, couple to separate environments with decay rates denoted  $\kappa$  for the coplanar waveguide resonators and  $\gamma$  for the transmon qubits. Absolute values can for example be extracted from [8] where  $\gamma = 3.7\text{MHz}$ . Decay of the coplanar waveguide resonator is due to the finite transparency of the coupling capacitors at both ends of the resonators and decay rates for example in [28] are  $\kappa = 5.7\text{MHz}$ . Both environments, for the transmon qubit and the coplanar waveguide resonator, are assumed to be in a vacuum state which is a valid assumption at typical temperatures for circuit QED experiments of  $T = 15\text{mK}$ . Therefore in a master equation for a Hamilton operator expressed in the operators for the resonator field  $a$  and the transmon qubit  $b$  the dissipators read,

$$\frac{\kappa}{2}\mathcal{D}[a, a]\rho + \frac{\gamma}{2}\mathcal{D}[b, b]\rho,$$

with

$$\mathcal{D}[A, B]\rho = 2A\rho B^\dagger - (A^\dagger B\rho + \rho A^\dagger B).$$

These can be cast into dissipators expressed in the polariton modes  $c_+$  and  $c_-$ ,

$$\begin{aligned} \frac{\kappa}{2}\mathcal{D}[a, a]\rho + \frac{\gamma}{2}\mathcal{D}[b, b]\rho &= \Gamma_{c_+}\mathcal{D}[c_+, c_+]\rho + \Gamma_{c_-}\mathcal{D}[c_-, c_-]\rho + \\ &+ \Lambda(\mathcal{D}[c_+, c_-] + \mathcal{D}[c_-, c_+])\rho, \end{aligned}$$



with

$$\begin{aligned}\Gamma_{c_+} &= \frac{\kappa \cos^2(\theta) + \gamma \sin^2(\theta)}{2} \\ \Gamma_{c_-} &= \frac{\kappa \sin^2(\theta) + \gamma \cos^2(\theta)}{2} \\ \Lambda &= \sin(\theta) \cos(\theta) \frac{\kappa - \gamma}{2}.\end{aligned}$$

In the driven dissipative case where we selectively excite the polariton  $c_+$  mode we can neglect the dissipators of the  $c_-$  polaritons  $\mathcal{D}[c_-, c_-]$  and the mixed dissipators  $\mathcal{D}[c_+, c_-]$  and  $\mathcal{D}[c_-, c_+]$ . With these assumptions the master equation for a two site chain of the polariton  $c_+$ -mode reads,

$$\frac{d\rho}{dt} = i[\rho, \tilde{H}_{c_+}] + \Gamma_{c_+} (\mathcal{D}[c_{+,1}, c_{+,1}]\rho + \mathcal{D}[c_{+,2}, c_{+,2}]\rho) \quad (5.12)$$

$$\tilde{H}_{c_+} = \Omega \cos(\theta) (c_{+,1}^\dagger + c_{+,1}) + H_{c_+}.$$

To solve this master equation numerically we use it to derive the coupled equations of motion for the expectation values of normally ordered moments of the creation and annihilation operators  $c_{+,1}^\dagger, c_{+,1}, c_{+,2}^\dagger$  and  $c_{+,2}$ ,

$$\frac{d}{dt} \langle c_{+,1}^{\dagger n} c_{+,2}^{\dagger m} c_{+,1}^k c_{+,2}^l \rangle = \text{Tr} [\dot{\rho} c_{+,1}^{\dagger n} c_{+,2}^{\dagger m} c_{+,1}^k c_{+,2}^l]$$

We truncate this set of coupled equations by omitting couplings to mean values with  $n + m + k + l$  bigger than some  $n_{\max}$  and solve the reduced set of equations of motion. To confirm the accuracy of our approach, we test its convergence with increasing  $n_{\max}$ . That is, we repeat the procedure for  $n_{\max} \rightarrow n_{\max} + 1$ , compare the results and increase the value for  $n_{\max}$  in case both results differ by more than some required threshold value. The advantage with respect to a method that truncates the Hilbert space at some maximal number of excitations, is that our method becomes exact in the limit where the Hamilton operator becomes harmonic which is the case for small values of  $E_J/E_C$ . Moreover we experience a substantial decrease in cpu-time for this method.

### 5.2.1. Polariton density

We are interested in the field particle statistics in the driven dissipative regime and its dependencies of the on-site nonlinearity  $U_+$ , the intersite coupling  $J_+$  and the strength of the microwave drive  $\Omega$ . We therefore first consider the density of  $c_+$  polaritons in the last resonator. Figure 5.5 shows the density of  $c_+$  polaritons,  $\langle c_2^\dagger c_2 \rangle$ , in the second cavity as a function of the ratio  $E_J/E_C$  and the microwave drive frequency  $\omega_{\mu\nu}$ . The density of polaritons in the last cavity exhibits resonances when the microwave drive frequency matches one of the transition energies of the undriven conservative system Hamilton operator  $H_{c_+}$  and decreases rapidly because of the small decay rate  $\Gamma$ . One can clearly see the resonances due to transitions driven between the groundstate and eigenenergies in the one excitation subspace plotted in 5.3 a). Transitions from the groundstate into a two excitation state are much weaker owing to the finite Rabi frequency of the microwave drive  $\Omega$ .

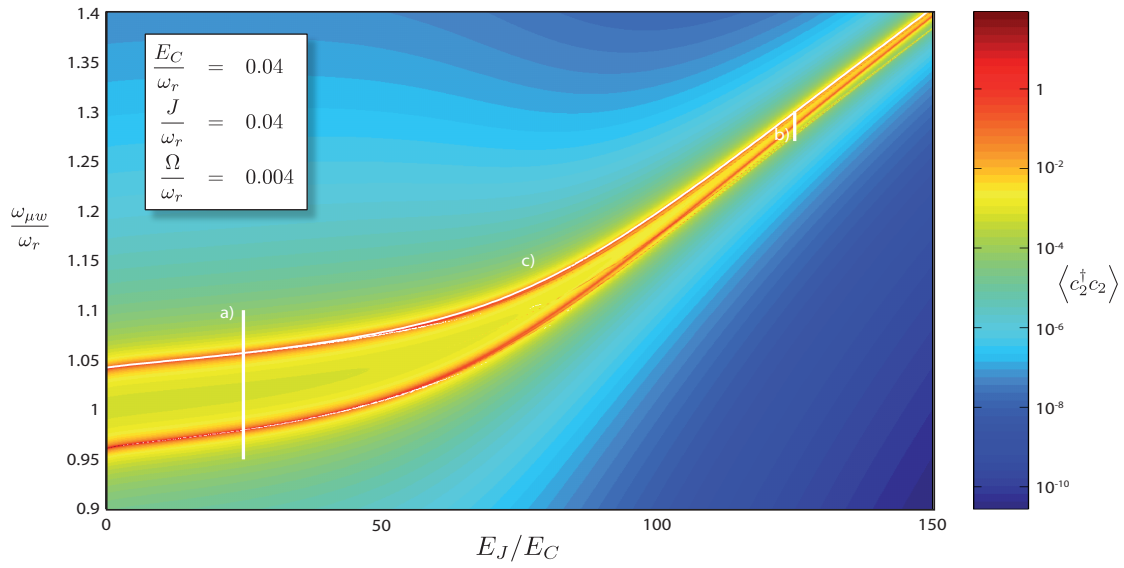


Figure 5.5.: Logarithmic density plot of the polariton density  $\langle c_2^\dagger c_2 \rangle$  in the last cavity plotted against  $E_J/E_C$  and the frequency of the microwave drive in units of the frequency of the coplanar waveguide resonator  $\omega_{\mu w}/\omega_r$ . Resonances in the density of polaritons arise where the microwave frequency matches one of the transition frequencies of the non-driven conservative system Hamilton operator  $H_{C_+}$

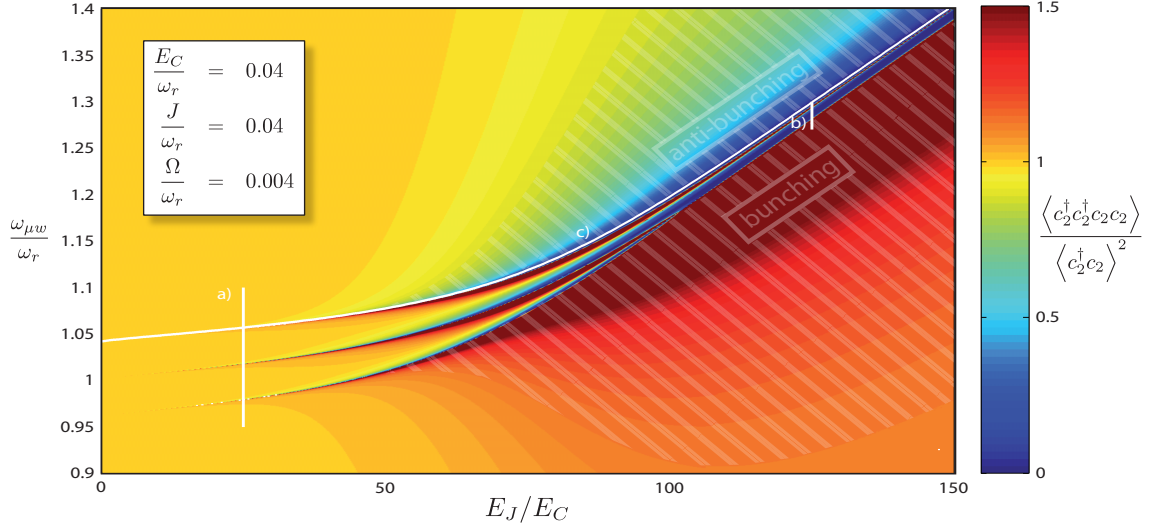


Figure 5.6.: Density plot of the  $g^{(2)}$ -function of the polariton mode in the second cavity plotted against  $E_J/E_C$  and the frequency of the microwave drive in units of the frequency of the coplanar waveguide resonator  $\omega_{\mu w}/\omega_r$ . For increasing nonlinearity the  $g^{(2)}$ -function shows bunching regions for red-detuned microwave drive with respect to the energy of 1-excitation states and anti-bunching regions for blue-detuned microwave drive.

### 5.2.2. Density-density correlations

We now consider the density-density correlations  $g^{(2)}$  in the last resonator. The  $g^{(2)}$ -function is a quantity that describes the likelihood to measure two photons at the same place. The  $g^{(2)}$  function of the last resonator is the normalized meanvalue of the second order moment of the field operators in the last resonator,

$$g^{(2)}(c_{+,2}) = \frac{\langle c_{+,2}^\dagger c_{+,2}^\dagger c_{+,2} c_{+,2} \rangle}{\langle c_{+,2}^\dagger c_{+,2} \rangle^2}.$$

Classical, thermal fields have  $g^{(2)}$ -values larger or equal to unity with the coherent field exhibiting a  $g^{(2)}$ -value of 1. A  $g^{(2)}$ -value below 1, meaning that the photons are anti-bunched, is a sufficient condition to call the field quantum mechanical in the sense that there is no classical field showing the same results in measurements of the  $g^{(2)}$ -function. Using previously developed refinements of microwave measurement techniques [63, 5], measurements of  $g^{(2)}$ -functions in circuit QED are now possible [12].

In figure 5.6 we plotted the  $g^{(2)}$ -function of the field in the last coplanar waveguide resonator. To get a more detailed insight of the processes leading to a  $g^{(2)}$ -value for specific parameters we plotted the  $g^{(2)}$ -function along special values of the microwave drive frequency and the ratio  $E_J/E_C$  marked by white lines in figure 5.6. Figures 5.7 and 5.8 show the results for the different paths, denoted by a), b), and c) in the density plot of the  $g^{(2)}$ -function in 5.6, for the  $g^{(2)}$ -function as well as the corresponding values for the density of

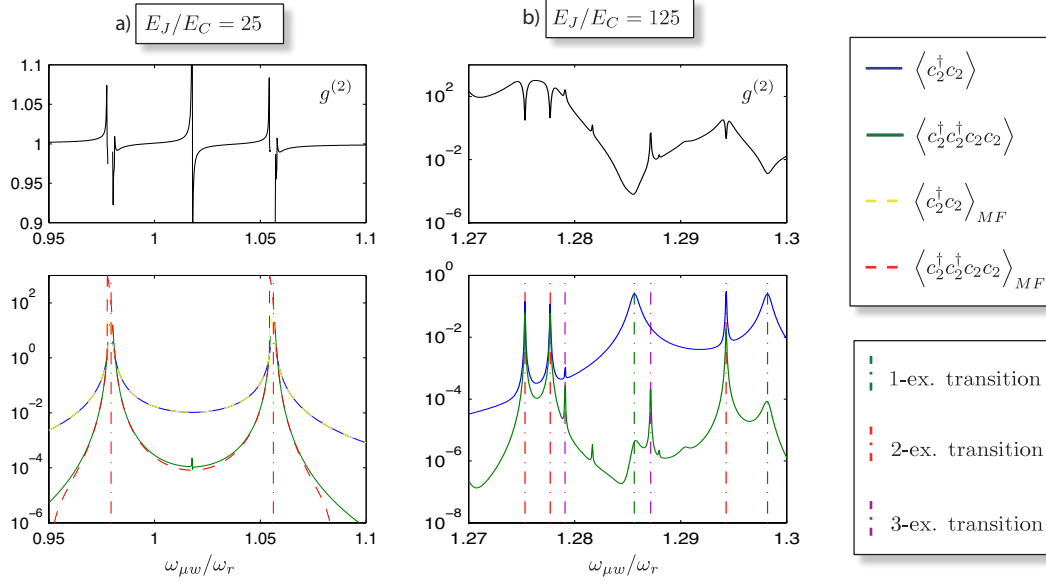


Figure 5.7.: Plots of the  $g^{(2)}$ -function, the density of polaritons  $\langle c_2^\dagger c_2 \rangle$  and the second order moment  $\langle c_2^\dagger c_2^\dagger c_2 c_2 \rangle$  in the second cavity for special values of  $E_J/E_C$  are shown. For all plots we have chosen the intersite coupling constant and the on-site nonlinearity to be  $J_0/\omega_r = 0.04$  and  $E_C/\omega_r = 0.04$  and the decay rates of transmon qubit and coplanar waveguide resonator to be  $\gamma/\omega_r = 0.00008$  and  $\kappa/\omega_r = 0.00004$  respectively but we applied different Rabi frequencies of the microwave drive: for a)  $\Omega/\omega_r = 0.004$ , and for b)  $\Omega/\omega_r = 0.001$ . Plotted are results obtained by numerical calculation of the masterequation in solid lines and results obtained by a mean field approach with an exact single-site solution in dashed lines. Eigenenergies of the system without dissipation and driving are signaled by vertical dash-dotted lines. For  $E_J/E_C = 25$  one can see clearly separated resonances for the symmetric and antisymmetric states  $d_{\pm}^\dagger |00\rangle$  and a two photon resonance for the state  $d_+^\dagger d_-^\dagger |00\rangle$ . The shape of the resonances at  $d_+^\dagger |00\rangle$  and  $d_-^\dagger |00\rangle$  are reproduced by the meanfield approximation and therefore for a single mode feature. The two photon resonance for the state  $d_+^\dagger d_-^\dagger |00\rangle$  is not reproduced by the meanfield approach since it does not correctly incorporate the interactions between  $d_+^\dagger$  and  $d_-^\dagger$  modes. For  $E_J/E_C = 125$  multiple resonances determined by the eigenenergies of the system without dissipation and driving arise.

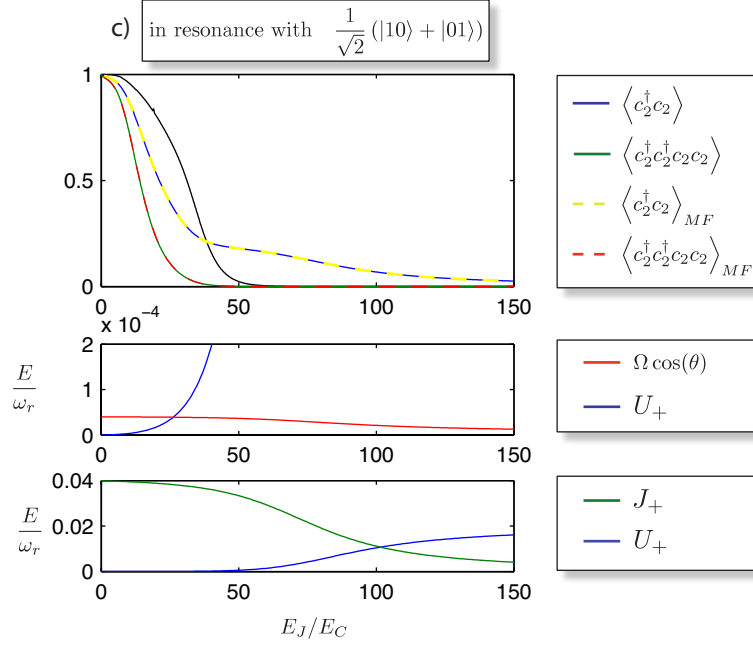


Figure 5.8.: A plot of the  $g^{(2)}$ -function, the density of polaritons  $\langle c_2^\dagger c_2 \rangle$  and the second order moment  $\langle c_2^\dagger c_2^\dagger c_2 c_2 \rangle$  in the second cavity is shown. The microwave drive frequency is chosen to match the transition from the ground state to the symmetric 1-excitation eigenstate. For all plots we have chosen the intersite coupling constant and the on-site nonlinearity to be  $J_0/\omega_r = 0.04$  and  $E_C/\omega_r = 0.04$ , the decay rates for transmon qubit and coplanar waveguide resonator to be  $\gamma/\omega_r = 0.00004$  and  $\kappa/\omega_r = 0.00008$  respectively and the Rabi frequency of the microwave drive to be  $\Omega/\omega_r = \Gamma/\omega_r = 0.00004$ . Plotted are results obtained by numerical calculation of the masterequation in solid lines and results obtained by a mean field approach with an exact single-site solution in dashed lines. In resonance to the symmetric state  $g^{(2)}$  shows a transition from uncorrelated coherent field particle statistics to anti-bunched correlated field particle statistics. The transition from coherent to anti-bunched is determined by the interplay of the Rabi frequency of the microwave drive and the on-site nonlinearity.

polaritons in the last cavity,  $\langle c_{+,2}^\dagger c_{+,2} \rangle$ , and the second order moment,  $\langle c_{+,2}^\dagger c_{+,2}^\dagger c_{+,2} c_{+,2} \rangle$ .

For small values of  $E_J/E_C$  our system is basically linear because the nonlinearity  $U_+/2 = (E_C/2) \sin^4(\theta)$  is negligible. A harmonic field mode driven by a coherent source is in a coherent state. Therefore the  $g^{(2)}$ -function is equal to one for small values of  $E_J/E_C$ . As the nonlinearity grows for increasing values of  $E_J/E_C$  the  $g^{(2)}$ -function plotted against the ratio of  $E_J/E_C$  and the frequency of the microwave drive  $\omega_{\mu w}$  becomes more structured. In the density plot of the  $g^{(2)}$ -function in 5.6 we can identify resonances where the frequency of the microwave drive matches the eigenenergies of the unperturbed system without microwave drive and dissipation. These resonances manifest themselves as separating lines between bunching regions (values of  $g^{(2)} > 1$ ) and anti-bunching regions (values of  $g^{(2)} < 1$ ).

To understand the origin of these separating lines, it is illustrating to analyze our system in terms of a symmetric mode,  $d_+$ , and an antisymmetric mode,  $d_-$ , where

$$d_{\pm} = \frac{1}{\sqrt{2}} (c_{+,1} \pm c_{+,2})$$

rather than the two localized modes  $c_{+,1}$  and  $c_{+,2}$ . In terms of  $d_+$  and  $d_-$  the Hamilton operator reads,

$$\begin{aligned} H_{c_+} = & (\omega_+ - J_+) d_+^\dagger d_+ + (\omega_+ + J_+) d_-^\dagger d_- - \frac{U_+}{4} (d_+^\dagger d_+^\dagger d_+ d_+ + d_-^\dagger d_-^\dagger d_- d_-) \\ & - U_+ d_+^\dagger d_+ d_-^\dagger d_- - \frac{U_+}{4} (d_+^\dagger d_+^\dagger d_- d_- + h.c.) . \end{aligned} \quad (5.13)$$

The Hilbert space of the Hamilton operator  $H_{c_+}$  can be described by two different bases, states that are labeled by the number of excitations in the collective modes,

$$\frac{(d_+^\dagger)^n (d_-^\dagger)^m}{\sqrt{n!} \sqrt{m!}} |00\rangle = |nm\rangle_{cm} ,$$

or states that are labeled by the number of excitations in the localized modes,

$$\frac{(c_{+,1}^\dagger)^n (c_{+,2}^\dagger)^m}{\sqrt{n!} \sqrt{m!}} |00\rangle = |nm\rangle_s .$$

The lines separating bunching and anti-bunching regions in figure 5.6 can now be identified with the energies of the 1 excitation states,

$$d_+ |00\rangle = |10\rangle_{cm} = \frac{1}{\sqrt{2}} (|10\rangle_s + |10\rangle_s) \quad (5.14)$$

$$d_- |00\rangle = |10\rangle_{cm} = \frac{1}{\sqrt{2}} (|10\rangle_s - |10\rangle_s) \quad (5.15)$$

and the energy of a 2-excitation state,

$$d_+^\dagger d_-^\dagger |00\rangle = |11\rangle_{cm} = \frac{1}{\sqrt{2}} (|20\rangle_s - |02\rangle_s) . \quad (5.16)$$

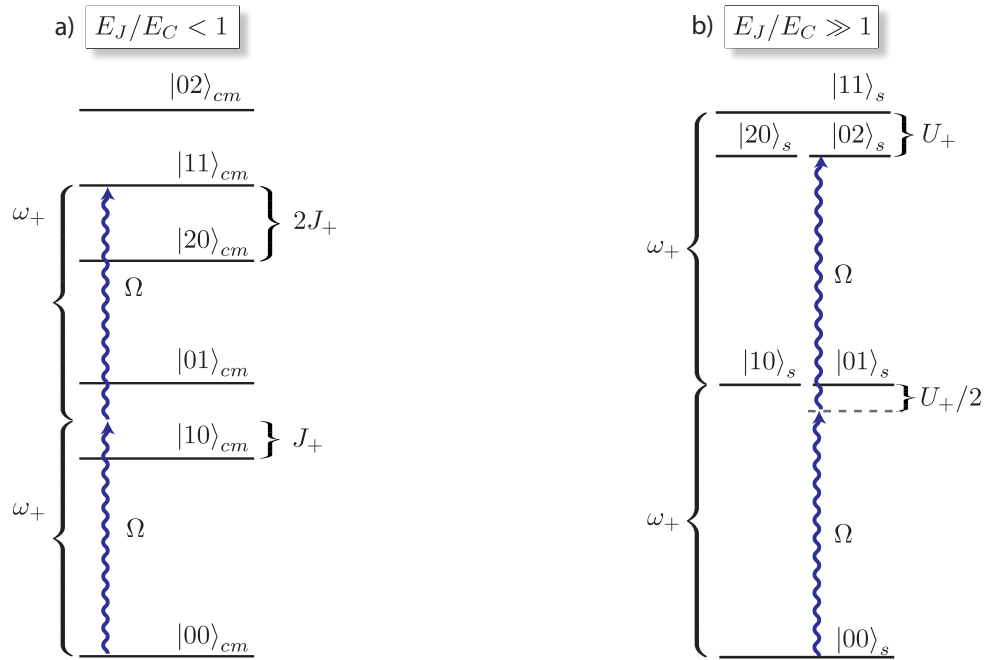


Figure 5.9.: Sketch of the energy spectrum of the Bose-Hubbard Hamilton operator  $H_{c,+}$  for a two site model for vanishing nonlinearity  $U_+$  compare a) and vanishing intersite coupling  $J_+$  compare b). For vanishing nonlinearity a microwave drive can drive multiple transitions leading to a coherent state. Contrary to the linear case for strong nonlinearity one can only drive a transition between two distinct states as the energy differences between the eigenenergies aren't degenerate any more

To understand the origin of the anti-bunching regions for a microwave drive that is blue detuned with respect to the energies of the states (5.14-c) and the bunching regions for a red detuned microwave drive one has to consider the spectrum of the Hamilton operator  $H_{c_+}$ .

For small nonlinearity, that is for values of  $E_J/E_C < 50$ , the Hamilton operator 5.13 reduces to a Hamilton operator for two uncoupled harmonic oscillators described by the modes  $d_+$  and  $d_-$  with energies  $\omega_+ - J_+$  and  $\omega_+ + J_+$  respectively. The eigenenergies in this situation are shown in 5.9 a). A microwave drive with frequency  $\omega_+ - J_+$  as depicted in 5.9 not only drives the transition from the groundstate to the first excited state of the symmetric collective mode  $|00\rangle_{cm} \rightarrow |10\rangle_{cm}$  but also all other transitions to higher excited states  $|n0\rangle_{cm} \rightarrow |n+10\rangle_{cm}$ . As a result the steady state in this situation is always the coherent state exhibiting a  $g^{(2)}$ -value of 1. For slightly increased values of the nonlinearity that remain in the range  $U_+ < \Gamma_{c_+}$ , the system can still be described in terms of two weakly interacting collective modes. But the symmetric as well as the antisymmetric mode are subject to the nonlinearity and an intermode interaction, c.f. Hamilton operator 5.13. This can be seen in 5.7 a) where we plotted the  $g^{(2)}$ -values that deviate from the value of a coherent field. The  $g^{(2)}$ -function shows anti-bunching regions for blue detuned microwave drive with respect to the energies of the states (5.14-c) and bunching regions for red detuned microwave drive. To gain insight into the underlying physical principles in this situation we calculated the density  $\langle c_{+,2}^\dagger c_{+,2} \rangle$  and the second symmetric moment  $\langle c_{+,2}^\dagger c_{+,2}^\dagger c_{+,2} c_{+,2} \rangle$  by an iterative meanfield approach (c.f. subsection 5.2.3) to solve the master equation 5.12 with the Hamilton operator written as in 5.13. Operator mean values of a single driven dissipative mode with Kerr nonlinearity can be computed exactly [23] and we expand this model in a meanfield way to incorporate the density-density coupling. With this method we get good agreement with the numerical exact values for the density in the last cavity and are able to compute values for the polariton density close to the systems eigenenergies (5.14-c) where our numerical approach fails to converge. For details about the method please see subsection 5.2.3. These results support our assertion that the system can be described by weakly interacting collective modes in the limit of small nonlinearities  $U_+$ . In 5.7 a) numerically exact values are plotted in solid lines and values obtained by the above mentioned mean field method are plotted in dashed lines.

For strong nonlinearity  $U_+$  and small intersite coupling  $J_+$ , that is for values of  $E_J/E_C > 50$ , the  $c_+$ -polaritons become transmon excitations and the Hamilton operator  $H_{c_+}$  splits into two parts describing the first and the second transmon qubit respectively. Here the collective modes  $d_+$  and  $d_-$  no longer decouple and the localized modes  $c_1$  and  $c_2$  become a more appropriate description of the system. The eigenenergy spectrum in this situation is shown in 5.9 b). The main difference to the spectrum without nonlinearity is that the microwave drive can't be adjusted to drive multiple transitions. In order to drive the transition to the state  $|02\rangle_s$  for example one has to adjust the microwave frequency to match half of the energy difference between the groundstate and the 2-excitation state  $|02\rangle_s$  because it is a two photon transition. Due to the anharmonicity of the eigenenergy spectrum no other transition can be driven. The difference of microwave frequencies needed to drive the transition from groundstate to  $|01\rangle_s$  respectively  $|02\rangle_s$  amounts to  $U_+/2$  which is bigger than the linewidth  $\Gamma_{c_+}$ . To get an estimate for the value of  $g^{(2)}$  we simplify our model assuming that the frequency of the microwave drive is adjusted such that it reso-



nantly drives a transition between the groundstate of our model  $|00\rangle_s$  and some excited state  $|0n\rangle_s$ . Provided the Rabi frequency  $\Omega$  and the loss rates  $\kappa$  and  $\gamma$  are all small compared to the frequency separation between different resonance lines, the system can then be modeled by a two level system consisting of the groundstate of our model  $|00\rangle_s$  and the excited state  $|0n\rangle_s$ . In this situation the maximal occupation inversion one could get in the steady state is,

$$\rho_{max} = \frac{1}{2} (|00\rangle \langle 00| + |0n\rangle \langle 0n|) ,$$

and the  $g^{(2)}$ -value for this density matrix would be

$$g^{(2)} = \frac{\text{tr} [\rho_{max} c_{+,2}^\dagger c_{+,2}^\dagger c_{+,2} c_{+,2}]}{(\text{tr} [\rho_{max} c_{+,2}^\dagger c_{+,2}])^2} = \frac{2n(n-1)}{n^2}$$

which is below one for a 1-excitation state and above one for every state containing more than 2 excitations. Therefore bunching areas arise if states containing more than 2-exciations are excited and anti-bunching areas arise if only 1-excitation states can be excited and the photons pass the setup "one by one". In our Bose-Hubbard model the on-site nonlinearity is negative and hence all transition frequencies to states containing more than two excitations are red detuned with respect to transition frequencies to states containing only one excitation (5.14-c). This is why bunching areas arise for red detuned microwave drive and anti bunching areas arise for blue detuned microwave drive.

If we adjust the microwave drive frequency for every value of  $E_J/E_C$  to match the eigenfrequency of the antisymmetric 1-excitation state we get the transition from a perfectly uncorrelated field with  $g^{(2)} = 1$  to strongly correlated, anti-bunched field statistics with  $g^{(2)} < 1$  see 5.8. For a quantum phase transition of the ground state of the Bose-Hubbard Hamilton operator one would expect this transition as a consequence of the interplay of the intersite hopping  $J_+$  and the on-site nonlinearity  $U_+$ . For the driven dissipative system we observe that the interplay between the Rabi frequency of the microwave drive  $\Omega \cos(\theta)$  and the on-site nonlinearity  $U_+$  determines the particle statistics. This can be seen in 5.8 where we plotted the  $g^{(2)}$ -function and the intersite coupling, on-site nonlinearity and the Rabi frequency of the microwave drive.

### 5.2.3. Meanfield approximation for two coupled modes with small nonlinearity

We want to solve the master equation 5.12 for small values of  $E_J/E_C$ . For  $E_J/E_C = 25$ , we find  $J_+ \gg U_+$  and express Hamilton operator  $\tilde{H}_{c_+}$  in terms of the collective modes  $d_+$  and  $d_-$ ,

$$\tilde{H}_{c_+} = \tilde{H}_{d_+} + \tilde{H}_{d_-} + H_{dd} + H_{ex}$$

where,

$$\tilde{H}_{d_\pm} = \frac{\Omega \cos(\theta)}{\sqrt{2}} (d_\pm^\dagger + d_\pm) + (\Delta\omega_+ \pm J_+) d_\pm^\dagger d_\pm - \frac{U_+}{4} d_\pm^\dagger d_\pm^\dagger d_\pm d_\pm$$

$$H_{dd} = -U_+ d_+^\dagger d_+ d_-^\dagger d_-$$

$$H_{ex} = -\frac{U_+}{4} (d_+^\dagger d_+^\dagger d_- d_- + h.c.) .$$

Here  $\Delta\omega_+ = \omega_+ - \omega_l$  is the difference between the frequency  $\omega_+$  and the microwave drive frequency  $\omega_l$ . Since  $J_+ \gg U_+$ , the two collective modes are energetically far separated and we neglect  $H_{ex}$  in a rotating wave approximation. In zeroth order in our approximation we neglect  $H_{dd}$  as well and decouple the collective modes completely. The driven dissipative master equation for the collective modes  $d_+$  and  $d_-$  with Hamilton operators  $H_{d_+}$  and  $H_{d_-}$  can be solved exactly for steady state values, c.f. [23]. We compute the densities of the two collective modes  $\langle d_{\pm}^\dagger d_{\pm} \rangle = \delta_{\pm}^{(0)}$  in zeroth order approximation and use them to approximate the intermode density-density coupling,

$$-U_+ d_+^\dagger d_+ d_-^\dagger d_- \rightarrow -\frac{U_+}{2} \left( d_+^\dagger d_+ \delta_-^{(0)} + \delta_+^{(0)} d_-^\dagger d_- \right).$$

This way the modes are still decoupled but the density of the  $d_+$ -mode induces a frequency shift of the  $d_-$ -mode  $\omega_+ - J_+ \rightarrow \omega_+ - J_+ - U_+ \delta_+^{(0)}$  and vice versa. We proceed to calculate the densities of the two modes with the shifted frequencies to obtain the densities of the two modes in first order approximation  $\delta_{\pm}^{(1)}$ . We iterate this method until the difference between densities of consecutive order in approximation is smaller than some threshold value. After this procedure we approximate the density in the last coplanar waveguide resonator

$$\langle c_{+,2}^\dagger c_{+,2} \rangle \rightarrow \frac{1}{2} \left( \langle d_+^\dagger d_+ \rangle + \langle d_-^\dagger d_- \rangle \right) + \text{Re} \left[ \langle d_+^\dagger \rangle \langle d_- \rangle \right]$$

where we calculated the values for  $\langle d_+^\dagger \rangle$  and  $\langle d_- \rangle$  with the renormalized frequencies  $\omega_+ + J_+ - U_+ \delta_-^{(n_{max})}$  and  $\omega_+ - J_+ - U_+ \delta_+^{(n_{max})}$ . With this procedure we can reproduce the numerically exact values for the density in the last coplanar waveguide resonator and are able to compute values for the polariton density close to the systems eigenenergies (5.14-c) where the numerically exact method converges very slowly and becomes numerically very demanding.

## 6. Josephson Junction Intersected Resonators

In the previous chapter we considered a set of coplanar waveguide resonators each coupled to a superconducting charge qubit as a artificial system of bosons, or more precisely photons, to study the interplay between their on-site interaction mediated by the nonlinearity of the charge qubit and the hopping between the resonators. As a consequence of the strong coupling between each individual coplanar waveguide resonator and its charge qubit, it is more convenient to describe the elementary excitations of the system in terms of polaritons. Polaritons are coherently combined excitations of the coplanar waveguide resonator and the charge qubit. They inherit the ability to jump between different coplanar waveguide resonators from their photonic nature and the ability to interact on each individual site from their partial existence as a charge qubit excitation. Due to their twofold nature however they also come in two flavors, the upper and lower polariton, named because of its higher and lower energy respectively. If we consider the coplanar waveguide resonator and charge qubit to be on resonance, their polaritons are separated in energy space by the coupling energy between resonator and qubit. This coupling energy is not large enough to get an efficient separation of the two polariton species, albeit large compared to setups in the optical regime. To further increase the coupling between the charge qubit and the coplanar waveguide resonator one might couple them via the current in the resonator rather than by the charge as previously done. This means incorporating the Josephson junction directly into the central conductor of the coplanar waveguide resonator. In the following we will show that this greatly simplified setup actually can be interpreted as a ultrastrongly coupled charge qubit to a coplanar waveguide resonator. To accommodate our theoretical model to the ultrastrong coupling we change our way of thinking. We do not consider the resonator and the qubit as separate systems and treat their interaction as a perturbation but rather model them as an entity and treat the nonlinearity of the Josephson junction as perturbation.

### 6.1. Model Assumptions for the Josephson Junction Intersected Resonator

At first we consider a slightly more general setup of a coplanar waveguide resonator which is interrupted by  $N$  identical, capacitively shunted Josephson junctions with Josephson inductance  $L_J$  and shunting capacitance  $C_J$ . The Josephson junctions are regularly spaced with distance  $\Delta$ . The coplanar waveguide resonator supports one-dimensional voltage-current waves with wave velocity  $v = 1/\sqrt{l c}$  and characteristic wave impedance  $Z_c = \sqrt{l/c}$ . Where  $l$  and  $c$  are the inductance and capacitance per unit length of the coplanar waveguide respectively. The resonator is terminated on both ends open circuited and at the positions of the Josephson junctions the Josephson current-phase relations have to be fulfilled. Instead of the Josephson junctions one could also incorporate dc-SQUIDs, which

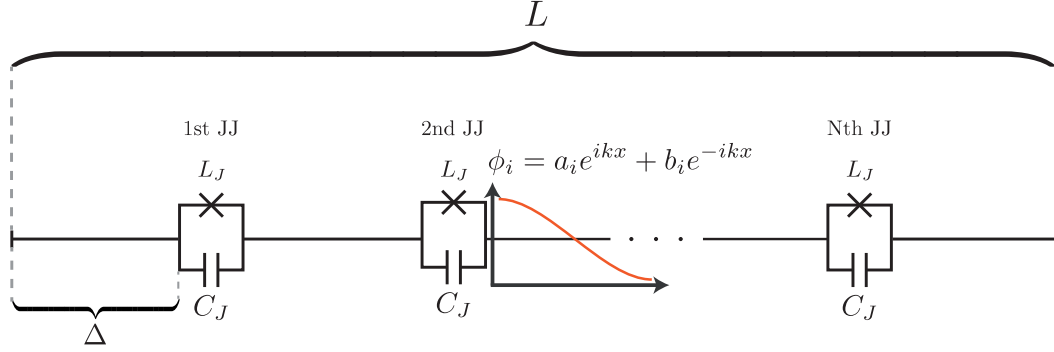


Figure 6.1.: Schematic sketch of the Josephson junction intersected resonator. The central line of a coplanar microwave resonator is intersected at equal distances  $\Delta$  by identical, capacitively shunted Josephson junctions with Josephson energy  $E_J$  and shunting capacitance  $C_J$ . The state of the coplanar waveguide resonator is fully defined by the flux functions at intermediary slices of coplanar waveguides  $\phi_i$

would enable in situ tuning of Josephson plasma frequencies  $\omega_p = 1/\sqrt{L_J C_J}$ . With this technique one could also smooth out inevitable production deviations between individual dc-SQUIDS. The state of the coplanar waveguide resonator is fully defined by the flux function  $\phi = \int_{-\infty}^t V(t') dt'$  in each slice of coplanar waveguide between the Josephson junctions. Physical observables like the excess charge per unit length,  $Q = c\dot{\phi}$ , or the current,  $I = (\partial_x \phi)/l$ , in the coplanar waveguide resonator may be derived from the flux function  $\phi$ . The Lagrangian for the whole system reads,

$$\mathcal{L} = \sum_{j=1}^{N+1} \mathcal{L}_j^{\text{CPW}} + \sum_{j=1}^N \mathcal{L}_j^{\text{JJ}}, \quad (6.1)$$

with,

$$\mathcal{L}_j^{\text{CPW}} = \int_{(j-1)\Delta}^{j\Delta} \left\{ \frac{c}{2} [\partial_t \phi(x, t)]^2 - \frac{1}{2l} [\partial_x \phi(x, t)]^2 \right\} dx$$

$$\mathcal{L}_j^{\text{JJ}} = \frac{C_J}{2} \delta\phi_j^2 + \frac{\varphi_0^2}{L_J} \cos\left(\frac{\delta\phi_j}{\varphi_0}\right),$$

where the Josephson junctions introduce a drop  $\delta\phi_i = \phi|_{x \nearrow j\Delta} - \phi|_{x \searrow j\Delta}$  in the flux function, that is the difference between the limit of the flux function approaching the Josephson junction from the left,  $\phi|_{x \nearrow j\Delta}$ , and from the right,  $\phi|_{x \searrow j\Delta}$ . Because the setup does not contain any flux threaded loops, that would require the sum of fluxes around the loop to equal the threaded flux modulo  $2\pi$ , the global minimum of the potential landscape of the setup is reached, when all flux drops at the Josephson junctions  $\delta\phi_i$  vanish and  $\phi = 0$  for all  $x \in [0, L]$ . At first we may linearize the Lagrangian around this global minimum, find the exact eigenmodes of the linearized Lagrangian and then investigate effects of the

nonlinearity in a perturbative manner. The nonlinearity is introduced solely by the cosine-potential of the Josephson junctions, therefore it suffices to consider only the quadratic part of the cosine-potential in order to get the linearized Lagrangian  $\bar{\mathcal{L}}$ ,

$$\mathcal{L}_j^{JJ} \rightarrow \bar{\mathcal{L}}_j^{JJ} = \frac{C_J}{2} \delta\phi_j^2 - \frac{1}{2L_J} \delta\phi_j^2. \quad (6.2)$$

## 6.2. Spectrum Calculation with Transfer Matrix Technique

With the help of the transfer matrix technique (c.f section 3.3 or citation [92]) we calculate the classical spectrum of eigenmodes of the coplanar waveguide resonator with Josephson junctions, henceforth called nonlinear resonator.

The flux function for the coplanar waveguide fulfills a wave equation,

$$\partial_t^2 \phi - v^2 \partial_x^2 \phi = 0. \quad (6.3)$$

An Ansatz with separation of the variables time  $t$  and space  $x$ ,  $\phi(x, t) = g(t)f(x)$ , leads us to the linear dispersion relation  $\omega = vk$ , with  $k$  the wavevector, and the fundamental solution for the spatial function of the flux  $f_j(x) = a_j(x) + b_j(x)$  ( $a_j(x) = \bar{a}_j e^{ikx}$ ,  $b_j(x) = \bar{b}_j e^{-ikx}$ ) of coplanar waveguide slice  $j$ , which stretches from  $x = (j-1)\Delta$  to  $j\Delta$ . Now the linearization of the Josephson current-flux relations (c.f. equation 6.2) emerges as an essential step to be able to separate the spatial and temporal functions in the equations of motion for the flux drops at the Josephson junctions. The nonlinear current-flux relation for Josephson junctions intertwines the spatial and temporal component beyond separability. However the linearized current-flux relations for the Josephson junctions,

$$-\partial_x \phi_j(\Delta) = -\partial_x \phi_{j+1}(0) = \frac{l}{L_J} \left( 1 - \frac{\omega^2}{\omega_p^2} \right) \delta\phi_j,$$

can be recast in identical 2 by 2 matrices  $S$  mapping positive and negative frequency components  $a_j(x)$  and  $b_j(x)$  directly to the left of the Josephson junction to their counterparts directly to the right of the Josephson junction (c.f. section 3.3),

$$\begin{pmatrix} a_{j+1}(0) \\ b_{j+1}(0) \end{pmatrix} = \underbrace{\begin{pmatrix} 1 + i\alpha & -i\alpha \\ i\alpha & 1 - i\alpha \end{pmatrix}}_S \begin{pmatrix} a_j(\Delta) \\ b_j(\Delta) \end{pmatrix},$$

where  $1/\alpha = 2l/(kL_J)(1 - \omega^2/\omega_p^2)$ . With the translational matrix  $T(\delta)$ , which propagates the flux function along the coplanar waveguide for the length  $\delta$ ,

$$\begin{pmatrix} a_j(x + \delta) \\ b_j(x + \delta) \end{pmatrix} = \underbrace{\begin{pmatrix} e^{ik\delta} & 0 \\ 0 & e^{-ik\delta} \end{pmatrix}}_{T(\delta)} \begin{pmatrix} a_j(x) \\ b_j(x) \end{pmatrix},$$

we define  $D = T(\Delta)$  and are able to propagate i.e. relate the wavefunction parameters  $a_1(0), b_1(0)$  at the left end of the nonlinear resonator to the wavefunction parameters  $a_{N+1}(\Delta), b_{N+1}(\Delta)$  at the right end of the nonlinear resonator,

$$\begin{pmatrix} a_{N+1}(\Delta) \\ b_{N+1}(\Delta) \end{pmatrix} = D(SD)^N \begin{pmatrix} a_1(0) \\ b_1(0) \end{pmatrix}. \quad (6.4)$$

Our goal is to find the eigenmodes of the nonlinear resonator. To this end we not only need the equations of motion for the flux function in the coplanar waveguide but we also need boundary conditions. Current has to vanish at the borders of the nonlinear resonator,  $\frac{1}{l}\partial_x\phi_1|_{x=0} = 0$  and  $\frac{1}{l}\partial_x\phi_{N+1}|_{x=\Delta} = 0$  which imposes the following conditions on the spatial flux function parameters,

$$a_1(0) - b_1(0) = 0 \qquad a_{N+1}(\Delta) - b_{N+1}(\Delta) = 0.$$

These conditions can be rewritten as a homogeneous linear equation for the wavefunction parameters  $a_1(0), b_1(0)$  with the help of eq. (6.4),

$$\begin{pmatrix} 1 & -1 \\ (1 & -1) \cdot D(SD)^N \end{pmatrix} \begin{pmatrix} a_1(0) \\ b_1(0) \end{pmatrix} = \begin{pmatrix} 0 \\ 0 \end{pmatrix}.$$

This homogeneous linear equation only has nontrivial solutions if the determinant of the coefficient matrix vanishes. We use this condition to determine the eigenfrequencies of the nonlinear resonator. To this end we express the scattering matrix that relates the wavefunction parameters at the left end of the nonlinear resonator to the wavefunction parameters at the right end of the nonlinear resonator,

$$D(SD)^N = D^{\frac{1}{2}}(D^{\frac{1}{2}}SD^{\frac{1}{2}})^N D^{\frac{1}{2}},$$

in terms of Pauli matrices  $\sigma_x, \sigma_y, \sigma_z$  and the 2 by 2 identity matrix  $\mathbb{1}$ ,

$$\begin{aligned} D^{\frac{1}{2}}SD^{\frac{1}{2}} &= \underbrace{(\cos(k\Delta) - \alpha \sin(k\Delta))}_{v_0} \mathbb{1} + \underbrace{i(\alpha \cos(k\Delta) + \sin(k\Delta))}_{v_z} \sigma_z \underbrace{-\alpha}_{v_y} \sigma_y \\ &= v_0 \mathbb{1} + \vec{v} \vec{\sigma}. \end{aligned} \quad (6.5)$$

Using the algebraic properties of the Pauli matrices we can further calculate arbitrary powers of the above matrix,

$$(D^{\frac{1}{2}}SD^{\frac{1}{2}})^N = \underbrace{\left( \sum_{n=0}^{\infty} \binom{N}{2n} v_0^{N-2n} (\vec{v} \cdot \vec{v})^n \right)}_{co(v)} \mathbb{1} + \underbrace{\left( \sum_{n=0}^{\infty} \binom{N}{2n+1} v_0^{N-1-2n} (\vec{v} \cdot \vec{v})^n \right)}_{si(v)} \vec{v} \vec{\sigma}.$$

This leads us to the following transcendental equation for the eigenenergies of the nonlinear resonator,

$$\sin(k\Delta) (co(v) + si(v)v_0) = 0.$$

$\sin(k\Delta) = 0$  singles out the eigenmodes of the bare coplanar waveguide resonator that do not couple at all to the Josephson junctions because the current for these specific modes vanishes at the positions of the Josephson junctions. The remaining factor can be simplified to,

$$\sum_{n=0}^{\infty} \binom{N+1}{2n+1} v_0^{N-2n} (v_0^2 - 1)^n = 0. \quad (6.6)$$

By virtue of the fundamental theorem of algebra we know that this equation has  $N$  solutions. Lets suppose for the moment that all  $N$  solutions for this equation  $v_{0,n}$  are real valued. This would provide us with  $N$  equations that can be deduced with the help of the definition of  $v_0$  (c.f. eq.6.5) and  $\alpha$ ,

$$\frac{\cos\left(\frac{\omega}{v}\Delta\right) - v_{0,n}}{\sin\left(\frac{\omega}{v}\Delta\right)} = \frac{cv}{2C_J} \frac{\omega}{\omega_p^2 - \omega^2}, \quad (6.7)$$

We could now proceed by trying to directly solve the equation (6.6) and deduce all  $N$  transcendental equations (6.7). But there is a more physical intuitive way to guess the solutions of (6.6): The coefficients of the polynomial (6.6) are all numerical constants, consequently all solutions  $v_{0,n}$  should also be numerical constants without further dependencies on the physical parameters defining the nonlinear resonator. If we are able to guess the  $v_{0,n}$  for a particular range of the physical parameters with the help of the equations (6.7), we found the general solutions valid for all values of the physical parameters. Now imagine a solution where the frequency of the eigenmode  $\omega$  is far detuned from the plasma frequency of the Josephson junctions  $\omega_p$ . The right hand side of (6.7) vanishes and the eigenmodes should be the free modes of the bare coplanar waveguide resonator without Josephson junctions with frequencies  $\omega_{n'} = (\pi v/L)n'$ ,  $n' \in \mathbb{N}$ . Therefore the left hand side of the equations (6.7) also has to vanish for far detuned bare coplanar waveguide resonator and Josephson junctions and consequently the solutions for equation (6.6) are  $v_{0,n} = \cos\left(n\frac{\pi}{N+1}\right)$ . Therefore all  $N$  transcendental equations for the eigenfrequencies are,

$$\frac{\cos\left(\frac{\omega}{v}\Delta\right) - \cos\left(n\frac{\pi}{N+1}\right)}{\sin\left(\frac{\omega}{v}\Delta\right)} = \frac{cv}{2C_J} \frac{\omega}{\omega_p^2 - \omega^2}, \quad (6.8)$$

where  $n \in [1, N]$ . Every transcendental equation for a specific  $n$  has a infinite number of solutions defining a manifold of eigenmodes with the same index  $n$ . We introduce the combined index  $i = \{n, k\}$  which indexes all eigenmodes irrespective of their manifold.

The spatial flux functions  $f_{j|i}$  can be determined by propagating the initial  $a_{1|i}(0)$  and  $b_{1|i}(0)$  from the left border of the nonlinear resonator to position  $x$  with the help of the transfer matrices  $T, D$  and  $S$ . All pairs of  $a_{1|i}(0)$  and  $b_{1|i}(0)$  are equal, because of current conservation at the end of the transmission line resonator, and we choose them to be  $a_{1|i}(0) = b_{1|i}(0) = \frac{1}{2}$  without loss of generality. This provides us with a set of orthogonal however not orthonormal spatial eigenfunctions. Therefore the spatial flux eigenfunctions  $f_{j|i}$  may be written,

$$f_{j|i}(x) = \frac{1}{2} \begin{pmatrix} 1 & 1 \end{pmatrix} T(x \bmod \Delta) (SD)^{(j-1)} \begin{pmatrix} 1 \\ 1 \end{pmatrix}.$$

Again we employ the algebraic properties of the pauli matrices to get the simplified expressions for the eigenmode functions,

$$f_{j|i}(x) = c_{j|i} \cos\left(\frac{\omega_i}{v}(x \bmod \Delta)\right) + s_{j|i} \sin\left(\frac{\omega_i}{v}(x \bmod \Delta)\right), \quad (6.9)$$

with,

$$c_{j|i} = \cos\left(\pi \frac{(j-1)n}{N+1}\right) - \frac{\sin\left(\pi \frac{(j-1)n}{N+1}\right)}{\sin\left(\pi \frac{n}{N+1}\right)} \left(\cos\left(\frac{\omega_{n,k}}{v}\Delta\right) - \cos\left(\pi \frac{n}{N+1}\right)\right)$$

$$s_{j|i} = -\frac{\sin\left(\pi \frac{(j-1)n}{N+1}\right)}{\sin\left(\pi \frac{n}{N+1}\right)} \sin\left(\frac{\omega_{n,k}}{v}\Delta\right),$$

where again the combined index  $i = \{n, k\}$  is supposed to index all eigenmodes across all manifolds.

Now that we found the eigenfrequencies and their respective spatial eigenfunctions, we may proceed twofold. In the first section we consider a coplanar waveguide resonator with only one Josephson junction. We evaluate its compatibility as a building block for a network of capacitively coupled nonlinear resonators. This approach should be considered as a evolutionary step from the interacting many body system using polaritons in the previous chapter. We adopt a different paradigm in the second section where we consider coplanar waveguides with multiple Josephson junctions. In the spirit of a Dicke model or Tavis-Cummings model we here present many-body physics in a single nonlinear resonator.

### 6.3. Single Josephson Junction

For a nonlinear resonator with a single Josephson junction all expressions for the general case found in the previous section are considerably simplified. The only transcendental equation for the spatial mode frequencies  $\omega_i$  reads,

$$\cot\left(\frac{\omega}{v}\Delta\right) = \frac{cv}{2C_J} \frac{\omega}{\omega_p^2 - \omega^2}, \quad (6.10)$$

With the help of this transcendental equation we numerically compute the frequencies for modes,  $\omega_i$ , of the nonlinear resonator which are antisymmetric with respect to a mirroring with a plane of symmetry perpendicular to the nonlinear resonator through the Josephson junction. For the symmetric modes the current through the Josephson junction vanishes and consequently the flux drop across the Josephson junction also vanishes and therefore the symmetric modes are unaltered by the presence of the Josephson junction.

One can check for the orthogonality of the antisymmetric modes by integrating the product of two different ( $i \neq l$ ) antisymmetric modes over the length of the nonlinear resonator,

$$\int_0^L f_i(x) f_l(x) dx = \frac{2v \left( \omega_l \cos\left(\frac{\omega_i}{v}\frac{L}{2}\right) \sin\left(\frac{\omega_l}{v}\frac{L}{2}\right) - \omega_i \cos\left(\frac{\omega_l}{v}\frac{L}{2}\right) \sin\left(\frac{\omega_i}{v}\frac{L}{2}\right) \right)}{\omega_l^2 - \omega_i^2}. \quad (6.11)$$



With the help of the transcendental equation for the eigenfrequencies 6.10 we get,

$$\frac{2v \left( \omega_l \cos\left(\frac{\omega_l L}{v}\right) \sin\left(\frac{\omega_l L}{2v}\right) - \omega_i \cos\left(\frac{\omega_l L}{v}\right) \sin\left(\frac{\omega_i L}{2v}\right) \right)}{\omega_l^2 - \omega_i^2} = -\frac{C_J}{c} \delta f_i \delta f_l,$$

where  $\delta f_i$  is the flux drop of every spatial eigenmode,  $\delta f_i = f_{1|i}(0) - f_{2|i}(0)$ . This result leads us to the useful generalization of the  $l_2$  scalar product to account for the discontinuity at the Josephson junction,

$$c \int_0^L f_i(x) f_l(x) dx + C_J \delta f_i \delta f_l = \delta_{i,l} \eta_i, \quad (6.12)$$

with the norm of the flux eigenfunctions,

$$\eta_i = c \left( \frac{L}{2} + \frac{\delta f_i^2}{\omega_i^2} \frac{c}{2L_J} \left( 1 + \frac{\omega_i^2}{\omega_p^2} \right) \right).$$

We decided not to normalize the spatial eigenmodes but rather regard them as modes with different effective “masses” or in this case capacitances  $\eta_i$ . This does not alter any physical observable value but simplifies some of the calculations. Now we can reformulate the flux field in terms of the eigenmode flux functions  $f_i$ ,

$$\phi(x, t) = \sum_{i=1}^{\infty} g_i(t) f_i(x),$$

and with the help of the orthogonality relation 6.12 we decompose the integral in the Lagrangian into a sum over the infinite number of eigenmode amplitudes  $g_i$ ,

$$\mathcal{L} = \sum_{i=1}^{\infty} \left( \frac{\eta_i}{2} \dot{g}_i^2 - \frac{1}{2} \eta_i \omega_i^2 g_i^2 \right) + \frac{\varphi_0^2}{L_J} \left( \cos\left(\frac{\delta\phi}{\varphi_0}\right) + \frac{1}{2} \left(\frac{\delta\phi}{\varphi_0}\right)^2 \right),$$

where  $\delta\phi = \sum_i g_i(t) \delta f_i$ . Here, we already neglected the symmetric modes, because they are completely decoupled from the antisymmetric modes. The corresponding Hamiltonian can be found by a Legendre transformation which leaves the nonlinear part from the Lagrangian unaltered,

$$\mathcal{H} = \sum_{i=1}^{\infty} \left( \frac{\pi_i^2}{2\eta_i} + \frac{1}{2} \eta_i \omega_i^2 g_i^2 \right) - \frac{\varphi_0^2}{L_J} \left( \cos\left(\frac{\delta\phi}{\varphi_0}\right) + \frac{1}{2} \left(\frac{\delta\phi}{\varphi_0}\right)^2 \right)$$

$$\pi_i = \eta_i \dot{\phi}_i.$$

We quantize the theory by promoting  $\pi_i$  and  $g_i$  to operators  $\hat{\pi}_i$  and  $\hat{g}_i$  with the canonical commutation relations  $[\hat{g}_i, \hat{\pi}_l] = i\hbar \delta_{i,l}$ . The generalized coordinates  $\hat{g}_i$  and momenta  $\hat{\pi}_i$  can be expressed in terms of lowering and raising operators  $a_i$  and  $a_i^\dagger$  via the relations,

$$\hat{\pi}_i = -i \sqrt{\frac{\hbar \eta_i \omega_i}{2}} (a_i - a_i^\dagger) \quad \hat{g}_i = \sqrt{\frac{\hbar}{2\eta_i \omega_i}} (a_i + a_i^\dagger),$$

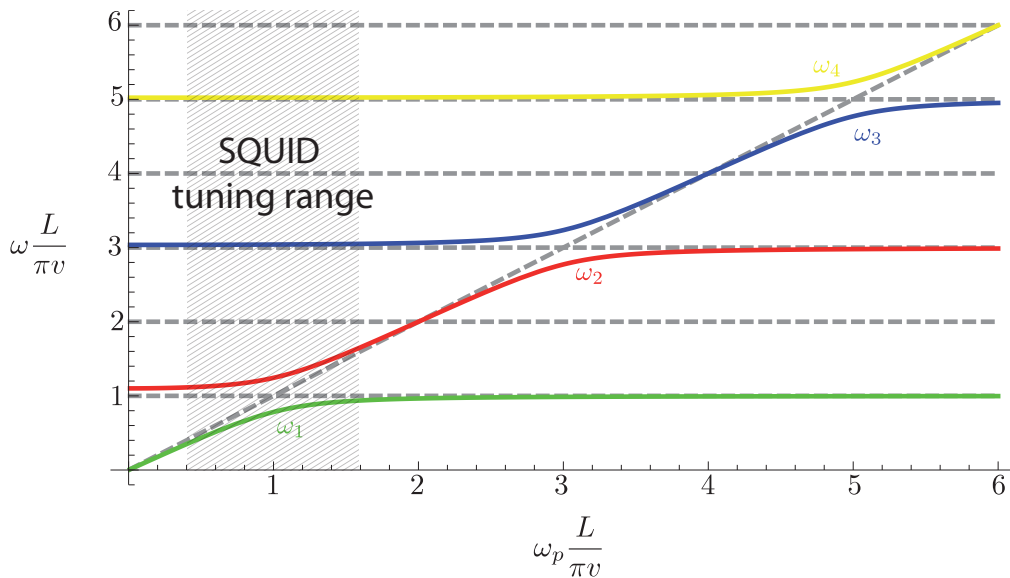


Figure 6.2.: Numerically calculated frequencies of the linear part of the coplanar waveguide resonator intersected by the capacitively shunted Josephson junction. Anti-crossings show up where the plasma frequency of the capacitively shunted Josephson junction  $\omega_p$  (dashed ascending graph) matches one of the frequencies of the antisymmetric modes of the coplanar waveguide resonator (dashed horizontal graphs). For parameters used in the numerical calculation see table 6.1

with  $[a_i, a_l^\dagger] = \delta_{i,l}$ . Finally, we arrive at the following Hamilton operator,

$$H = \sum_{i=1}^{\infty} \hbar \omega_i (a_i^\dagger a_i + \frac{1}{2}) - \frac{\varphi_0^2}{L_J} \left( \cos \left( \frac{\delta \hat{\phi}}{\varphi_0} \right) + \frac{1}{2} \left( \frac{\delta \hat{\phi}}{\varphi_0} \right)^2 \right), \quad (6.13)$$

with

$$\delta \hat{\phi} = \sum_{i=1}^{\infty} \lambda_i (a_i + a_i^\dagger) \quad \text{and,} \quad \lambda_i = \sqrt{\frac{\hbar}{2\eta_i \omega_i}} \delta f_i.$$

### 6.3.1. Spectrum

There are two limiting cases where the solutions of the transcendental equation for the eigenfrequencies 6.10 can be deduced directly without any numerical calculation. For our choice of parameters (c.f. table 6.1), the right hand side has a narrow divergence for  $\omega = \omega_p$  and quickly approaches zero for values of  $\omega$  unequal to  $\omega_p$ . Consequently, we have two different possibilities for approximate solutions of the transcendental equation. For  $\omega \neq \omega_p$  we can approximate the right hand side of the transcendental equation by 0 and find with the help of the left hand side,

$$\omega_i = (2i + 1) \frac{\pi v}{L} \quad i \in \mathbb{N}.$$

This corresponds to the situation where the plasma frequency of the Josephson junction  $\omega_p$  is off-resonant with the unperturbed frequency of the coplanar waveguide resonator mode and consequently we recover the unperturbed frequencies of the resonator without Josephson junction. The situation changes if one searches for modes near the plasma frequency of the Josephson Junction,  $\omega \approx \omega_p$ . Then, the right hand side diverges and the left hand side tells us that this always happens for frequencies equal to the frequencies of the symmetric modes  $\omega_i = ((\pi v)/L)2i$ . If we consider the linearized current flux relation for the capacitively shunted Josephson junction,

$$-\partial_x \phi_1\left(\frac{L}{2}\right) = -\partial_x \phi_2\left(\frac{L}{2}\right) = \frac{l}{L_J} \left(1 - \frac{\omega^2}{\omega_p^2}\right) \delta\phi,$$

we see that for modes with frequency  $\omega = \omega_p$  the current vanishes at the place of the Josephson junction. However the flux function of the eigenmode still has to be antisymmetric. The only possibility for the flux function of this eigenmode is to be the same as the symmetric mode with the half to the right of the Josephson junction flipped. Even though there is no current flowing into the Josephson junction, the flux drop at the Josephson junction is at its maximum. This tells us that current is flowing internally between the shunted capacitor and the inductive part of the Josephson junction to fulfill the Josephson current flux relation. This scheme is independent of the number of Josephson junctions: If the eigenmode of the entire nonlinear resonator oscillates at the plasma frequency of the identical Josephson junctions then the Josephson junctions introduce the maximal flux drop in the flux function of the nonlinear resonator and the current oscillates internally in the Josephson junctions. These considerations are confirmed by the numerically calculated mode spectrum of the linear part of the combined device. As expected, we in principle find the spectrum of the antisymmetric modes of the coplanar waveguide resonator and the plasma frequency of the Josephson junction, with additional avoided crossings near  $((\pi v)/L)(2i + 1) \approx \omega_p$ . The latter arise from their mutual interaction.

### 6.3.2. Derivation of the Kerr-nonlinearity

In principle, every antisymmetric mode is coupled to all other antisymmetric modes by the nonlinear part of the Hamilton operator 6.13. As we illustrate in the following, the interactions between different modes are however negligible in the low energy limit. Firstly, we note that the nonlinear part of the Hamilton operator does not contain any hopping terms of the form  $a_i a_l^\dagger + a_i^\dagger a_l$  for  $i \neq l$  because we already diagonalized the complete linear part of the Lagrangian. Secondly, density-density interactions of the type  $a_i^\dagger a_i a_l^\dagger a_l$  can be neglected because we assume all the modes but the mode under consideration to be in the vacuum state and the negligible interaction between the modes prevents them from becoming populated. Finally, the remaining higher order terms do not contribute a significant coupling. To separate the Hamilton operator of the considered mode from the rest, we apply a rotating wave approximation, the validity of which we confirm below. This approximation allows us to substantially simplify the cosine term of the nonlinear part of

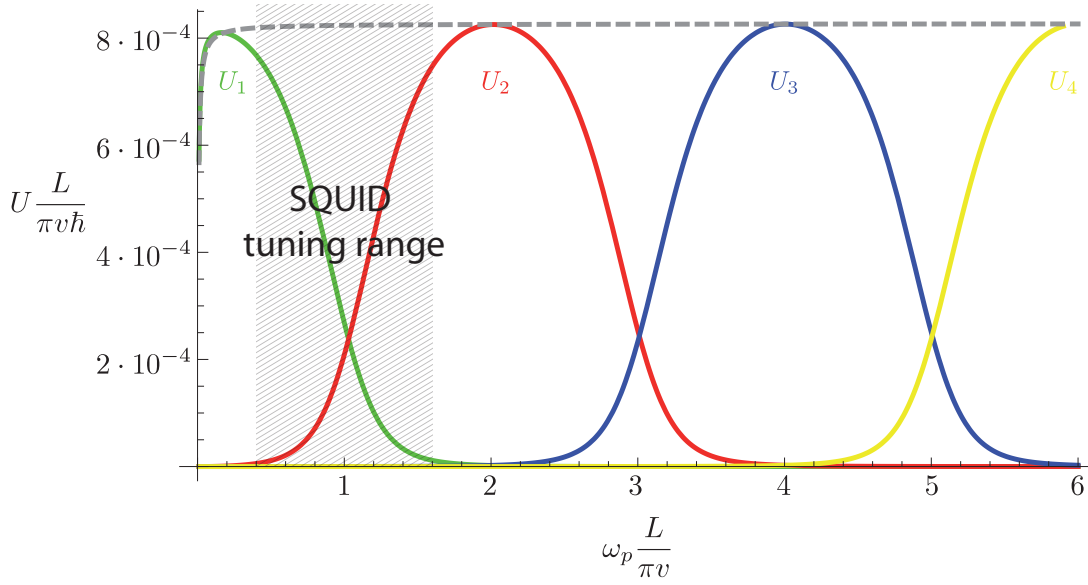


Figure 6.3.: Nonlinearity parameter of the different modes  $U_i$ . If the frequency of the mode is near the plasma frequency of the capacitively shunted Josephson junction the nonlinearity  $e^2/(4C_s)$  is inherited. For parameters used in the numerical calculation see table 6.1

the Hamilton operator. To this end we, consider the identity,

$$\begin{aligned} \cos \left( \sum_{i=1}^{\infty} \frac{\lambda_i}{\varphi_0} (a_i + a_i^\dagger) \right) &= \cos \left( \frac{\lambda_1}{\varphi_0} (a_1 + a_1^\dagger) \right) \cos \left( \sum_{i=2}^{\infty} \frac{\lambda_i}{\varphi_0} (a_i + a_i^\dagger) \right) \\ &\quad - \sin \left( \frac{\lambda_1}{\varphi_0} (a_1 + a_1^\dagger) \right) \sin \left( \sum_{i=2}^{\infty} \frac{\lambda_i}{\varphi_0} (a_i + a_i^\dagger) \right). \end{aligned}$$

The sine terms will only contain operator products with odd powers of the individual mode operators, hence the second addend can be neglected as part of the rotating wave approximation. If we iterate this consideration, we can approximate the cosine of the sum of our mode position operators by the product of the cosines of the mode position operators,

$$\cos \left( \sum_i \frac{\lambda_i}{\varphi_0} (a_i + a_i^\dagger) \right) \rightarrow \prod_i \cos \left( \frac{\lambda_i}{\varphi_0} (a_i + a_i^\dagger) \right).$$

The cosine terms can further be approximated by a sum of normally ordered operator products with equal numbers of annihilation and creation operators,

$$\cos \left( \frac{\lambda_i}{\varphi_0} (a_i + a_i^\dagger) \right) \rightarrow \alpha_{i,0} + \alpha_{i,1} a_i^\dagger a_i + \alpha_{i,2} a_i^\dagger a_i^\dagger a_i a_i + \dots \quad (6.14)$$

The expansion coefficients  $\alpha_{i,k}$  in equation 6.14 are not the usual expansion coefficients of the cosine since one has to take into account that also higher powers of  $\lambda_i/\varphi_0(a_i +$

$a_i^\dagger$ ) generate operator products of lower powers if we attempt to normal order the mode operator binomials. With the formula for mode operator binomials given in [64],

$$(a + a^\dagger)^m = \sum_{k=0}^{\lfloor m/2 \rfloor} \sum_{n=0}^{m-2k} \frac{m!(a^\dagger)^i a^{m-2k-n}}{2^k k! n! (m-2k-n)!},$$

where  $\lfloor m/2 \rfloor$  denotes the largest integer less than or equal to  $m/2$ , we can identify the prefactors for the rotating wave expansion of the cosine,

$$\cos\left(\frac{\lambda_i}{\varphi_0}(a_i + a_i^\dagger)\right) \rightarrow e^{-\frac{\lambda_i^2}{2\varphi_0^2}} \left(1 - \frac{\lambda_i^2}{\varphi_0^2} a_i^\dagger a_i + \frac{\lambda_i^4}{4\varphi_0^4} a_i^\dagger a_i^\dagger a_i a_i + \dots\right).$$

We assume exemplarily that only the fundamental mode is populated and can therefore neglect all modes with  $i \neq 1$  in the Hamilton operator. Since  $|\lambda_i/\varphi_0| \ll 1$ , as will be confirmed below, and because we are only interested in low photon numbers where  $\lambda_i^2/\varphi_0^2 \langle a_1^\dagger a_1 \rangle \ll 1$ , we can truncate the cosine expansion after the quartic order term. We thus get for the nonlinear part of our Hamilton operator in the rotating wave and low photon number approximation,

$$H^{\text{nonlin}} \rightarrow -\frac{\varphi_0^2}{L_J} \left( \left(1 - \frac{\lambda_1^2}{\varphi_0^2} a_1^\dagger a_1 + \frac{\lambda_1^4}{4\varphi_0^4} a_1^\dagger a_1^\dagger a_1 a_1\right) \prod_{i=1}^{\infty} e^{-\frac{\lambda_i^2}{2\varphi_0^2}} + \frac{\lambda_1^2}{\varphi_0^2} a_1^\dagger a_1 \right).$$

Any constant in the Hamilton operator provides us with a not measurable shift of the overall energy, therefore we may omit all constant terms and get the following Hamilton operator for the fundamental mode in rotating wave approximation,

$$H_1 = (\omega_1 - \delta\omega) a_1^\dagger a_1 - U a_1^\dagger a_1^\dagger a_1 a_1,$$

with

$$\delta\omega = \frac{\lambda_1^2}{L_J} \left(1 - \prod_{i=1}^{\infty} e^{-\frac{\lambda_i^2}{2\varphi_0^2}}\right) \quad U = \frac{\lambda_1^4}{4L_J\varphi_0^2} \prod_{i=1}^{\infty} e^{-\frac{\lambda_i^2}{2\varphi_0^2}},$$

where  $\delta\omega$  is a small renormalization of the fundamental mode due to the nonlinearity.

To calculate the nonlinearity parameter for the fundamental mode,  $U_1$ , we need to evaluate the formally infinite product,  $\prod_i \exp(-\lambda_i^2/(2\varphi_0^2))$ . Here the superconducting gap provides a natural cut-off frequency. If the first excited state of a mode of the nonlinear resonator exceeds the superconducting gap in energy, Cooper pairs will break and strong dissipation processes will start. Therefore we only include modes that fit energetically into the superconducting gap in the above product and get  $\prod_{i=1}^{i_{\text{cutoff}}} \exp(-\lambda_i^2/(2\varphi_0^2))$ .  $i_{\text{cutoff}}$  is here the largest of all  $i$  that fulfills the equality,

$$\hbar \frac{\pi\nu}{L} (2i-1) < \Delta_{\text{sc}}(T) \quad \text{and} \quad \Delta_{\text{sc}}(T) = 3.52 k_B T_c \sqrt{1 - \frac{T}{T_c}},$$

with  $\Delta_{\text{sc}}$  the energy gap of the superconductor. For our calculations we used the critical temperature of niobium. Niobium technique is favorable because of its high transition

temperature of 9.2 Kelvin that enables fast precharacterization at liquid helium temperatures before cooling the whole device down to the millikelvin range.

The nonlinearity of the eigenmodes is inherited from the Josephson junction when the frequency of the eigenmode is near the plasma frequency  $\omega_p$ . The unnormalized nonlinearity parameter of a single Josephson junction is simply half of its charging energy  $\tilde{U} = E_c/2 = e^2/(4C_J)$ . The normalization coming from the normal ordering of all orders of the cosine in the Hamilton operator ensures that for increasing Josephson inductance the nonlinearity parameter vanishes. The charge qubit in the transmon regime has exactly the same nonlinearity since after all it is merely a capacitively shunted Josephson junction. Careful inspection of the unnormalized nonlinearity parameter of individual eigenmodes of the nonlinear resonator provides us with the following formula,

$$\lim_{\omega \rightarrow \omega_p} \tilde{U}_i = \lim_{\omega \rightarrow \omega_p} \frac{\lambda_i^4}{4L_J \varphi_0^2} = \frac{e^2}{4 \frac{(C_J + \frac{Lc}{8})^2}{C_J}}.$$

Therefore the eigenmode of the nonlinear resonator can not inherit the full nonlinearity of the bare Josephson junction but the nonlinearity of the Josephson junction gets renormalized by virtue of the altered Josephson junction capacitance. This principle of inheritance, where a collective mode of the composite resonator-junction system adopts the properties of one of its constituents if its frequency matches the frequency of the respective isolated constituent, is further illustrated by the nonlinearity  $U_i$  of higher modes (see 6.3). Here we can see that also higher modes could be employed as onsite nonlinear mode as they acquire the same amount of nonlinearity.

### 6.3.3. Experimental limitations and prerequisites

In this section we discuss how one would realize the above introduced nonlinear resonator with one Josephson junction. We propose to use a dc SQUID instead of the single Josephson junction in order to have a tunable nonlinearity  $U$ . The SQUID consists of two identical Josephson junctions with plasma frequency  $\omega_{p,0}$  in a loop that is threaded by an external flux  $\Phi$ . If the self inductance of the SQUID is negligible, it can be modeled as a single Josephson junction whose plasma frequency  $\omega_p$ ,

$$\omega_p = \omega_{p,0} \sqrt{2|\cos(\Phi/(2\varphi_0))|}$$

can be tuned via the external flux  $\Phi$  threading the SQUID loop (cf. [16]). The further discussion will be twofold. We first consider the experimental limitations which are imposed on our theoretical model by the physics of the superconducting circuitry and then discuss how the setup should be tuned to realize a sufficient amount of nonlinearity. In an experiment, it is favorable that the fundamental mode of the nonlinear resonator is within a frequency band suitable for state-of-the-art microwave measuring devices. Furthermore, the thermal population should be insignificant at least at millikelvin temperatures. We therefore choose the length  $L$  of the transmission line resonator such that for all relevant plasma frequencies  $\omega_p$  the frequency of the fundamental mode is in the range  $4\text{GHz} < \omega/(2\pi) < 8\text{GHz}$ . All other design parameters of the transmission line ( $Z_0, l, c$ ) are typical values found in many circuit QED setups. We study a wide range

Resonator	Josephson Junction		
Wave Impedance	$Z_0 = 50\Omega$	Shunting Capacitance	$C_J = 1.9\text{pF}$
Phase Velocity	$v = 0.98 \cdot 10^8 \frac{\text{m}}{\text{s}}$	plasma frequency	$0.2 \frac{\pi v}{L} < \omega_p < 1.3 \frac{\pi v}{L}$

Table 6.1.: Parameters for an experimental realization of the coplanar waveguide resonator with a single Josephson junction.

of plasma frequencies, putting a focus on the experimentally well accessible range of  $0.2((\pi v)/L) < \omega_p < 1.3((\pi v)/L)$ . A summary of all relevant parameters is given in 6.1.

In figures 6.2,6.3 and 6.5 we hatch a proposed tuning range for the dc-SQUID plasma frequency of  $0.2((\pi v)/L) < \omega_p < 1.3((\pi v)/L)$ . This results in a tuning range for the non-linearity  $U_1$  of  $U_{min}/(2\pi\hbar) = 10\text{kHz}$  to  $U_{max}/(2\pi\hbar) = 10\text{MHz}$  and a frequency drag for the fundamental mode of  $\omega_{min}/(2\pi) = 5.2\text{GHz}$  to  $\omega_{max}/(2\pi) = 8.5\text{GHz}$ . This provides us with sufficient nonlinearity to exceed present day decay rates of coplanar waveguide resonators  $\gamma/(2\pi) \approx 100\text{kHz}$  while still keeping the frequency drag within the bandwidth of state of the art microwave detection. These values allow one to investigate the Bose-Hubbard Hamiltonian in the driven dissipative regime [14, 78, 59, 83] with seamless tunability between the onsite nonlinearity dominated regime  $U > J$  and the hopping dominated regime  $J > U$  using present day technology. Finally, we note that the nonlinearity  $U_{max}$  is here bound from above by the charging energy (see figure 6.3). Therefore, it could be further increased by decreasing the Josephson junction capacitance  $C_J$ . However, this would shift the anticrossing marking the region of tunability, and hence the operating interval, to lower plasma frequencies, finally resulting in fabrication and noise issues. In the whole presented range of plasma frequencies  $0.2((\pi v)/L) < \omega_p < 1.3((\pi v)/L)$  we checked the validity of our rotating wave approximation. The most dominant process of all neglected ones is the exchange of three fundamental mode excitations with one excitation of the next higher odd mode,  $a_1 a_1 a_1 a_2^\dagger$ . The prefactor for this term in the Hamilton operator is of the order,  $\lambda_1^3 \lambda_2 / (L_J \varphi_0^2)$ . This should be compared to the frequency difference between three times the fundamental mode frequency  $\omega_1$  and the second odd mode frequency  $\omega_2$ . For the whole considered range of critical currents the quotient of the prefactor and the frequency difference is vanishingly small, which validates our assumption of decoupled field modes.

### 6.3.4. Networks

Circuit QED offers ample possibilities to couple several resonators to a network as there are basically no limitations on the topology and geometry of networks of transmission line resonators [47], except for constraints imposed by the detection circuitry and by space on the chip. In figure 6.4 we display two specific configurations of one-dimensional networks (chains) of nonlinear resonators. In figure 6.4 a), the resonators are coupled at both ends, which form a small capacitance and thereby enable photon hopping between adjacent resonators. In this way, also two-dimensional lattices can be formed by coupling more than two resonators at their ends. The advantage of this way of coupling the res-

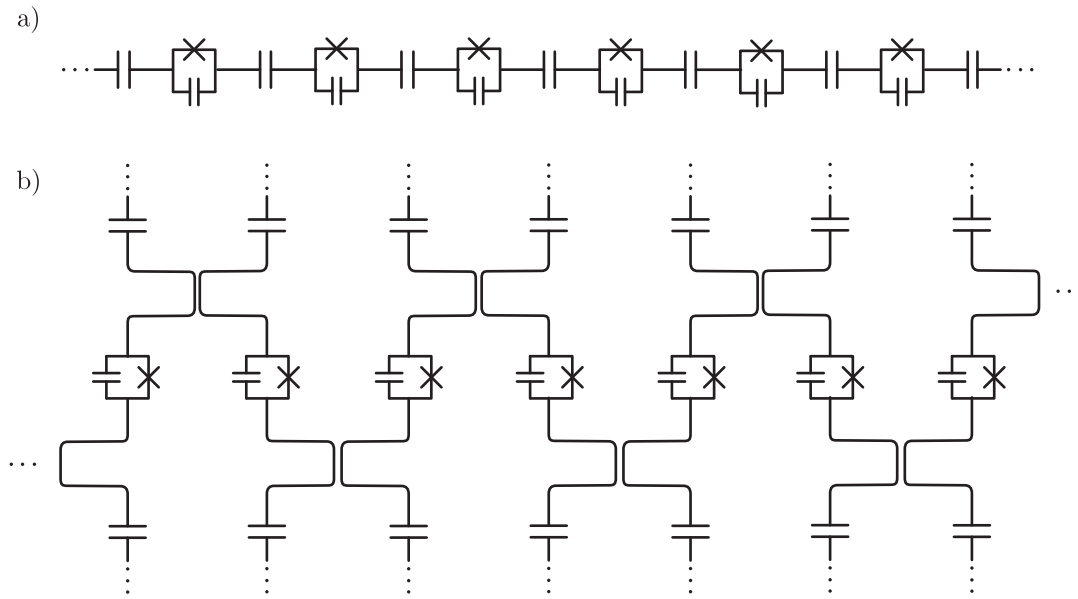


Figure 6.4.: Two different coupling schemes for one-dimensional networks of nonlinear resonators. a) Capacitive coupling of the nonlinear resonators. b) Capacitive and inductive coupling with the advantage of individual addressability for the nonlinear resonators. Only the central wires of the coplanar waveguides are drawn. Groundplanes are omitted.

onators is scalability, but one can only probe the output fields at the borders of the entire network. Coplanar waveguide resonators can however also be coupled by reducing the distance between their central lines for a certain length see figure 6.4 b). Depending on the exact position of the convergence, and the specific mode under consideration, the coupling between the two resonators is in general both capacitive and inductive [60, 76]. The advantage of this coupling scheme is that each nonlinear resonator can be probed individually. This advantage however only holds for one-dimensional networks.

For both designs the coupling constants are typically smaller than the frequencies of the field modes and therefore a rotating wave approximation is applicable. The coupling Hamilton operator consequently reads [69],

$$H_g = \sum_{\langle l,m \rangle} g_{l,m} (a_l a_m^\dagger + a_l^\dagger a_m) ,$$

where  $a_l$  is one but always the same eigenmode operator of the different nonlinear resonators, the sum comprises all coupled nonlinear resonators and  $g_{l,m}$  incorporates all microscopic details of the interaction like the respective eigenmode, the coupling capacitance and the coupling inductance. With present day precision in sample production we assume, for the following, all coupling constants to be equal,  $g_{l,m} = g$ . As shown before every nonlinear resonator can be modeled by a harmonic oscillator Hamilton operator with a Kerr nonlinearity of strength  $U$ . For the whole chain of nonlinear resonators we therefore get a



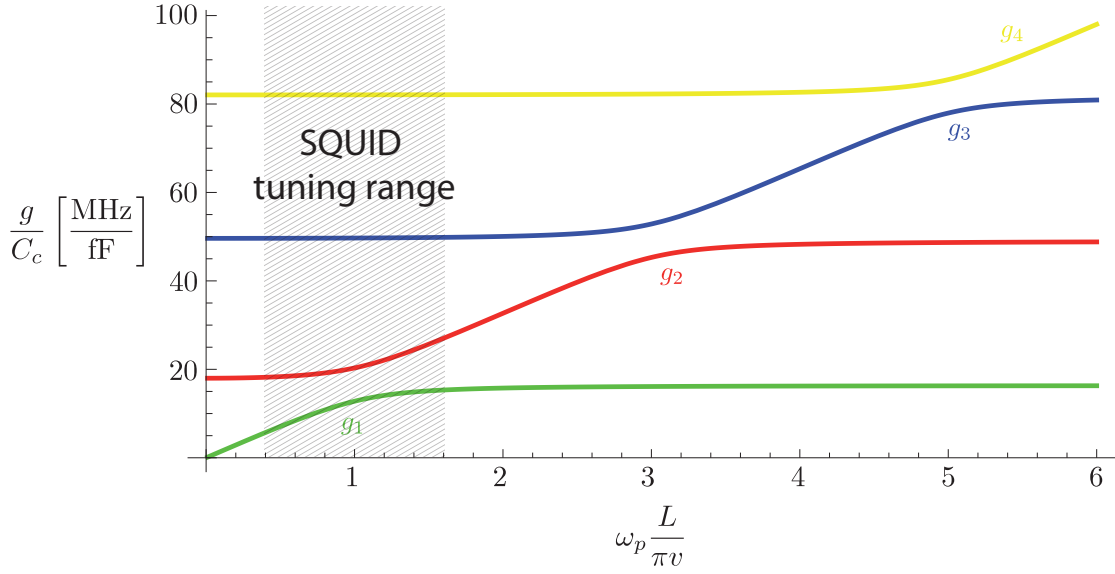


Figure 6.5.: Numerically calculated coupling strengths between the same modes of adjacent nonlinear resonators in a capacitively coupled network. For parameters used in the numerical calculation see table 6.1

Bose-Hubbard Hamilton operator of the form,

$$H_{BH} = \sum_l \left[ \omega a_l^\dagger a_l + U a_l^\dagger a_l^\dagger a_l a_l + g (a_l^\dagger a_{l+1} + a_l a_{l+1}^\dagger) \right] \quad (6.15)$$

Next we calculate the strength of the coupling  $g$  between two neighboring nonlinear resonators in a network. We only consider capacitive coupling of nonlinear resonators where the respective ends of the central lines of adjacent nonlinear resonators are either close to each other or connected by interdigitated capacitors. To integrate the coupling into our theoretical model we have to include the energy of the coupling capacitor, with coupling capacitance  $C_c$ , into the Lagrangian of the nonlinear resonator,

$$\mathcal{L}_c = \frac{C_c}{2} (\dot{\phi}_1|_{x=L} - \dot{\phi}_2|_{x=0})^2, \quad (6.16)$$

where  $\phi_{1/2}$  is the flux field of adjacent nonlinear transmission line resonators. After a Legendre transformation to get the corresponding energy term in the Hamiltonian we would get different conjugate momenta  $\pi_n$ . We neglect this effect because the coupling capacitance  $C_c$  is very small compared to the overall capacitance of the nonlinear resonator. After quantizing the theory the time derivative of the flux field of the nonlinear resonator gets mapped to  $\dot{\phi}_{1/2} \rightarrow -i \sum_i \sqrt{\hbar \omega_i / (2\eta_i)} f_n(x) (a_{1/2,i} - a_{1/2,i}^\dagger)$ . The coupling term in the Lagrangian therefore provides us with many different effects: We get renormalizations of the different resonator eigenmode frequencies, exchange couplings between different eigenmodes of adjacent resonators and on the same resonator, which we neglect in a rotating

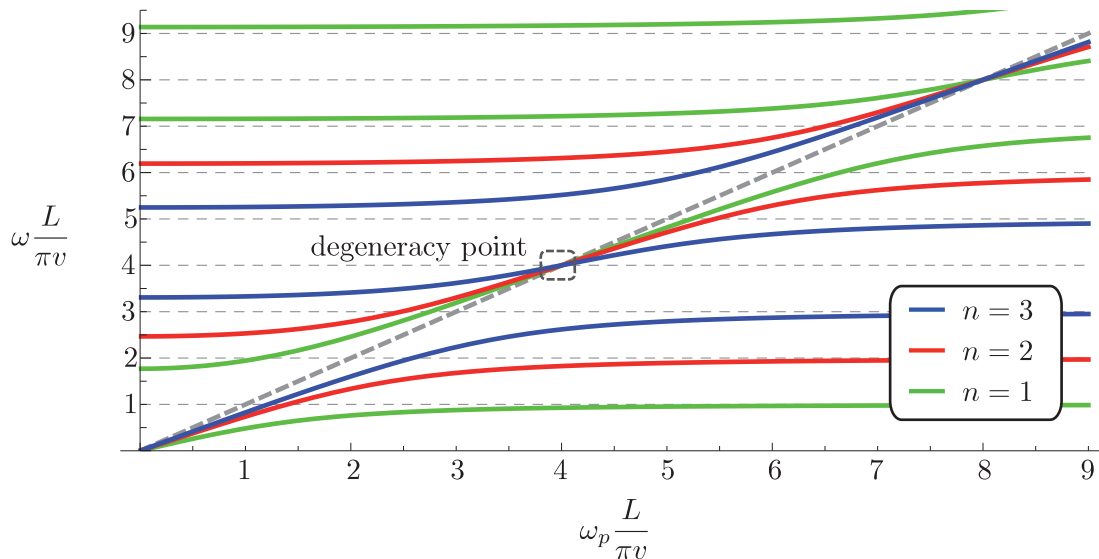


Figure 6.6.: Spectrum of a coplanar waveguide resonator interrupted by 3 identical and uniformly distributed Josephson junctions plotted over their plasma-frequency  $\omega_p$  in units of the fundamental mode frequency  $(\pi v)/L$ . Eigenmodes of the coplanar waveguide resonator without Josephson junctions that do not couple to the Josephson junctions for symmetry reasons are omitted in the plot. The degeneracy point that we consider in Figure 6.9 and in our calculations for the driven dissipative regime below is marked by a dashed box.

wave approximation, and exchange coupling of the same mode of adjacent resonators,

$$H_{i,g} = -\frac{C_c \omega_i}{4 \eta_i} \sum_{\langle l,m \rangle} (a_{l,i}^\dagger a_{m,i} + a_{l,i} a_{m,i}^\dagger). \quad (6.17)$$

The dimensionless capacitance of the fundamental eigenmodes  $\eta_i$  of the nonlinear transmission line resonator is not affected by a change of the Josephson junction's plasma frequency for generic parameters (cf. 6.1) of our setup. The coupling  $g_i = (C_c \omega_i)/(4\eta_i)$  of the same eigenmodes in adjacent nonlinear resonators is therefore almost completely determined by the frequency of the modes cf. figure 6.5, where we plotted the coupling of the first three antisymmetric eigenmodes of the nonlinear resonator. This in turn enables us to increase the nonlinearity while increasing the coupling, provided we do not use the fundamental mode of the nonlinear resonator.

## 6.4. Multiple Josephson Junctions

### 6.4.1. Spectrum

The nonlinear resonator examined in the previous section can be considered as a building block or one "site" in a complex network. This building block is the single ingredient to

build the network. The network supports excitations that can hop between different building blocks and interact if they are on the same building block. In the flexible framework of circuit QED we can also explore many body physics in a single coplanar waveguide resonator. This situation has already been considered for example by Dicke [21] in his seminal work on multiple two level scatterers coupled to a single photonic mode confined by a cavity. If we consider more than one Josephson junction in our coplanar waveguide resonator we also enter this realm of multiple scatterers coupled to the field of a single cavity. However the extraordinary high coupling strengths of circuit QED force us to walk off the beaten path of the phenomenological Dicke model and delve into the microscopical model already solved for its eigenmodes in section 6.1.

To calculate the spectrum of a coplanar waveguide resonator with  $N$  Josephson junctions we have to solve  $N$  transcendental equations 6.8. The computational effort therefore only scales linearly with the system size and we are able to handle quite large systems. In figure 6.6 we plotted the spectrum of a coplanar waveguide resonator with three junctions. The Josephson junctions are spaced evenly, with distance  $\Delta$ , along the length of the coplanar waveguide resonator. Because of this symmetry the spectrum decomposes into sub-spectra. There are as many sub-spectra as there are Josephson junctions. Each sub-spectrum represents the manifold of eigenmodes which are solutions to one of the transcendental equations 6.8. The sub spectrum for each manifold resembles the spectrum of a Josephson junction that is ultrastrongly coupled to specific free modes of the bare coplanar waveguide resonator (c.f. citation [52] or section 6.3). However these sub-spectra can not be attributed to the coupling between a specific Josephson junction and the coplanar waveguide resonator but rather the coupling of a collective Josephson junction mode with specific symmetry to modes of the coplanar waveguide resonator with compatible symmetry. For a large detuning between free mode frequency and plasma frequency the Josephson junction mode and the coplanar waveguide resonator oscillate independently. In turn for degenerate plasma and free mode frequencies, the eigenfrequencies of the combined device show an anticrossing of the order of the eigenmode frequencies themselves. In this regime excitations of the device are strongly hybridized between the coplanar waveguide resonator and the Josephson junctions. We can deduce the positions of the anti-crossings with the help of flux eigenfunctions  $f_i$ . Consider a free mode of the bare coplanar waveguide resonator which has the frequency  $\omega_{n'} = (\pi v/L)n'$  and exhibits an anticrossing with the Josephson junction mode which is associated to the manifold  $n$  of eigenmodes. This mode asymptotically approximates one of the manifold modes for very large plasma frequency of the Josephson junctions  $\omega_p \rightarrow \infty$ . In this situation we may conclude that the free mode frequency plugged into the flux function of the approximated manifold eigenmode should reduce the flux eigenfunction to that of the free mode. With this reasoning we can deduce the following rules,

$$n' = n + 2(N + 1)m \qquad n' = -n + 2(N + 1)(m + 1). \qquad (6.18)$$

If either of these both rules is fulfilled, then the free mode of frequency  $\omega_{n'}$  shows an anti-crossing with the modes of manifold  $n$ . Additionally to all eigenmodes derived from the transcendental equations 6.8 there are modes that do have extrema of their flux function at the position of the Josephson junctions. The current in the coplanar waveguide is proportional to the spatial derivative of the flux function. Therefore these modes have vanishing current at the Josephson junctions and are consequentially completely decoupled.

**Connections to Phenomenological Model** As it turned out it is possible to treat the interaction between the Josephson junctions and the coplanar waveguide resonator exactly in the microscopic model and we will introduce the small nonlinearity of the Josephson junctions perturbatively in the following. An alternative approach would have been to diagonalize the coplanar waveguide resonator and the Josephson junctions separately and then treat the interaction between them in a perturbative manner. The resulting Hamilton operator should contain interaction energy contributions similar to,  $g(a^\dagger + a)(b + b^\dagger)$ , where  $a$  lowers the eigenstate of the coplanar waveguide resonator and  $b$  lowers the eigenstate of the Josephson junctions. The magnitude of the coupling coefficient  $g$  can already be determined by the size of the anticrossing in the exact classical spectrum of eigenmodes. The effective coupling frequency between the Josephson junctions and the coplanar waveguide resonator, is half of the frequency difference of the eigenmodes of the nonlinear resonator at the anticrossing. We restrict ourselves to the lowest anticrossing in each sub spectrum and Taylor expand the transcendental equations (6.8) to second order in  $\omega = \omega_p + \delta\omega$  around the anticrossing at  $\omega_p = (\pi v/L)n$ , and get

$$\delta\omega^2 = \frac{(N+1)}{4C_J L l} \Rightarrow g = \frac{1}{2} \sqrt{\frac{N+1}{C_J L l}}.$$

This expression can be given a simple physical meaning when we realize that the coupling of two resonant oscillatory circuits where one is coupled to the current of the other (c.f. figure 6.7) has the same functional form. The coupling strength is proportional to the frequency of a fictional resonating circuit with the inductance of the one circuit and the capacitance of the other. We also corroborated the approximate coupling formula with numerical calculations presented in figure 6.7 b). The coupling strength  $g$  grows with the square root of the number of Josephson junctions comparable to the Situation in the Dicke model. The Dicke model describes a bosonic mode coupled uniformly to many two level systems. After the Holstein Primakoff transformation of the two level systems we get, in the thermodynamic limit, a mapping on the Hamiltonian of two coupled harmonic oscillators. The two harmonic oscillators are the bosonic mode and spin waves for the two level systems, and the coupling between them is proportional to the square root of the number of two level systems. This similarity immediately raises the question whether a ground state phase transition comparable to the one seen in the Dicke model can also happen here. In the Dicke model the phase transition is indicated by the appearance of a soft mode, a joined excitation of the bosonic mode and the two level systems with vanishing frequency even though the frequencies of all involved systems does not vanish. We can exclude this possibility for our system. The left hand side of equation (6.7) diverges for  $\omega = 0$  while the right hand side vanishes, if  $\omega_p$  is finite. The energy gap between the energetically lowest eigenmode and the groundstate for degenerate Josephson junctions and coplanar waveguide resonator only slowly converges to 0 upon increasing the number of Josephson junction evidenced by the numerical data shown in figure 6.7 c). The lowest energy eigenmode therefore never crosses the groundstate like it does in the Dicke model.

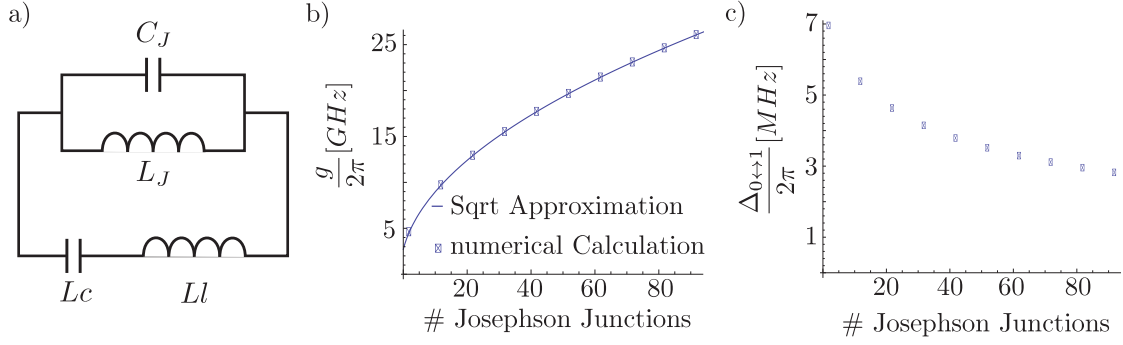


Figure 6.7.: a) Minimal model for the coupling of a coplanar waveguide resonator of length  $L$  with total capacitance  $Lc$  and inductance  $Ll$  and the Josephson junction with Josephson inductance  $L_J$  and parallel capacitance  $C_J$ . b) Comparison of numerical data and analytical approximation of the phenomenological coupling strength between coplanar waveguide resonator and Josephson junction. c) Numerical data for the gap between the energetically lowest eigenmode and the groundstate. All numerical data in this figure is calculated with the parameters presented in subsection 6.4.5

### 6.4.2. Quantisation

After the determination of the flux eigenfunctions  $f_i$  and eigenfrequencies  $\omega_i$  we are now able to decompose the Lagrangian of a flux field  $\phi = \sum_i g_i f_i$  into an infinite but discrete set of eigenmodes with the help of the following generalized scalar product for the eigenfunctions  $f_i$ ,

$$c \int_0^L f_k f_l dx + C_J \sum_{j=1}^N \delta f_{j|k} \delta f_{j|l} = \delta_{k,l} \eta_k,$$

where,

$$\delta f_{j|i} = f_i|_{x \nearrow j\Delta} - f_i|_{x \searrow j\Delta} = 2 \sin\left(\pi \frac{jn}{N+1}\right) \frac{(\cos(\frac{\omega_i}{v}\Delta) - \cos(\pi \frac{n}{N+1}))}{\sin(\pi \frac{n}{N+1})},$$

is the flux drop of the individual eigenmode  $i$  at Josephson junction  $j$ . With this scalar product the eigenmodes are orthogonal but not normalized. The norm of the eigenmodes reads,

$$\eta_i = \frac{Lc}{2} \frac{1 - \cos(k_i\Delta) \cos(\pi \frac{n}{N+1})}{\sin(\pi \frac{n}{N+1})^2} + \frac{c(N+1)}{4C_J l} \left( \frac{\sin(k_i\Delta)}{\sin(\pi \frac{n}{N+1})} \right)^2 \frac{\omega_p^2 + \omega^2}{(\omega_p^2 - \omega^2)^2}.$$

The linearized Lagrangian in terms of the time dependent amplitudes  $g_i$  is a sum of independent harmonic oscillators,

$$\bar{\mathcal{L}} = \sum_i \frac{\eta_i}{2} \dot{g}_i^2 - \frac{1}{2} \eta_i \omega_i^2 g_i^2.$$

The norm of the eigenmodes has units of a capacitance and represents the fictional capacitance of the LC-circuit that in turn represents a specific eigenmode of the nonlinear resonator. However the magnitude of the norm of the eigenmodes is without physical relevance since it depends on the arbitrary chosen norm for the spatial eigenfunctions. Of physical relevance for the modes are the frequency  $\omega_i$  and the local values for the electrical potential  $V(x) = g f(x)$  and current  $I(x) = \frac{1}{l} g \frac{d}{dx} f(x)$  of the central line in the coplanar waveguide resonator which are independent of the chosen normalization. With this we can perform a Legendre transform to get the Hamiltonian of the system,

$$\bar{\mathcal{H}} = \sum_i \frac{1}{2\eta_i} \pi_i^2 + \frac{1}{2} \eta_i \omega_i^2 g_i^2, \quad (6.19)$$

with  $\pi_i = \eta_i \dot{g}_i$  the canonical conjugate momentum of  $g_i$ . Afterwards we quantize the theory in the generic way by introducing individual lowering and raising operators for the individual eigenmodes of the nonlinear coplanar waveguide resonator,

$$\hat{\pi}_i = -i \sqrt{\frac{\hbar \eta_i \omega_i}{2}} (a_i - a_i^\dagger) \quad \hat{g}_i = \sqrt{\frac{\hbar}{2\eta_i \omega_i}} (a_i + a_i^\dagger).$$

The Hamilton operator, together with the nonlinear contributions originating from the Josephson junctions, consequently reads,

$$H = \bar{H} + H_{NL} = \sum_i \hbar \omega_i a_i^\dagger a_i - \frac{\varphi_0^2}{L_J} \sum_{j=1}^N \left( \cos\left(\frac{\delta \hat{\phi}_j}{\varphi_0}\right) + \frac{1}{2} \left(\frac{\delta \hat{\phi}_j}{\varphi_0}\right)^2 \right),$$

where,

$$\begin{aligned} \delta \hat{\phi}_j &= \sum_i \delta f_{j|i} \hat{g}_i \\ &= \sum_i \sqrt{\frac{2}{N+1}} \sin\left(\pi \frac{j n_i}{N+1}\right) \lambda(\omega_i) (a_i + a_i^\dagger), \end{aligned}$$

and  $\lambda(\omega_i)$  is,

$$\lambda(\omega_i) = \frac{\sqrt{N+1} \sqrt{\hbar \omega_i}}{C_J L \sqrt{\left(\frac{2l}{L}(\omega_p^2 - \omega_i^2)\right)^2 + \left(\cot\left(\frac{\omega_i \Delta}{v}\right) \frac{\omega_i}{L C_J v} (\omega_p^2 - \omega_i^2) + \frac{N+1}{C_J L^2} (\omega_p^2 + \omega_i^2)\right)},$$

which is a measure of the mean zero point flux fluctuations in the Josephson junctions. If the frequency of the eigenmode is close to a free mode frequency  $\omega_{n'} = ((\pi v)/L)n'$  of the coplanar waveguide resonator, then the flux fluctuations in the Josephson junctions vanish because the flux drops of the spatial eigenfunctions  $\delta f_{j|i}$  vanish. However if the eigenmode frequency is equal to the plasma frequency  $\omega_p$ , the flux fluctuations are,

$$\lambda_p(n) = \sqrt{\frac{\hbar}{2\omega_p \left( C_J + \frac{Lc}{4(N+1)} \frac{1}{1 \pm \cos\left(n \frac{\pi}{N+1}\right)} \right)},$$

which is the zero point flux fluctuation of a single Josephson junction with renormalized capacitance  $C'_J = C_J + \frac{Lc}{4(N+1)} \frac{1}{1 \pm \cos(\frac{\pi}{N+1})}$ . Note that naively taking  $\lim_{\omega_p \rightarrow \bar{\omega}} \lambda(\omega_n) = \lambda(\omega_p)$  does not lead to correct results since  $\cot(\frac{\omega}{v}\Delta)$  diverges for  $\omega_p \rightarrow \bar{\omega}$ . We thus expressed  $\cot(\frac{\omega}{v}\Delta)(\omega_p^2 - \omega^2)$  with the help of the transcendental equation for the eigenfrequencies (c.f. equation 6.8) to get the correct limit.

**Effects of the Nonlinearity** The nonlinearity reintroduces couplings between the above derived eigenmodes that do not couple linearly since we diagonalized the linear part of the Lagrangian. If we would consider a infinite coplanar waveguide with Josephson junctions the nonlinearity would introduce scattering of excitations with conservation of the crystal quasi-momentum which leads to a selection rule for allowed scattering between the eigenmodes. Our setup with the periodically spaced Josephson junction and the finite coplanar waveguide resonator still contains enough symmetry to generate a selection rule for allowed scattering between eigenmodes. The nonlinearity of the nonlinear resonator is the sum of the Josephson energies of all phase-jumps at the Josephson junctions, where quadratic terms have been subtracted. As a first step to further analyze the workings of the nonlinearity we expand the polynomial of all manifold flux quadratures  $\bar{\phi}_n = \sum_k \hat{\phi}_{n,k} = \sum_k \lambda(\omega_{n,k})(a_{n,k} + a_{n,k}^\dagger)$ ,

$$\begin{aligned} H_{NL} &= -\frac{\varphi_0^2}{LJ} \sum_{j=1}^N \sum_{l=2}^{\infty} \frac{-2^l}{(2l)!(N+1)^l} \left( \sum_{n=1}^N \sin\left(\pi \frac{jn}{N+1}\right) \frac{\bar{\phi}_n}{\varphi_0} \right)^{2l} \\ &= -\frac{\varphi_0^2}{LJ} \sum_{j=1}^N \sum_{l=2}^{\infty} \frac{-2^l}{(2l)!(N+1)^l} \sum_{\bar{n} \in P(2l)} \prod_{m=1}^{2l} \sin\left(\pi \frac{j\bar{n}_m}{N+1}\right) \frac{\bar{\phi}_{\bar{n}_m}}{\varphi_0}. \end{aligned} \quad (6.20)$$

Here  $\bar{n}$  denotes a vector of length  $2l$  that is an element of the set  $P(2l)$  of all combinations of manifold indices  $n$  of length  $2l$  and  $\bar{n}_m$  is the element number  $m$  of  $\bar{n}$ . We want to first compute the sum over all Josephson junctions (sum over index  $j$ ). Since the dependencies on the Josephson junction only arise in the sine functions it suffices to examine the expression,

$$\sum_{j=1}^N \prod_{l=1}^{2l} \sin\left(\pi \frac{j\bar{n}_l}{N+1}\right) = \frac{1}{2^{2l-1}} \sum_{j=1}^N \sum_{\{\sigma\}} P(\sigma) \cos\left(\pi \frac{j \sum_{m=1}^{2l} \sigma_m \bar{n}_m}{N+1}\right), \quad (6.21)$$

where  $\{\sigma\}$  is the set of all  $2^{2l-1}$  different combinations  $\sigma$  of minus and plus signs, for example  $\sigma_l = \{-1, 1, 1, 1, -1, \dots, 1\}$ .  $P(\sigma)$  is the parity of the sign combination  $P(\sigma) = \prod_{m=1}^{2l} \sigma_m$ , which is either  $-1$  for combinations with an odd number of minus signs or  $1$  for combinations with a even number of minus signs. The sum over  $j$  can for each  $\nu = \sum_{m=1}^{2l} \sigma_m \bar{n}_m$  be simplified with,

$$\sum_{j=1}^N \cos\left(\pi \frac{j\nu}{N+1}\right) = \begin{cases} N & \text{if } \nu = 2(N+1)m \quad m \in \mathbb{N}_0 \\ -1 & \text{if } \nu \text{ even and } \nu \neq 2(N+1)m \quad m \in \mathbb{N}_0 \\ 0 & \text{if } \nu \text{ odd.} \end{cases}$$

To further evaluate (6.21), we thus need to analyze when  $\nu$  is even and whether there are cases of  $\nu = 2(N+1)m$  with  $m \in \mathbb{N}_0$ . Combinations of  $\bar{n}_l$  that contain an odd number

of odd manifold indices do not contribute because their sum can only be odd. This selection rule originates in the mirror symmetry of the device. Eigenmode functions with odd manifold index  $n$  are anti-symmetric, with respect to a symmetry axis perpendicular to the nonlinear resonator through its center, while eigenmode functions with even manifold index  $n$  are symmetric. Having ruled out combinations with an odd quantity of odd manifold indices, all contributing  $\nu$  must be even. If there are no  $\nu$  that are multiples of  $2(N+1)$ , then  $\sum_{j=1}^N \cos(\pi j \nu / (N+1)) = -1$  for all  $\nu$  and because of the equally distributed plus and minus signs of cosine terms, i.e. because  $\sum_{\{\sigma\}} P(\sigma) = 0$ , equation (6.21) is identically zero and the specific nonlinear coupling vanishes. There can thus only be non-vanishing couplings if there is at least one  $\nu = 2(N+1)m$  ( $m \in \mathbb{N}_0$ ). In fact, for every such  $\nu = 2(N+1)m$  there is another even  $\nu \neq 2(N+1)m$  with opposite parity so that the two terms add up to a pre-factor  $N+1$  in each non-vanishing coupling, see Eq. (6.20). Moreover, since

$$\sum_{j=1}^N \prod_{m=1}^{2l} \sin\left(\pi \frac{j \bar{n}_m}{N+1}\right) \leq \frac{N+1}{2}.$$

each coupling term between modes scales as  $(N+1)^\alpha$  with  $\alpha \leq -1$ .

### 6.4.3. Degeneracy Point

We have decomposed the linear part of the Lagrangian into independent eigenmodes, that are again coupled via  $H_{NL}$ . This coupling however is only relevant if the frequency difference between a pair of eigenmodes is comparable to their mutual coupling. Particularly interesting in this respect is the degeneracy point marked in figure 6.6,  $\omega_p = \bar{\omega}$ , with  $\bar{\omega} = \pi v(N+1)/L$ , where the plasma frequency coincides with the eigenmode frequencies of  $N$  modes. We therefore concentrate our further discussions on the vicinity of the degeneracy point where  $N$  eigenmodes with indices  $i = (n, k=2)$  become degenerate. Here,  $k$  can be interpreted as a band index since a mode-function with index  $k$  has  $k-1$  nodes between any pair of adjacent Josephson junctions, and  $n$  counts the modes within the band.

Our goal is to neglect any remaining coupling to the other eigenmodes in a “single-band approximation”. To confirm the accuracy of the single-band approximation applied at  $\omega_p = \bar{\omega}$ , we examine leading terms of the couplings between modes  $a_i$ . As we diagonalized the linear part of the Hamilton operator for the nonlinear resonator, there are no direct exchange coupling terms of the type,  $a_k^\dagger a_l + a_k a_l^\dagger$  in  $\bar{H}$ . However such terms emerge from the nonlinearity by virtue of the bosonic commutation relations if the raising and lowering operators are normal ordered. With the above derived selection rules for the nonlinearity we can compute these linear couplings between eigenmodes, c.f. eq. (6.20). Fig. 6.8 shows these couplings for a nonlinear resonator with 8 Josephson junctions. The coupling of every eigenmode with  $k=2$  with every eigenmode with  $k=1$  is calculated at the degeneracy point  $\omega_p = \frac{\pi v}{L}(N+1)$  and plotted in a color coded matrix plot. The strongest coupling, occurring between the seventh and fifth eigenmode, is plotted as a function of the plasma frequency  $\omega_p$ . For the couplings between all eigenmodes with  $k=2$  and  $k=3$  we did the same calculations and also plotted the result in figure 6.8. We observe that the couplings are always three orders of magnitude smaller than the fundamental mode



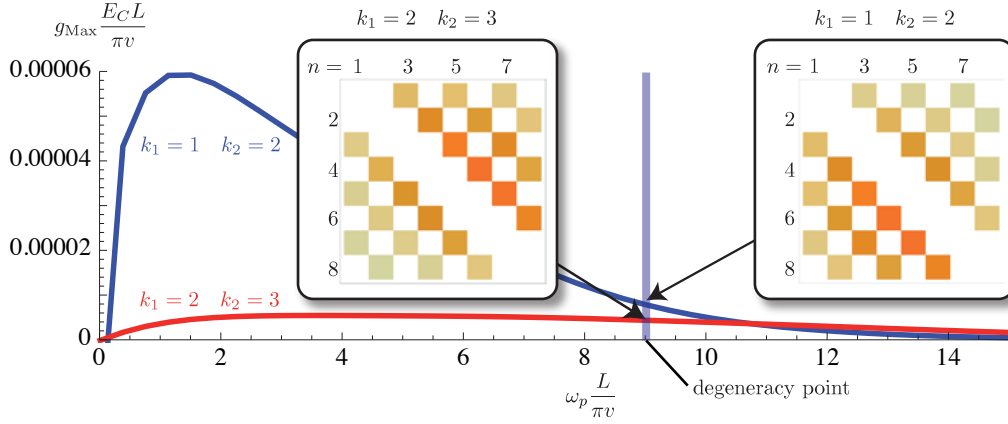


Figure 6.8.: Coupling between all eigenmodes with  $k = 1$  and  $k = 2$  and between all eigenmodes with  $k = 2$  and  $k = 3$  at the degeneracy point. For each case, the largest coupling  $g_{\text{Max}}$  in units of the fundamental mode frequency  $(\pi v)/L$  is plotted as a function of the plasma frequency  $\omega_p$  of the Josephson junctions.

frequency of the coplanar waveguide resonator. Therefore we can safely neglect all interactions between eigenmodes with different values of  $k$ . In agreement with the selection rules for the nonlinearity we find the checkerboard pattern for the coupling matrices showing that there is no coupling between a symmetric and an antisymmetric eigenmode.

We thus focus our analysis on modes with  $k = 2$  and the degeneracy point where their frequencies  $\omega_{n,2} \approx \bar{\omega}$ , so that they are described by the reduced Hamilton operator  $[H]_{k=2} = \sum_n \hbar \omega_n a_n^\dagger a_n + [H_{NL}]_{k=2}$  and skip the index  $k$  from now on:  $a_n \equiv a_{n,2}$  and  $\omega_n \equiv \omega_{n,2}$ .

**Local Modes** A new set of basis modes that arises from a unitary transformation of our degenerate eigenmodes will also be a set of eigenmodes for the nonlinear resonator with the same eigenfrequency  $\bar{\omega}$ . It is therefore beneficial to choose a new set of modes that facilitates the treatment of the nonlinearity. The total nonlinearity is the sum of the locally provided nonlinearities by the Josephson junctions. The above derived eigenmodes typically have comparable phase jumps at every Josephson junction. If we would find another set of eigenmodes at the degeneracy point with phase jumps only on one, but mutually different, Josephson junctions we would succeed in disentangling the coupling of the nonlinearity between eigenmodes.

The Hamilton operator for the eigenmodes in the vicinity of the degeneracy point is,

$$[\hat{\mathcal{H}}]_{k=2} = \hbar \sum_n \omega_n a_n^\dagger a_n - \frac{\varphi_0^2}{L_J} \sum_{j=1}^N \sum_{l=2}^{\infty} \frac{-1^l}{(2l)!} \left( \sqrt{\frac{2}{N+1}} \sum_{n=1}^N \sin\left(\pi \frac{jn}{N+1}\right) \frac{\hat{\phi}_n}{\varphi_0} \right)^{2l},$$

where  $\hat{\phi}_n = \lambda(\omega_n)(a_n + a_n^\dagger)$ . Note that if the zero point flux fluctuations  $\lambda(\omega_n)$  of the  $N$

degenerate eigenmodes were all equal and we used the transformation,

$$b_j = \sqrt{\frac{2}{N+1}} \sum_{n=1}^N \sin\left(\pi \frac{jn}{N+1}\right) a_n,$$

all modes  $b_j$  would decouple and the Hamilton operator would decompose into a sum of independent Hamilton operators describing identical Josephson junctions. Because of the subtle and from eigenmode to eigenmode differing renormalization of the zero point flux fluctuation the new eigenmodes  $b_j$  are still coupled. However we rewrite the Hamilton operator in terms of the new modes  $b_j$  assuming identical zero point flux fluctuations,

$$\lambda_0 = \sqrt{\frac{\hbar}{2C_J\omega_p}},$$

and append the deviations of the perfect symmetry as a correction in the coupling matrices,

$$[\hat{\mathcal{H}}]_{k=2} = \sum_{j=1}^N \left[ \hbar\bar{\omega} b_j^\dagger b_j + \hbar\bar{\omega} \sum_{l=1}^N u_{j,l} b_j^\dagger b_l - \frac{\varphi_0^2}{L_J} \sum_{m=2}^{\infty} \frac{(-1)^m}{(2m)!} \left( \frac{\hbar}{2\omega_p C_J \varphi_0^2} \right)^m \left( (b_j + b_j^\dagger) + \sum_{l=1}^N g_{j,l} (b_l + b_l^\dagger) \right)^{2m} \right]. \quad (6.22)$$

with the coupling matrices,

$$u_{j,l} = \frac{2}{N+1} \sum_{n=1}^N \sin\left(\frac{jn\pi}{N+1}\right) \sin\left(\frac{ln\pi}{N+1}\right) \left[ \frac{\omega_n}{\bar{\omega}} - 1 \right] \quad \text{and}$$

$$g_{j,l} = \frac{2}{N+1} \sum_{n=1}^N \sin\left(\frac{jn\pi}{N+1}\right) \sin\left(\frac{ln\pi}{N+1}\right) \left[ \frac{\lambda(\omega_n)}{\lambda_0} - 1 \right].$$

For the chosen Josephson junction capacitances  $C_J$  and coplanar waveguide resonator capacitance  $Lc$  these coupling matrices are small, i.e.  $\max(|u_{j,l}|) \ll 1$  and  $\max(|g_{j,l}|) \ll 1$ . For this reason we may only keep terms that couple modes up to linear order in  $g_{j,l}$  in the Hamilton operator. Importantly,  $\max(|g_{j,l}|) \ll 1$ , suppresses correlated tunneling [40] as the corresponding terms would be higher than linear order in  $g_{j,l}$ . Keeping only terms up to quartic order in the flux field amplitudes  $\hat{\phi}_n$  in Eq. (6.22) and performing a rotating wave approximation we arrive at the Hamiltonian,

$$H = \sum_{j=1}^N \left[ \hbar\bar{\omega} b_j^\dagger b_j - \frac{E_C}{2} b_j^\dagger b_j^\dagger b_j b_j \right] + \quad (6.23)$$

$$+ \hbar\bar{\omega} \sum_{j,l} u_{j,l} b_j^\dagger b_l - E_C \sum_{j,l} g_{j,l} \left( (b_j^\dagger b_j^\dagger b_j + b_j^\dagger) b_l + \text{H.c.} \right),$$

with the single Josephson junction charging energy  $E_C = e^2/(2C_J)$ . The resulting Hamilton operator describes a set of mutually coupled oscillators with Kerr type nonlinearities of strength  $E_C$  that can be substantial even on the single photon level. Interestingly the coupling is not only formed by linear particle exchange, but also contains a non-linear,

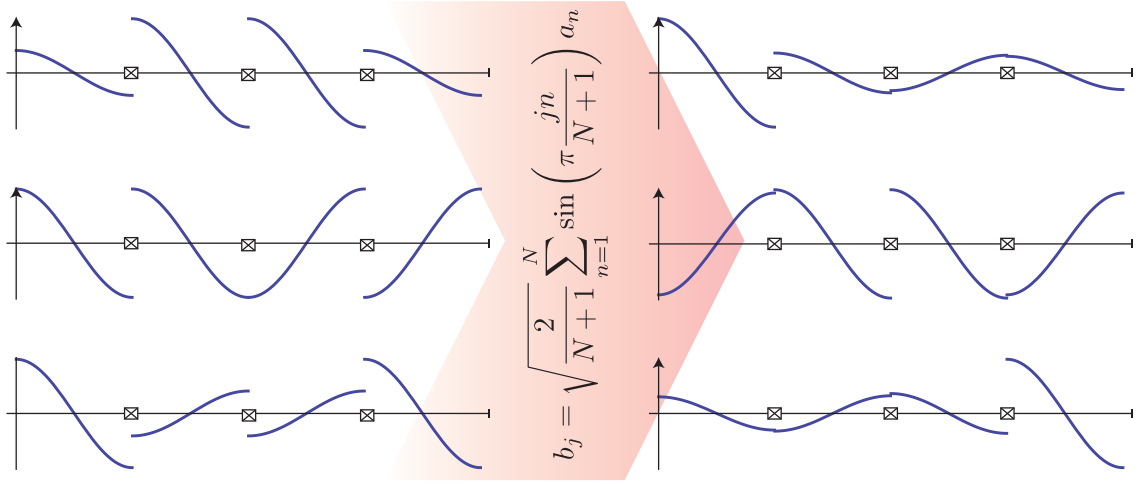


Figure 6.9.: Eigenmode functions with  $k = 2$  in arbitrary units at the degeneracy point for a nonlinear resonator with three Josephson junctions (crossed boxes). Left: flux functions associated to the mode operators  $a_n$ . Right: flux functions of modes  $b_j$  that minimize nonlinearity induced mixing.

density assisted excitation exchange. We thus have a rather unique situation, where a set of highly nonlinear modes form a narrow frequency band and can be efficiently driven by a single input tone.

As intended the flux functions of the modes  $b_j$  have a large flux drop at a specific Josephson junction and considerably smaller flux drops at all other Josephson junctions which can be seen in figure 6.9 where we plotted the flux functions of the degenerate “global” eigenmodes  $a_n$  together with their “local” counterparts for the modes  $b_j$

#### 6.4.4. Driven Dissipative Dynamics

The diagonalization of the microscopic Hamilton operator of a system of ultrastrongly interacting nonlinear oscillators with a resonator provides us with the rare opportunity to calculate transport behavior of such a system in the driven dissipative regime. With the introduction of the “local modes” in the previous chapter we detangled the ultrastrongly interacting subsystems into set of modes with considerably lower interaction strength that can be taken into account perturbatively in the following. To investigate the transport of microwave photons and the internal processes during transport, we want to concentrate our attention to the following situation: We weakly couple the nonlinear resonator from one side capacitively, with capacitance  $C_c$ , to a half-infinite transmission line. With this outlet we excite the nonlinear resonator with a sinusoidal microwave tone  $\phi_{ext}$  of frequency  $\omega_L$ . The energy stored in the coupling capacitance  $C_c$  is,

$$\tilde{H}_\Omega = \frac{C_c}{2} (\dot{\phi}_{ext} - \dot{\phi}|_{x=0})^2 = \frac{C_c}{2} (\dot{\phi}_{ext}^2 + \dot{\phi}|_{x=0}^2) - C_c \dot{\phi}_{ext} \dot{\phi}|_{x=0}.$$

We consider only small coupling capacitances and neglect a small renormalization of the eigenmode frequencies caused by the first two terms in the expanded coupling energy.

Moreover we choose the drive frequency to be near resonance with the modes  $a_n$  and neglect any coupling to other modes of the nonlinear resonator. Expressing the internal flux field  $\phi$  at the driven side of the resonator in terms of the lowering and raising operators of the eigenmodes  $a_n$  and  $a_n^\dagger$  we arrive at,

$$[\tilde{H}_\Omega]_{k=2} \approx H_\Omega = -C_c \dot{\phi}_{ext} \sum_n \dot{g}_n f_n(x)|_{x=0} = i \dot{\phi}_{ext} \sum_n \sqrt{\frac{\hbar \omega_p}{2\eta_n}} (a_n - a_n^\dagger).$$

Here we used the special normalization we have chosen for the flux functions of the eigenmodes, namely that they are all equal to one at the beginning of the nonlinear resonator. Next we unitarily transform to the  $b_j$  modes and express the classical drive as  $\dot{\phi}_{ext} = \Omega \sqrt{\frac{N+1}{\hbar \omega_p C_c^2}} \sin(\omega_L t)$  to get,

$$H_\Omega = i \sin(\omega_L t) \sum_{j=1}^N \underbrace{\Omega \left( \sum_{n=1}^N \frac{\sin\left(\pi \frac{jn}{N+1}\right)}{\sqrt{\eta_n}} \right)}_{\Omega_j} (b_j - b_j^\dagger).$$

Because of varying eigenmode capacitances  $\eta_n$  and varying values of the flux functions for modes  $b_j$ , at the side driven by the microwave tone, we get different effective driving strengths  $\Omega_j$ . We detect the excitation either with the reflected signal or by another infinite coplanar waveguide coupled capacitively to the other end of the nonlinear resonator. A completely analogous derivation leads to the input-output relation,

$$c_{OUT} = \sqrt{\kappa_x} \sum_j \tau_j b_j - c_{IN}$$

where  $\kappa_x$  is the decay rate into the output line and,

$$\tau_j = \sqrt{\frac{2}{(N+1) \sum_{n=1}^N \frac{1}{\eta_n}}} \sum_{n=1}^N (-1)^n \frac{\sin\left(\pi \frac{jn}{N+1}\right)}{\sqrt{\eta_n}}.$$

Assuming vacuum input noise outside the nonlinear resonator  $\langle c_{IN} \rangle = 0$  we compute the output intensity  $\langle c_{OUT}^\dagger c_{OUT} \rangle$  with the help of the input-output relation.

There are two different types of dissipative processes that enable microwave photons leaking out of the nonlinear resonator. Microwave photons decay through the capacitively coupled ends of the nonlinear resonator into the half infinite coplanar waveguides and there is dissipation due to two-level fluctuators in the Josephson junctions or the substrate material of the circuit QED setup. The latter source of dissipation is the same for every mode  $b_j$  since we assume the quality of every Josephson junction to be the same. Yet decay through the ends of the nonlinear resonator may be different for the individual modes  $b_j$  as they do not couple with the same strength to the in- and output coplanar waveguides. As we found this inhomogeneity to be very small, we opted to neglect it in this description. Therefore we here include dissipative processes with a standard master equation technique,

$$\dot{\rho} = \frac{i}{\hbar} [\rho, H_\Omega + H] + \frac{\kappa}{2} \sum_{j=1}^N (2b_j \rho b_j^\dagger - (\rho b_j^\dagger b_j + b_j^\dagger b_j \rho)),$$

where  $\kappa$  is the phenomenological decay rate assumed to be equal for all modes  $b_j$ . Assuming that the dominant dissipation mechanism is relaxation in the Josephson junctions, we employ here an independent bath approximation for the modes  $b_j$ .

**Mean Field Approximation** Due to a dynamical balance between constant injection and the leakage of microwave photons, as discussed in the preceding section, a steady state emerges. The effective Hamilton operator  $H$  that we derived above constitutes a set of nonlinear oscillators with interactions between every oscillator. Because of this high coordination number together with weak couplings  $|u_{j,l}|, |g_{j,l}| \ll 1$  a mean field approach to investigate the steady state is reasonable. We reduce the coupling to an interaction with the respective mean fields,

$$b_j^\dagger b_k \rightarrow \langle b_j^\dagger \rangle b_k + b_j^\dagger \langle b_k \rangle \quad \text{and}$$

$$(b_j^\dagger b_j^\dagger b_j + b_j^\dagger) b_k \rightarrow (\langle b_j^\dagger b_j^\dagger b_j \rangle + \langle b_j^\dagger \rangle) b_k + (b_j^\dagger b_j^\dagger b_j + b_j^\dagger) \langle b_k \rangle .$$

In a first step we calculate the mean fields  $\langle b_j^\dagger \rangle$  and  $\langle b_j^\dagger b_j^\dagger b_j \rangle$  individually for every mode  $b_j$  and ignore the coupling. We calculate the mean fields with a standard fock space truncation method with a variable truncation to ensure numerical correct values. Afterwards we update the driving amplitudes,

$$\Omega_j \rightarrow \Omega_j - i\bar{\omega} \sum_{k \neq j} u_{j,k} \langle b_j^\dagger \rangle + iE_C \sum_{k \neq j} g_{j,k} (\langle b_j^\dagger b_j^\dagger b_j \rangle + 2 \langle b_j^\dagger \rangle) ,$$

and introduce another nonlinear driving,

$$H_\Omega^{\text{nonlin}} = -E_C \sum_{j=1}^N \sum_{k \neq j} g_{j,k} (b_j^\dagger b_j^\dagger b_j \langle b_k \rangle + b_j^\dagger b_j b_j \langle b_k^\dagger \rangle) ,$$

which is why we can not use the exact solution to the single site problem [23], because the exact solution does not treat nonlinear driving. With the updated driving, which takes into account the driving of the modes among each other, we again calculate the mean fields  $\langle b_j^\dagger \rangle$  and  $\langle b_j^\dagger b_j^\dagger b_j \rangle$  and iterate the procedure until it converges.

**Synchronized Switching** We find that, upon increasing the intensity of a red detuned drive  $\omega_L = \omega_p - 4E_C/\hbar$  for  $\omega_p = \bar{\omega}$ , all modes switch synchronously and instantly from low occupancies to high photon numbers, see figure 6.10. This phenomenon can be understood as follows. Each mode  $b_j$  features a negative Kerr nonlinearity. Ignoring the inter-mode couplings, one would thus expect that the combination of slightly red detuned driving and negative nonlinearity leads to a switching behavior as a function of the drive strength since the Kerr nonlinearity can be interpreted as an intensity dependent frequency shift  $\delta\omega_j \sim (E_C/2\hbar)\langle b_j^\dagger b_j \rangle$  [23]. Hence, upon driving the oscillator increasingly strong the frequency will drop and, for a critical driving strength, eventually come into resonance with the drive, causing a growth of oscillator excitations. While switching in the higher excited state the modes also undergo a quantum to classical transition. For a red detuned drive of small amplitude they behave like qubits with a  $\pi$ -phase delay with respect to the drive

phase. After the switching into the higher excited state however the modes are in phase with the drive like harmonic oscillators with red detuned driving. As it turned out the nonlinear driving does not change qualitatively this behavior already observed without nonlinear driving.

Due to the different driving amplitudes  $\Omega_j$  one would expect a different critical drive strength for each mode  $j$ . Yet, the coupling  $g_{j,l}$  or classical drive, after our mean field approximation, between the modes is such that only modes  $b_j$  that are in phase amplify each other. When the mode with the lowest critical drive strength tries to switch it is getting weighed down because of the phase synchronizing features of the coupling  $g_{j,l}$ . Yet, if eventually a majority of modes switches into the higher excited state they drag the remaining modes with them, causing a very sharp and synchronized transition.

If we detune the plasma frequency of the Josephson junctions  $\omega_p$  from the point of degeneracy, we introduce additional mixing between the modes  $b_j$ , and, for detunings  $\Delta\omega > 4E_C$ , finally destroy the symmetry of the coupling that promotes synchronization of phases. As a consequence the synchronization of the switching behavior deteriorates and is eventually lost.

#### 6.4.5. Experimental Parameters

To examine the driven-dissipative dynamics of the nonlinear resonator at degeneracy of all its eigenmodes, as described above, one has to make sure at first that the plasma frequency at the degeneracy point is within the bandwidth of the detection chain and well below the superconducting gap. Typically one uses frequencies of 6 – 9 GHz in circuit QED setups. This implies half wave coplanar waveguide resonators of about 7 mm length at phase velocities of  $v = 0.98 \cdot 10^8 \frac{\text{m}}{\text{s}}$  in coplanar waveguides. At the degeneracy point half a wave length has to fit in between neighboring Josephson junctions which implies an overall nonlinear resonator length of  $(N + 1)0.007\text{m}$ . Additionally the nonlinear resonator has to be in the phase regime where zero point flux fluctuations are small compared to the rescaled quantum of flux  $\lambda(\omega_i) < \varphi_0$  which is why we have chosen to shunt each Josephson junction with an additional Capacitance  $C_J = 1\text{pF}$ . To be able to observe the transition of synchronized to non-synchronized  $b_j$ -modes, one has to change the magnitude of the Josephson inductance. This can either be achieved by designing different setups with different sizes of Josephson junctions or by using dc-superconducting quantum interference devices whose effective Josephson inductance can be tuned by threading a flux bias through their loops. The degeneracy point can be reached, given the above set of parameters, at  $L_J = 2.9\text{nH}$ . Therefore the Josephson inductance has to be tunable around  $L_J = 2.9\text{nH}$ . For our calculations in the driven-dissipative regime we have chosen a phenomenological decay rate of  $\kappa/(2\pi) = 20\text{MHz}$  for the modes  $b_j$ . The synchronization effect however is very robust against dissipation and the decay rates of actual experimental setups may be larger without any impact on synchronization. The suitable choice of parameters is summarized in table 6.2.

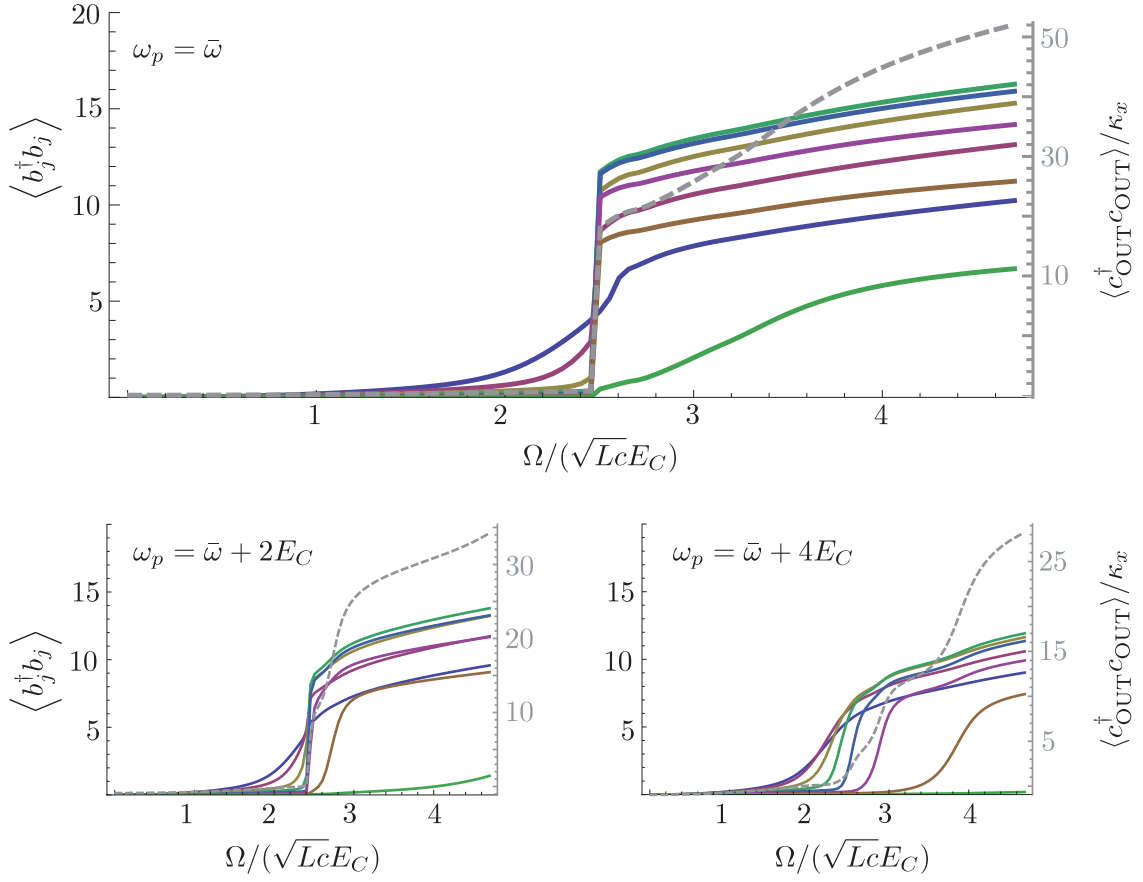


Figure 6.10.: Occupancies for the local modes  $b_j$  (colored solid lines) plotted as a function of the drive strength  $\Omega$  (scale at left vertical axes) at the degeneracy point  $\omega_p = \bar{\omega}$  for a nonlinear resonator with  $N = 8$  Josephson junctions (a) and for plasma frequencies  $\omega_p$  slightly detuned from the degeneracy point (b) and (c). The gray dashed line shows the output intensities (scale at right vertical axes).

Resonator	Josephson Junctions		
Length	$L = (N + 1)0.007\text{m}$	Shunting Capacitance	$C_J = 1\text{pF}$
Wave Impedance	$Z_0 = 50\Omega$	Josephson Inductance	tunable $L_J \approx 2.9\text{nH}$
Phase Velocity	$v = 0.98 \cdot 10^8 \frac{\text{m}}{\text{s}}$	$b_j$ decay rate	$\frac{\kappa}{2\pi} = 20\text{MHz}$

Table 6.2.: Parameters for an experimental realization of the coplanar waveguide resonator with multiple Josephson junctions.





## 7. Nonlinear Coupling

The Bose-Hubbard model with its linear inter-site exchange coupling and onsite Kerr nonlinearities presents the probably simplest implementation of an interacting many-body system that shows non-trivial behaviour. The microwave photons can move between sites via the inter-site exchange coupling and they interact due to the onsite Kerr nonlinearities. This interaction however is a zero-range contact interaction; microwave photons only interact if they are on the same site. This limitation of the interaction range can be overcome in the toolbox of superconducting circuits. With a capacitively shunted Josephson junction (c.f. fig.: 7.1) one can implement a nonlinear coupling between sites  $i$  and  $j$ . This nonlinear coupling effectively increases the range of the interaction indefinitely, since it is always possible to increase the number of connections between sites in the network. The Lagrangian of the coupling element reads,

$$\mathcal{L}_c = \frac{C_J}{2}(\dot{\varphi}_i - \dot{\varphi}_j)^2 + E_J \cos\left(\frac{\varphi_i - \varphi_j}{\varphi_0}\right),$$

with  $E_J$  the Josephson energy of the Josephson junction and  $C_J$  the sum of the intrinsic capacitance of the physical Josephson junction and an optional external shunting capacitance. The entire Lagrangian comprises all capacitive and inductive parts and may be expressed as,

$$\mathcal{L} = \frac{1}{2}\dot{\vec{\varphi}}^T \mathbf{C} \dot{\vec{\varphi}} - U(\vec{\varphi})$$

with  $\vec{\varphi}$  the vector of all node fluxes in the setup and  $\mathbf{C}$  the capacitance matrix. The Hamiltonian of the setup consequentially is,

$$\mathcal{H} = \frac{1}{2}\vec{q}^T \mathbf{C}^{-1} \vec{q} + U(\vec{\varphi}),$$

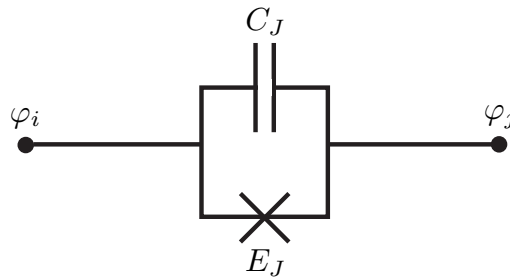


Figure 7.1.: Nonlinear coupling circuit between sites  $i$  and  $j$ . Shunting capacitance  $C_J$  combines the effects of the intrinsic capacitance of the physical Josephson junction and an additional external capacitance.

## 7. Nonlinear Coupling

---

with  $\vec{q}$  the canonical conjugate momenta of  $\vec{\varphi}$ . We may separate the capacitance matrix into a diagonal part, the self capacitances of the nodes, and a non-diagonal part, the coupling capacitances of the setup,  $\mathbf{C} = \mathbf{C}^{diag} + \mathbf{C}^{non-diag}$ . Assuming  $\mathbf{C}^{non-diag} \ll \mathbf{C}^{diag}$  we approximately invert the capacitance matrix to first order in  $\mathbf{C}^{non-diag}/\mathbf{C}^{diag}$ ,  $\mathbf{C}^{-1} \approx \mathbf{C}_{diag}^{-1} (1 - \mathbf{C}^{non-diag}/\mathbf{C}^{diag})$  and get the following Hamiltonian,

$$\mathcal{H} = \underbrace{\frac{q_i}{2\tilde{C}_i} + \frac{\varphi_i}{2\tilde{L}_i} + \frac{q_j}{2\tilde{C}_j} + \frac{\varphi_j}{2\tilde{L}_j}}_{\mathcal{H}_{(i,j)}^{lin}} + \overbrace{\frac{C_J}{\tilde{C}_i\tilde{C}_j} q_i q_j - \frac{1}{L_J} \varphi_i \varphi_j}_{\mathcal{H}_{(i,j)}^{lin}} - E_J \sum_{n=2}^{\infty} (-1)^n \frac{(\varphi_i - \varphi_j)^{2n}}{\varphi_0^{2n} (2n)!} + \mathcal{H}_{rest},$$

with,  $\tilde{C}_\alpha = \sum_{l_\alpha} C_{l_\alpha}$ , the sum of all capacitances of the branches ( $l_\alpha$ ) connected to node  $\alpha=i$  or  $j$  and,  $1/\tilde{L}_\alpha = \sum_{l_\alpha} 1/L_{l_\alpha}$ , the corresponding sum over all inverse inductances. Here we already separated the linear parts involving nodes  $i$  and  $j$  and their coupling from the nonlinear contributions and everything else,  $\mathcal{H}_{rest}$ . With this we may proceed with the quantization of the theory by introducing bosonic lowering and raising operators for the nodes  $i$  and  $j$ ,

$$\hat{\varphi}_\alpha = \frac{1}{\sqrt{2}} \left( \frac{\tilde{L}_\alpha}{\tilde{C}_\alpha} \right)^{\frac{1}{4}} (a_\alpha + a_\alpha^\dagger) \quad \hat{q}_\alpha = \frac{i}{\sqrt{2}} \left( \frac{\tilde{C}_\alpha}{\tilde{L}_\alpha} \right)^{\frac{1}{4}} (a_\alpha^\dagger - a_\alpha).$$

The linear part of the Hamilton operator involving nodes  $i$  and  $j$  and their coupling now reads,

$$H_{(i,j)}^{lin} = \omega_i a_i^\dagger a_i + \omega_j a_j^\dagger a_j - \sqrt{\omega_i \omega_j} \alpha_- (a_i^\dagger a_j + a_i a_j^\dagger) - \sqrt{\omega_i \omega_j} \alpha_+ (a_i^\dagger a_j^\dagger + a_i a_j) \quad (7.1)$$

with the oscillation frequencies  $\omega_\alpha = 1/\sqrt{\tilde{L}_\alpha \tilde{C}_\alpha}$  and,

$$\alpha_\pm = \left( \frac{\sqrt{\tilde{L}_i \tilde{L}_j}}{L_J} \pm \frac{C_J}{\sqrt{\tilde{C}_i \tilde{C}_j}} \right).$$

Next we truncate the nonlinearity of the coupling Josephson junction to fourth order. This is valid as long as zero point fluctuations in the node fluxes are small,  $(L_\alpha/C_\alpha)^{1/4} \ll \varphi_0$ , and we are only considering the lowest excited states of the node fluxes. We further assume that the eigenfrequencies of node  $i$  and  $j$  are large compared to the coupling between the two and neglect rotating terms in a rotating wave approximation. The approximate Hamilton operator in this parameter regime is,

$$H \approx ((\omega_i + \delta\omega_i) a_i^\dagger a_i - U_i a_i^\dagger a_i^\dagger a_i a_i) + ((\omega_j + \delta\omega_j) a_j^\dagger a_j - U_j a_j^\dagger a_j^\dagger a_j a_j) + H_{(i,j)} + H'_{rest},$$

where  $\langle i, j \rangle$  parametrizes the nonlinear coupling circuit between nodes  $i$  and  $j$ . Each node has a nonlinear onsite term due to the nonlinear terms in the coupling Hamilton operator.

Additionally the eigenfrequencies of the nodes are slightly renormalized due to terms that are generated during the normal ordering process of the the nonlinear terms. Since these terms are a sum of all nonlinear branches connected to node  $i$  and  $j$  we can not further specify their form. We may provide some examples in the following two sections (c.f. section 7.1 and section 7.2). Finally the coupling between node  $i$  and  $j$  reads,

$$\begin{aligned}
 H_{\langle i,j \rangle} &= H_{\langle i,j \rangle}^{\text{lin}} - H_{\langle i,j \rangle}^{\text{cross-Kerr}} + H_{\langle i,j \rangle}^{\text{assist-tunnel}} - H_{\langle i,j \rangle}^{\text{squeeze}} \\
 H_{\langle i,j \rangle}^{\text{cross-Kerr}} &= 2E_C^{iijj} \frac{\sqrt{\tilde{L}_i \tilde{L}_j}}{L_J} a_i^\dagger a_i a_j^\dagger a_j \\
 H_{\langle i,j \rangle}^{\text{assist-tunnel}} &= E_C^{iiij} \frac{(\tilde{L}_i^3 \tilde{L}_j)^{1/4}}{L_J} (a_i^\dagger a_i^\dagger a_i a_j + \text{h.c.}) + E_C^{ijjj} \frac{(\tilde{L}_i \tilde{L}_j^3)^{1/4}}{L_J} (a_i^\dagger a_j^\dagger a_j a_j + \text{h.c.}) \\
 H_{\langle i,j \rangle}^{\text{squeeze}} &= \frac{E_C^{iijj}}{2} \frac{\sqrt{\tilde{L}_i \tilde{L}_j}}{L_J} (a_i^\dagger a_i^\dagger a_j a_j + \text{h.c.})
 \end{aligned}$$

It consists of the desired cross-Kerr, or density-density interaction,  $H_{\langle i,j \rangle}^{\text{cross-Kerr}}$ , a assisted tunneling term  $H_{\langle i,j \rangle}^{\text{assist-tunnel}}$  and a two-mode squeezing term  $H_{\langle i,j \rangle}^{\text{squeeze}}$ .

$$E_C^{\alpha\beta\gamma\delta} = \frac{e^2}{2(\tilde{C}_\alpha \tilde{C}_\beta \tilde{C}_\gamma \tilde{C}_\delta)^{1/4}},$$

is the generalized charging energy with  $\alpha, \beta, \gamma, \delta = i$  or  $j$ . A remarkable feature of the above presented nonlinear coupling is the possibility to compensate the linear capacitive and inductive coupling in the coupling element (c.f. equation 7.1) for certain parameter choices. The nonlinear coupling is the only remaining coupling in this case. The density-density coupling is the most robust coupling compared to the assisted tunneling and two-mode squeezing coupling because it is immune to the inevitable variances in the eigenfrequencies of the nodes of the lattice.

## 7.1. Cross-Kerr Nonlinearities

With the above introduced nonlinear coupling between sites one can now build a Bose-Hubbard lattice with nonlinear inter-site coupling. We consider a network of oscillators, that can either be implemented as lumped element resonators or as single modes of a coplanar resonator (c.f. figure 7.2). These sites are connected via the above presented capacitively shunted Josephson junctions. The Josephson junctions could be realized as small SQUIDs thus implementing a means for in-situ tunability of linear direct exchange coupling versus nonlinear interaction terms. Additionally one could couple each site to a superconducting qubit or introduce on-site interactions with the scheme presented in chapter 6.

The most suitable regime for the operation of quantum simulators based on microwaves in superconducting circuits is the driven dissipative regime. Similar to the considerations of chapter 5 we consider the situation where every site is driven by a coherent microwave

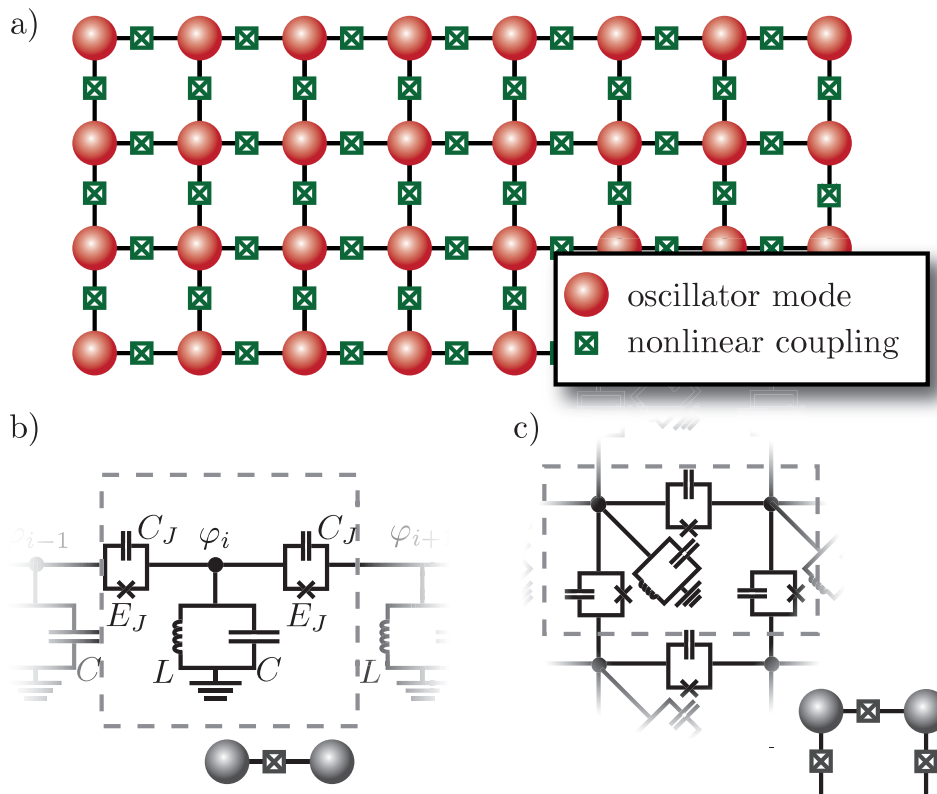


Figure 7.2.: Electrical circuit sketch of the setup we envision to realize a system with cross-Kerr nonlinearities. A chain of lumped element LC-circuits is coupled via capacitively shunted Josephson junctions. The Josephson energies could be tuned in situ by replacing the Josephson junctions with superconducting interference devices

source with strength  $\Omega$  and detuning  $\delta$  from the frequency of site  $i$ . Due to constant injection of microwaves and the inevitable leakage, steady states emerge. We are interested in the properties of these steady states. The Hamilton operator, in the frame rotating with the microwave drives, for a network of identical sites with identical coupling circuits is,

$$H = \sum_i \left[ -\delta n_i + \Omega(a_i + a_i^\dagger) \right] - J \sum_{\langle i,j \rangle} (a_i^\dagger a_j + a_i a_j^\dagger) + U \sum_i n_i(n_i - 1) + V \sum_{\langle i,j \rangle} n_i n_j + \frac{V}{4} \sum_{\langle i,j \rangle} \left[ a_i^\dagger a_i^\dagger a_j a_j - 2(a_i^\dagger(n_i + n_j)a_j + a_i(n_i + n_j)a_j^\dagger) \right].$$

Here we considered an onsite interaction  $U$ , an inter-site exchange coupling  $J$  and finally the inter-site density-density interaction, the assisted tunneling and two-mode squeezing interactions are all parameterized by  $V$ . The onsite interaction  $U$  and the group of nonlinear couplings between sites ( $V$ ) can be tuned independently by adding arbitrary onsite nonlinearities. The nonlinear coupling  $V$  and the linear exchange coupling  $J$  can be tuned independently with the mutual cancelation of capacitive and inductive linear exchange coupling, as explained above. However the ratios of the three different types of nonlinear couplings can not be altered due to their common origin in the fourth order term of the coupling Josephson junction. We may however realize that out of these three nonlinear coupling terms the density-density interaction is the only interaction that is independent of the frequency detuning between neighboring sites. For vanishing linear exchange coupling we can therefore suppress the assisted tunneling and two-mode squeezing terms by detuning the sites in a checkerboard pattern. If we adjust the frequencies of the microwave drives accordingly, we still retain the site-independent Hamilton operator in a frame rotating with the microwave drives. If the linear exchange coupling is non-vanishing it typically dominates the assisted tunneling and two-mode squeezing terms. Since the effects of these coupling terms are quite similar [41] we can neglect the effect of the assisted tunneling and two-mode squeezing terms altogether. We model the decay with a standard master equation where we assume uncorrelated decay into zero temperature reservoirs at each site  $i$ ,

$$\dot{\rho} = -i[H, \rho] + \frac{\kappa}{2} \sum_i (2a_i \rho a_i^\dagger - n_i \rho - \rho n_i),$$

with empirical decay rates  $\kappa$ .

It is already known that for two-level systems with inter-site density-density interactions, i.e. the limit  $U \rightarrow \infty$  of our system, an antiferromagnetic phase emerges [50]. We expect to see something similar for finite  $U$  where there is a competition between onsite and inter-site interaction: A phase with alternating occupation  $\langle a_i^\dagger a_i \rangle$  that breaks the symmetry of the network of identical sites. Henceforth we call this phase “photon crystal” in analogy to the periodic arrangement of interacting atoms that breaks the continuous translational symmetry of the three dimensional space itself. For networks with high coordination numbers we expect a meanfield approximation to be accurate. To capture the emergence of a photon crystal however we subdivide the network into two sub-networks  $A$  and  $B$  such that sites of sub-network  $A$  only interact with sites of sub-network  $B$ . For a two-dimensional square lattice this would imply a checkerboard pattern of “ $A$ ”- and “ $B$ ”-sites (c.f. figure 7.2). Sub-network  $A$  has  $N$  sites while sub-network  $B$  has  $M$  sites.

## 7. Nonlinear Coupling

---

We assume sites of the same sub-network to have the same mixed state but allow differences in the states between the sub-networks,  $\rho = \prod_{i \in A} \rho_i \prod_{j \in B} \rho_j = \rho_A^{\otimes N} \rho_B^{\otimes M}$ , and get the following mean field decoupling,

$$\begin{aligned} z^{-1} \sum_{\langle i,j \rangle} n_i n_j &\longrightarrow \langle n_A \rangle \sum_{j \in B} n_j + \langle n_B \rangle \sum_{i \in A} n_i \\ z^{-1} \sum_{\langle i,j \rangle} a_i^\dagger a_j &\longrightarrow \langle a_A^\dagger \rangle \sum_{j \in B} a_j + \langle a_B^\dagger \rangle \sum_{i \in A} a_i \\ z^{-1} \sum_{\langle i,j \rangle} a_i^\dagger a_i^\dagger a_j a_j &\longrightarrow \langle a_A^\dagger a_A^\dagger \rangle \sum_{j \in B} a_j a_j + \langle a_B^\dagger a_B^\dagger \rangle \sum_{i \in A} a_i a_i, \end{aligned}$$

with  $z$  the coordination number of the network. The dynamics is thus reduced to two coupled nonlinear equations for the density matrices of the  $A$  and  $B$  sub-networks, respectively  $\rho_A$  and  $\rho_B$ ,

$$\begin{aligned} \dot{\rho}_A &= -i[H_A, \rho_A] + \frac{\kappa}{2}(2a_A \rho_A a_A^\dagger - n_A \rho_A - \rho_A n_A) \\ \dot{\rho}_B &= -i[H_B, \rho_B] + \frac{\kappa}{2}(2a_B \rho_B a_B^\dagger - n_B \rho_B - \rho_B n_B), \end{aligned} \tag{7.2}$$

with the effective meanfield Hamilton operators,

$$\begin{aligned} H_A &= -\delta n_A + \Omega(a_A + a_A^\dagger) + U n_A (n_A - 1) + z V w_B n_A - z J(\psi_B a_A^\dagger + \text{h.c.}) \\ H_B &= -\delta n_B + \Omega(a_B + a_B^\dagger) + U n_B (n_B - 1) + z V w_A n_B - z J(\psi_A a_B^\dagger + \text{h.c.}). \end{aligned}$$

Here we already neglected the assisted tunneling and two-mode squeezing terms. The expectation values for the occupation  $w_{A/B} = \text{tr}(n_{A/B} \rho_{A/B})$  and amplitude  $\psi_i = \text{tr}(a_{A/B} \rho_{A/B})$  provide the nonlinear coupling mechanism for the meanfield master equations 7.2.

The emergence of a photon crystal manifests itself as a stationary solution ( $\dot{\rho}_A = 0$  and  $\dot{\rho}_B = 0$ ) with non-equal occupations for the sub-networks,  $\langle n_A \rangle \neq \langle n_B \rangle$ . The difference in occupation for the two sub-networks,  $\Delta n = |\langle n_A \rangle - \langle n_B \rangle|$ , therefore lends itself as an indicator for the presence of the photon crystal. Henceforth we only consider the situation of resonant microwave drives,  $\delta = 0$ , consequentially every nonlinearity, irrespective of their sign, can be thought of as a repulsive interaction.

For vanishing linear exchange coupling between the sites,  $J = 0$ , the emergence of the photon crystal is a competition between the on-site interaction,  $U$ , and inter-site interaction,  $V$ . In order to minimize on-site interaction  $U$ , a steady state of evenly distributed microwave photons is preferred while a minimization of the inter-site interaction  $V$  favors a steady state with alternating occupation, i.e.  $\Delta n \neq 0$ . Consequently there is for every value of  $U$  a critical value of the inter-site interaction  $V_c$  which marks the onset of the photon crystal (c.f. figure 7.3 a). This critical inter-site interaction  $V_c$  is a strictly monotonically increasing function of the on-site interaction  $U$ . For vanishing on-site interaction  $U$  there is still a finite critical inter-site interaction,  $zV_c \simeq \gamma_0(-2\delta + \sqrt{\gamma_0})/4\Omega^2$  with  $\gamma_0 = 4\delta^2 + 1$ , highlighting the role of the coherent microwave drives as a force which can drive the network into a crystalline phase. For finite on-site interaction  $U$  however the situation changes: for

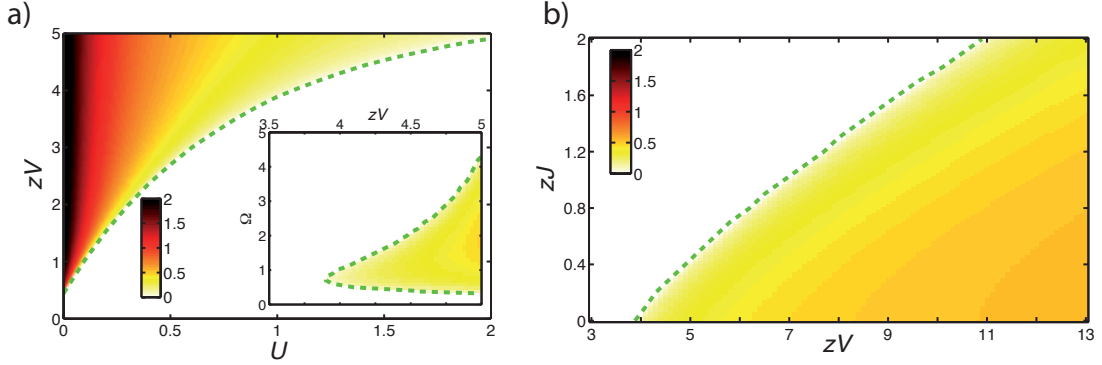


Figure 7.3.: a) Color coded density plot of  $\Delta n$  for the photon crystal in the  $U - V$  plane for vanishing inter-site exchange coupling  $J$ . If the cross-Kerr term exceeds a critical threshold  $V_c$ , the steady state is characterized by a staggered order in which  $\Delta n \neq 0$ . Here we fixed  $\Omega = 0.75\kappa$  and  $\delta = 0$ . In the inset we show  $\Delta n$  as a function of  $\Omega$  and  $V$  at a fixed value of  $U = \kappa$ . b) Color coded density plot of  $\Delta n$  for the photon crystal at finite inter-site exchange coupling.  $\Delta n$  is plotted as a function of  $J$  and  $V$ , for  $\delta = 0$  and  $U = \kappa$ . Here we fixed  $\Omega = 0.75\kappa$ .

small driving strength  $\Omega$  the networks total microwave occupation is not enough to probe the effects of the interaction. For intermediate driving strength  $\Omega$ , a photon crystal can emerge that gets destroyed again for strong driving (c.f inset of figure 7.3 a). For strong driving and finite on-site interaction the identical microwave drives thus reveal their tendency to equally distribute microwave photons in the network. Finite linear inter-site exchange coupling promotes the mobility of the microwave photons in the network and therefore inhibits the formation of the photon crystal (c.f figure 7.3 b)

## 7.2. Quantum Single-Photon Transistor

Another interesting application for the nonlinear density-density interaction can be thought of in the area of coherent manipulation of itinerant microwave photons. Deterministic generation of itinerant microwave photons in a circuit QED setup is quite simple: A qubit that is driven with a suitable Rabi pulse to its excited state and subsequently decays into a half infinite coplanar waveguide, generates almost perfect itinerant, single photon pulses traveling along coplanar waveguides [24]. Imagine an array of these deterministic single-photon sources arranged such that the coplanar waveguides could approach each other and interact via additional control circuitry in a predetermined manner (c.f. figure 7.4 a). If this control circuitry would be identical for every approach of coplanar waveguides and symmetrical in the sense that if we exchanged the itinerant microwave photons right before their interaction the working of the control circuitry would not change, then we could build an network to synthesize arbitrary states of multiple itinerant microwave photons.

We came up with a control circuitry that could block or unblock a single itinerant microwave photon dependent on the presence or absence of another single microwave photon. We dubbed it “Single-Photon Transistor” because a single photon could route another

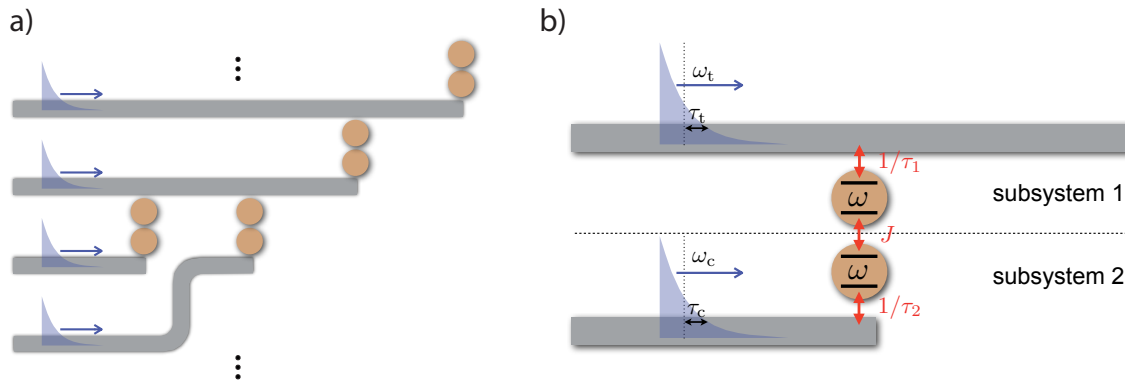


Figure 7.4.: a) Scheme to synthesize arbitrary states with itinerant microwave photons. Grey lines are coplanar waveguides and the two circles are the control circuitry mediating interaction, explained in more detail in b). b) Detailed view of the single-photon transistor. Two transmon qubits are coupled together with  $\sigma_z \sigma_z$  coupling and to a half-infinite and infinite coplanar waveguide respectively.

single photon in analogy to a transistor in a computer chip, where the transistor provides a means to switch current with current.

A plane wave traveling along a one-dimensional waveguide that is coupled to a qubit will excite the qubit. Subsequently the qubit will decay into a wave mode symmetric with respect to the position of the qubit. The plane wave however is asymmetric with respect to the position of the qubit. Constructive or destructive interference between the original plane wave and the decay-pulse of the qubit can cause anything between total reflection and transmission of the original plane wave. A single-photon wave packet as emitted by a decaying qubit centered around the frequency of the scattering qubit is reflected if the width of the wave packet in  $k$ -space is smaller than the coupling strength of the qubit to the one-dimensional waveguide  $1/\tau$ . However a sufficiently detuned wave packet will get transmitted without reflection.

The qubit is excited during the scattering process. To maximize this excitation of the qubit we have to time-invert the decay pulse of the qubit being initially in his excited state [15], also called inverting pulse. That is why a qubit coupled to a infinite one-dimensional waveguide can only be fully excited by sending signals from both directions. If we want to achieve complete excitation of a qubit, with a single pulse, we have to consider a half infinite one-dimensional waveguide with the qubit coupled to the end of the line.

We combine these two principles to build a single-photon transistor (c.f figure 7.4 b). Two identical transmon qubits with transition frequency  $\omega$  are coupled capacitively with coupling strengths  $1/\tau_1$  and  $1/\tau_2$  to two coplanar waveguides respectively. One half infinite coplanar waveguide which will guide the “control”-photon with temporal width  $\tau_c$  and one infinite waveguide for the “target”-photon of temporal width  $\tau_t$ . A one-photon inverting pulse,  $\tau_c = \tau_2$ , can maximally invert the control transmon qubit. The two transmon qubits are coupled via the capacitively shunted Josephson junction as explained above. We arrange things such that the linear exchange coupling vanishes. With the technique of can-



celing the linear inductive coupling with the linear capacity coupling, we also can get rid of any remaining geometric coupling of stray capacitances or stray inductances. The remaining  $\sigma^z\sigma^z$ -coupling can be thought of as a frequency shift of the target transmon qubit that depends on the excitation of the control transmon. Therefore the target transmon qubit can be shifted out of resonance or into resonance dependend on the absence or presence of a control photon inverting pulse. We assume a Lorentzian shape in frequency space for the target photon which enables the traget photon to be a inverting pulse which could serve as the control photon at the next single-photon transistor. The Hamilton operator for the whole setup reads,

$$H = H_{\text{sys}} + H_{\text{cpw}} + H_{\text{int}}, \quad (7.3)$$

with the Hamilton operator of the two qubits and the coupling circuit,

$$H_{\text{sys}} = \frac{\omega}{2}\sigma_1^z + \frac{\omega}{2}\sigma_2^z - V\sigma_1^z\sigma_2^z. \quad (7.4)$$

We only consider the transmon qubits and their coupling in their separate subspaces of a single excitation. This is valid since we do not have any direct exchange of excitations between the subsystem 1 comprising the target photon and transmon qubit and subsystem 2 comprising the control photon and transmon qubit. The Hamilton operator of the coplanar waveguides is,

$$H_{\text{cpw}} = \int_{-\infty}^{\infty} dp p (r_p^\dagger r_p - l_p^\dagger l_p) + \int_{-\infty}^{\infty} dp p b_p^\dagger b_p. \quad (7.5)$$

The continuum of modes for the infinite coplanar waveguide consists of left,  $l_p$ , and right,  $r_p$ , moving modes while the modes of the half infinite coplanar waveguide are non-degenerate. We assume a linear dispersion relation with mode index  $p = v_g \eta$  measured from the qubit frequency.  $v_g$  is the group velocity and  $\eta$  the wave vector. We extend the integral over  $p$  from  $-\omega$  to infinity to minus infinity to infinity since we only consider microwave pulses with a pulse width much smaller than their carrier frequency. The coupling Hamilton operator between the coplanar waveguides and the transmon qubits is,

$$H_{\text{int}} = \int_{-\infty}^{\infty} dp \left[ \frac{\sigma_1^+(r_p + l_p)}{\sqrt{2\pi\tau_1}} + \frac{\sigma_2^+ b_p}{\sqrt{\pi\tau_2}} + \text{h.c.} \right]. \quad (7.6)$$

We assume a point-like, frequency independent interaction with associated lifetimes for the transmon qubits  $\tau_1$  and  $\tau_2$ . In a realistic system, the qubits will be subject to dissipation. We thus assume relaxation of excited transmon qubit levels at a rate  $\gamma_r$  and pure qubit dephasing at a rate  $\gamma_\varphi$  to derive quantum Langevin equations for the photon and qubit operators that describe the unitary dynamics generated by  $H$  and the dissipative processes associated to  $\gamma_r$  and  $\gamma_\varphi$ . To investigate the dynamics of “single-photon” pulses in this setup, we combine quantum scattering theory with the input-output formalism of quantum optics as in [25], where the source terms for the input-output relations are provided by the solutions of the mentioned Langevin equations.

We have chosen to operate the transistor such that the target photon is reflected in the absence but unaffected in the presence of the control photon and therefore arranged the center frequencies of the control and target single-photon wave packets to be,  $\omega_c = \omega_t = \omega + 2V$ . We quantify the performance of the single-photon transistor via the difference  $C_s$

## 7. Nonlinear Coupling

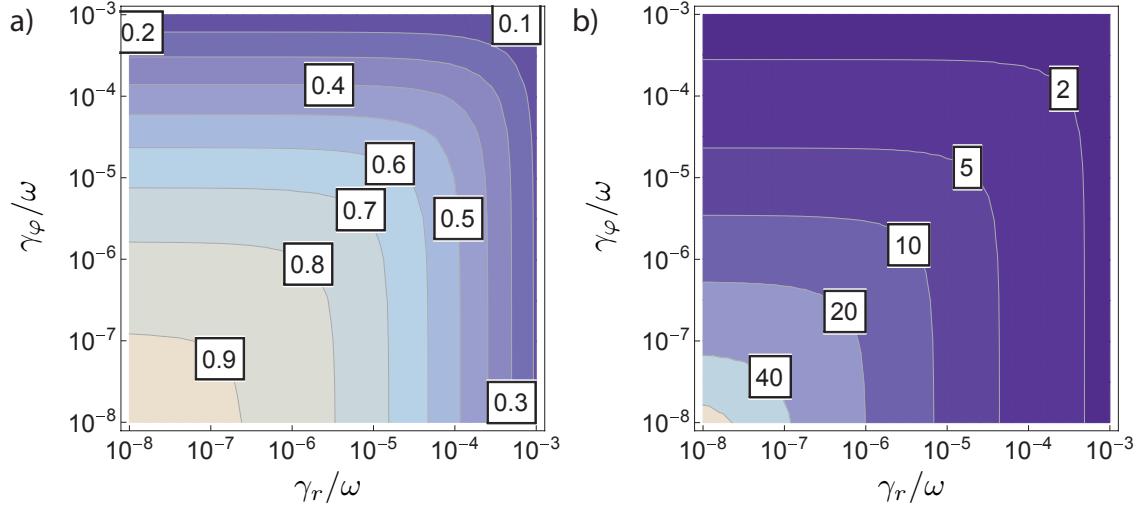


Figure 7.5.: Performance of the single-photon transistor. a) Maximized contrast  $C_s = p_{TC} - p_T$  as a function of the rates for qubit relaxation,  $\gamma_r$ , and pure dephasing,  $\gamma_\phi$ , for  $\omega_c = \omega_t = \omega + 2V$ ,  $\tau_1 = 200/\omega$ ,  $J = 0.01\omega$  and  $\tau_c = \tau_2$ . b) On-off ratio  $R_s = p_{TC}/p_T$  for the same parameters.

and ratio  $R_s$  between the transmission probabilities for the target photon in the presence  $p_{TC}$  and absence  $p_T$  of a control photon,

$$C_s = p_{TC} - p_T \quad \text{and} \quad R_s = p_{TC}/p_T, \quad (7.7)$$

For  $C_s = 1$  the setup would describe an ideal transistor for single photons. Figure 7.5 shows the achievable transmission contrast,  $C_s$ , and on-off ratio,  $R_s$ , for a realistic device with a qubit-qubit coupling of  $V = 0.01\omega$  and  $\omega\tau_1 = 200$  as a function of the relaxation rate  $\gamma_r$  and pure dephasing rate  $\gamma_\phi$  of the transmon qubits. As the plots show, an ideal single-photon transistor can be realized in the limit of vanishing  $\gamma_r/\omega$  and  $\gamma_\phi/\omega$  whereas very good performance can already be expected for currently realized values of  $\gamma_r/\omega \sim 10^{-6}$  and  $\gamma_\phi/\omega \sim 10^{-6}$ , where a single control photon changes the transmission probability for the target photon by a factor 20. Transmission contrast and on-off ratio have been optimized with respect to the temporal widths of target,  $\tau_t$  and control pulses,  $\tau_c$ .

## 8. Outlook

### 8.1. Future directions of circuit quantum electrodynamics

The scaling up of superconducting circuits will continue, posing mainly engineering problems. The number of parameters to be controlled on a chip increases linearly with its complexity. This immediately implies new challenges for the control wiring coming from high-temperature stages of the cryostat. Every wire running from a high temperature stage to the chip introduces noise on the chip. Future setups will therefore incorporate on-chip classical-logic elements to enable digital multiplexing of instructions sent to the chip rather than the analog, direct control of circuit QED chips nowadays. But the increasing size of chips not only generates engineering issues in the infrastructure around the chip but also complicates chip design itself. The groundplane on the chip will be cut into multiple pieces by the increasing number of waveguides, resonators and superconducting qubits. If the groundplane to the left and right of waveguides is not held at the exact same electrical potential we open the channel to slotline modes which introduce decay. Therefore an intricate system of airbridges has to be introduced to suppress the slotline modes [77]. Additionally there are still material science problems to tackle to further increase qubit coherence. The influence of two level defects in the amorphous substrate material and non-equilibrium quasi-particle production due to stray infrared fields has to be diminished [62].

Meanwhile theoretical work has to overcome its heterogenic structure. Each building block starting from the three basic charge-, flux- and phase-qubits, over to the more exotic quantronium- [86] and fluxonium-qubits [58] to the coplanar waveguide resonators has its own set of techniques to understand its eigensystem. The modeling of the superconducting circuits starting from the electrodynamics of the three-dimensional setup to the circuit representation [75] and from there to the formulation in the Lagrangian formalism and the quantisation [19] are well established and most importantly fairly generic with respect to different setups. Diagonalisation techniques for the Hamilton operators however are fragmented with only very narrowly restricted areas of applicability. Therefore the current approach for the description of large systems involves the combination of already diagonalised subsystems with moderate coupling strengths in order not to render the approximations for the subsystems invalid. This situation quite paradoxically restricts the design freedom of actual experiments for superconducting circuits. The extraordinary large couplings between the sub-systems are being restricted in order to comply to the above described two-step theory approach to large superconducting circuits. There are efforts to overcome this hurdle with group-theory [26] and an ansatz coined “Black-Box Superconducting Circuit Quantization” [68]. The ansatz of black box circuit quantisation is the subdivision of the whole Hamiltonian into a linear and non-linear part as pioneered in works related to Josephson junction intersected coplanar waveguides [11, 52]. This ansatz specifically acknowledges the strong coupling between the sub-systems and treats the non-linearity rather than the coupling between sub-systems as a perturbation. Black-box circuit

quantisation was developed with planar superconducting circuits embedded in three dimensional microwave cavities in mind. The linear part of the Hamiltonian for the setup with three-dimensional cavities can be diagonalised with finite element methods and subsequently quantised. The nonlinearity could be expressed in terms of lowering and raising operators of the eigenmodes of the linear part of the Hamiltonian. With this sequence one could reliably get the eigensystems of arbitrary three dimensional setups. However there are also more advanced methods which allow for a more profound insight into the physics of planar superconducting circuits which we are going to present below.

### 8.2. Quantum Graph models and Transfer Matrices

One difficulty in the modeling of planar superconducting circuits is the coexistence and strong coupling of elements that are large and elements that are small with respect to the wavelength of the microwaves. The elements that are large with respect to the wavelength, also called distributed elements, are the coplanar waveguides. The transverse dimension of coplanar waveguides is small enough to be well within the quasi one-dimensional limit. Therefore the state of the coplanar waveguide can be completely described by the one-dimensional flux function  $\phi(x, t)$ . The time derivative of the flux function is the electrical potential of the central line with respect to the surrounding groundplane  $V(x, t) = \partial_t \phi(x, t)$  and the spatial derivative divided by the inductance per unit length is the current through the coplanar waveguide  $I(x, t) = (1/l)\partial_x \phi(x, t)$ . The coplanar waveguides are linear elements of the setup and their equation of motion as given by the linear part of the Hamiltonian is a wave equation  $\partial_t^2 \phi - v^2 \partial_x^2 \phi = 0$ , with the phase velocity defined by inductance and capacitance per unit length of coplanar waveguide  $v = 1/\sqrt{lc}$ . In a typical setup of planar superconducting circuits the coplanar waveguides are composed in a network with multiple nodes where Kirchhoffs rules have to be enforced. As such the network of coplanar waveguides is a perfect representation of a quantum graph model. Quantum Graphs were introduced in the 1930s by Linus Pauling as a model for free electrons in organic molecules however they arise as mathematical models in various experimental contexts such as photonic crystals or mesoscopic systems in nanotechnology. However so far the vast amount of insights in the spectrum and eigenmodes of quantum graphs [7] has not been tapped for the network of coplanar waveguides.

In addition to the network of coplanar waveguides, typical superconducting circuits also have structures which are smaller than the wavelength, so called lumped element circuits. These are circuits composed of capacitors, inductors and Josephson junctions coupled capacitively or inductively to the network of coplanar waveguides. As we are at first only interested in the linear part of the Hamiltonian we only take the linear, inductive part of every Josephson junction into account. With this truncation every lumped element circuit can be described by a finite number of eigenfrequencies. The spectrum of the eigenmodes of the superconducting circuit as a function of these eigenfrequencies is the spectrum of the network of coplanar waveguides and the spectrum of the lumped element circuits where each degeneracy between the two is either lifted in an anti-crossing or not, depending on the symmetries of the setup [54, 53]. Apart from the anticrossings the eigenmode spectrum is well described by the standard quantum graph theory. Near the anticrossings we do get hybridized excitations of the waveguiding elements, the distributed elements, and

the wave scattering elements, the lumped elements. The formulation of quantum graph theory in terms of scattering matrices or transfer matrices is well suited to describe this situation. The flux function in the coplanar waveguides subject to the waveequation has two fundamental solutions: the forward- and backward propagating waves. therefore we can represent the flux function as a two component vector with the amplitudes of forward and backward propagating waves. In this formalism every linearized lumped element circuit can be represented as a two-by-two matrix which describes the scattering between forward- and backward propagating amplitudes to the left and right of the lumped element circuit. There is an intricate connection between the properties of these transfer matrices and the spectrum of the superconducting circuit given by the secular equation which has already been exploited to find the eigenmode spectrum of a coplanar waveguide resonator intersected by Josephson junctions [54].



# Bibliography

- [1] A. A. Abdumalikov, O. Astafiev, A. M. Zagoskin, Yu. A. Pashkin, Y. Nakamura, and J. S. Tsai. Electromagnetically Induced Transparency on a Single Artificial Atom. *Physical Review Letters*, 104(19):193601, May 2010.
- [2] P W Anderson and J M Rowell. Probable Observation of the Josephson Superconducting Tunneling Effect. *Phys. Rev. Lett.*, 10(6):230–232, 1963.
- [3] Markus Ansmann, H Wang, Radoslaw C Bialczak, Max Hofheinz, Erik Lucero, M Neeley, A D O’Connell, D Sank, M Weides, J Wenner, A N Cleland, and John M Martinis. Violation of Bell’s inequality in Josephson phase qubits. *Nature*, 461(7263):504–6, September 2009.
- [4] O Astafiev, A M Zagoskin, A A Abdumalikov, Yu A Pashkin, T Yamamoto, K Inomata, Y Nakamura, and J S Tsai. Resonance fluorescence of a single artificial atom. *Science (New York, N.Y.)*, 327(5967):840–3, February 2010.
- [5] N. Bergeal, R. Vijay, V. E. Manucharyan, I. Siddiqi, R. J. Schoelkopf, S. M. Girvin, and M. H. Devoret. Analog information processing at the quantum limit with a Josephson ring modulator. *Nature Physics*, 6(4):296–302, February 2010.
- [6] A J Berkley, H Xu, R C Ramos, M A Gubrud, F W Strauch, P R Johnson, J R Anderson, A J Dragt, C J Lobb, and F C Wellstood. Entangled macroscopic quantum States in two superconducting qubits. *Science*, 300:1548–1550, 2003.
- [7] Gregory Berkolaiko and Peter Kuchment. *Introduction to Quantum Graphs*. American Mathematical Soc., 2013.
- [8] Lev S. Bishop, J. M. Chow, Jens Koch, a. a. Houck, M. H. Devoret, E. Thuneberg, S. M. Girvin, and R. J. Schoelkopf. Nonlinear response of the vacuum Rabi resonance. *Nature Physics*, 5(2):105–109, December 2008.
- [9] Alexandre Blais, Ren-Shou Huang, Andreas Wallraff, S. M. Girvin, and R. J. Schoelkopf. Cavity quantum electrodynamics for superconducting electrical circuits: an architecture for quantum computation. *Physical Review A*, 69:14, February 2004.
- [10] Immanuel Bloch and Wilhelm Zwerger. Many-body physics with ultracold gases. *Reviews of Modern Physics*, 80(3):885–964, July 2008.
- [11] J. Bourassa, J. Gambetta, a. Abdumalikov, O. Astafiev, Y. Nakamura, and a. Blais. Ultrastrong coupling regime of cavity QED with phase-biased flux qubits. *Physical Review A*, 80(3):1–8, September 2009.

- [12] D. Bozyigit, C. Lang, L. Steffen, J. M. Fink, C. Eichler, M. Baur, R. Bianchetti, P. J. Leek, S. Filipp, M. P. da Silva, A. Blais, and A. Wallraff. Antibunching of microwave-frequency photons observed in correlation measurements using linear detectors. *Nature Physics*, 7(2):154–158, December 2010.
- [13] A.O Caldeira and A.J Leggett. Quantum tunnelling in a dissipative system. *Annals of Physics*, 149(2):374–456, September 1983.
- [14] I. Carusotto, D. Gerace, H. Tureci, S. De Liberato, C. Ciuti, and a. Imamoğlu. Fermionized Photons in an Array of Driven Dissipative Nonlinear Cavities. *Physical Review Letters*, 103(3):1–4, July 2009.
- [15] J. Cirac, P. Zoller, H. Kimble, and H. Mabuchi. Quantum State Transfer and Entanglement Distribution among Distant Nodes in a Quantum Network. *Physical Review Letters*, 78(16):3221–3224, April 1997.
- [16] John Clarke and Alex I. Braginski. *The SQUID Handbook: Fundamentals and Technology of SQUIDS and SQUID Systems, Volume I*. Wiley Online Library, 2005.
- [17] Frank Deppe, Matteo Mariani, E P Menzel, A Marx, S Saito, K Kakuyanagi, H Tanaka, T Meno, K Semba, H Takayanagi, E Solano, and R Gross. Two-photon probe of the Jaynes-Cummings model and controlled symmetry breaking in circuit QED. *Nature Physics*, 4(September), 2008.
- [18] Michel Devoret, John Martinis, and John Clarke. Measurements of Macroscopic Quantum Tunneling out of the Zero-Voltage State of a Current-Biased Josephson Junction. *Physical Review Letters*, 55(18):1908–1911, October 1985.
- [19] Michel H Devoret. Quantum Fluctuations in Electrical Circuits. In *Fluctuations quantiques Les Houches, Session LXIII, 27 juin-28 juillet 1995 = Quantum fluctuations*, pages 351–386. Elsevier,, Amsterdam ;;New York :, 1997.
- [20] L Dicarlo, M D Reed, L Sun, B R Johnson, J M Chow, J M Gambetta, L Frunzio, S M Girvin, M H Devoret, and R J Schoelkopf. Preparation and measurement of three-qubit entanglement in a superconducting circuit. *Nature*, 467(7315):574–8, September 2010.
- [21] R. Dicke. Coherence in Spontaneous Radiation Processes. *Physical Review*, 93(1):99–110, January 1954.
- [22] D. P. Divincenzo. *Topics in quantum computers*. Springer Netherlands, Dordrecht, 1997.
- [23] P D Drummond and D F Walls. Quantum theory of optical bistability. I. Nonlinear polarisability model. *Journal of Physics A: Mathematical and General*, 13(2):725–741, February 1980.
- [24] C. Eichler, C. Lang, J. M. Fink, J. Govenius, S. Filipp, and A. Wallraff. Observation of Entanglement between Itinerant Microwave Photons and a Superconducting Qubit. *Physical Review Letters*, 109(24):240501, December 2012.



- 
- [25] Shanhui Fan, Sükrü Kocabas, and Jung-Tsung Shen. Input-output formalism for few-photon transport in one-dimensional nanophotonic waveguides coupled to a qubit. *Physical Review A*, 82(6), December 2010.
- [26] David Ferguson, A. Houck, and Jens Koch. Symmetries and Collective Excitations in Large Superconducting Circuits. *Physical Review X*, 3(1):011003, January 2013.
- [27] Richard P. Feynman. Simulating physics with computers. *International Journal of Theoretical Physics*, 21(6-7):467–488, June 1982.
- [28] J M Fink, M Göppl, M Baur, R Bianchetti, P J Leek, a Blais, and a Wallraff. Climbing the Jaynes-Cummings ladder and observing its nonlinearity in a cavity QED system. *Nature*, 454(7202):315–8, July 2008.
- [29] a. Friedenauer, H. Schmitz, J. T. Glueckert, D. Porras, and T. Schaetz. Simulating a quantum magnet with trapped  $\text{Å}$  ions. *Nature Physics*, 4(10):757–761, July 2008.
- [30] JR Friedman, V Patel, W Chen, SK Tolpygo, and JE Lukens. Quantum superposition of distinct macroscopic states. *Nature*, 406(6791):43–6, July 2000.
- [31] Dario Gerace, Hakan E Türeci, Atac Imamoglu, Vittorio Giovannetti, and Rosario Fazio. The quantum-optical Josephson interferometer. *Nature Physics*, 5(4):281–284, 2009.
- [32] Sergey Gladchenko, David Olaya, Eva Dupont-Ferrier, Benoit Douçot, Lev B. Ioffe, and Michael E. Gershenson. Superconducting nanocircuits for topologically protected qubits. *Nature Physics*, 5(1):48–53, November 2008.
- [33] Lucia Hackermüller, Ulrich Schneider, Maria Moreno-Cardoner, Takuya Kitagawa, Thorsten Best, Sebastian Will, Eugene Demler, Ehud Altman, Immanuel Bloch, and Belén Paredes. Anomalous expansion of attractively interacting fermionic atoms in an optical lattice. *Science (New York, N.Y.)*, 327(5973):1621–4, March 2010.
- [34] M J Hartmann, F G S L Brandão, and M B Plenio. A polaritonic two-component Bose Hubbard model. *New Journal of Physics*, 10(3):033011, March 2008.
- [35] Michael Hartmann and Martin Plenio. Strong Photon Nonlinearities and Photonic Mott Insulators. *Physical Review Letters*, 99(10):1–4, September 2007.
- [36] Michael J. Hartmann. Polariton Crystallization in Driven Arrays of Lossy Nonlinear Resonators. *Physical Review Letters*, 104(11):1–4, March 2010.
- [37] Max Hofheinz, E M Weig, M Ansmann, Radoslaw C Bialczak, Erik Lucero, M Neeley, a D O’Connell, H Wang, John M Martinis, and a N Cleland. Generation of Fock states in a superconducting quantum circuit. *Nature*, 454(7202):310–4, July 2008.
- [38] a a Houck, D I Schuster, J M Gambetta, J a Schreier, B R Johnson, J M Chow, L Frunzio, J Majer, M H Devoret, S M Girvin, and R J Schoelkopf. Generating single microwave photons in a circuit. *Nature*, 449(7160):328–31, September 2007.

- [39] Andrew a. Houck, Hakan E. Türeci, and Jens Koch. On-chip quantum simulation with superconducting circuits. *Nature Physics*, 8(4):292–299, April 2012.
- [40] Jiasen Jin, Davide Rossini, Rosario Fazio, Martin Leib, and Michael J. Hartmann. Photon Solid Phases in Driven Arrays of Nonlinearly Coupled Cavities. *Physical Review Letters*, 110(16):163605, April 2013.
- [41] Jiasen Jin, Davide Rossini, Martin Leib, Michael J. Hartmann, and Rosario Fazio. Steady-state phase diagram of a driven QED-cavity array with cross-Kerr nonlinearities. *Physical Review A*, 90(2):023827, August 2014.
- [42] J. Johansson, G. Johansson, C. Wilson, and Franco Nori. Dynamical Casimir Effect in a Superconducting Coplanar Waveguide. *Physical Review Letters*, 103(14):147003, September 2009.
- [43] BR Johnson, MD Reed, and AA Houck. Quantum non-demolition detection of single microwave photons in a circuit. *Nature Physics*, pages 1–5, 2010.
- [44] M W Johnson, M H S Amin, S Gildert, T Lanting, F Hamze, N Dickson, R Harris, A J Berkley, J Johansson, P Bunyk, E M Chapple, C Enderud, J P Hilton, K Karimi, E Ladizinsky, N Ladizinsky, T Oh, I Perminov, C Rich, M C Thom, E Tolkacheva, C J S Truncik, S Uchaikin, J Wang, B Wilson, and G Rose. Quantum annealing with manufactured spins. *Nature*, 473(7346):194–8, May 2011.
- [45] B.D. Josephson. Possible new effects in superconductive tunnelling. *Physics Letters*, 1(7):251–253, July 1962.
- [46] Alexei Kitaev. Anyons in an exactly solved model and beyond. *Annals of Physics*, 321(1):2–111, January 2006.
- [47] Jens Koch, Andrew Houck, Karyn Le Hur, and S. Girvin. Time-reversal-symmetry breaking in circuit-QED-based photon lattices. *Physical Review A*, 82(4):1–18, October 2010.
- [48] Jens Koch, Terri Yu, Jay Gambetta, a. Houck, D. Schuster, J. Majer, Alexandre Blais, M. Devoret, S. Girvin, and R. Schoelkopf. Charge-insensitive qubit design derived from the Cooper pair box. *Physical Review A*, 76(4):1–19, October 2007.
- [49] Y. Kubo, F. R. Ong, P. Bertet, D. Vion, V. Jacques, D. Zheng, A. Dréau, J.-F. Roch, A. Auffeves, F. Jelezko, J. Wrachtrup, M. F. Barthe, P. Bergonzo, and D. Esteve. Strong Coupling of a Spin Ensemble to a Superconducting Resonator. *Physical Review Letters*, 105(14):140502, September 2010.
- [50] Tony E. Lee, H. Häffner, and M. C. Cross. Antiferromagnetic phase transition in a nonequilibrium lattice of Rydberg atoms. *Physical Review A*, 84(3):031402, September 2011.
- [51] A J Leggett. Testing the limits of quantum mechanics: motivation, state of play, prospects. *Journal of Physics: Condensed Matter*, 14(15):R415–R451, April 2002.

- 
- [52] M Leib, F Deppe, A Marx, R Gross, and M J Hartmann. Networks of nonlinear superconducting transmission line resonators. *New Journal of Physics*, 14(7):075024, July 2012.
- [53] M Leib, F Deppe, A Marx, R Gross, and M J Hartmann. Networks of nonlinear superconducting transmission line resonators. *New Journal of Physics*, 14(7):75024, 2012.
- [54] Martin Leib and Michael J. Hartmann. Synchronized Switching in a Josephson Junction Crystal. *Physical Review Letters*, 112(22):223603, June 2014.
- [55] A. Lupascu, S. Saito, T. Picot, P. C. de Groot, C. J. P. M. Harmans, and J. E. Mooij. Quantum non-demolition measurement of a superconducting two-level system. *Nature Physics*, 3(2):119–125, January 2007.
- [56] J Majer, J M Chow, J M Gambetta, Jens Koch, B R Johnson, J a Schreier, L Frunzio, D I Schuster, a a Houck, a Wallraff, a Blais, M H Devoret, S M Girvin, and R J Schoelkopf. Coupling superconducting qubits via a cavity bus. *Nature*, 449(7161):443–7, September 2007.
- [57] J B Majer, F G Paauw, A C J Ter Haar, C J P M Harmans, and J E Mooij. Spectroscopy on two coupled superconducting flux qubits. *Physical review letters*, 94:090501, 2005.
- [58] Vladimir E Manucharyan, Jens Koch, Leonid I Glazman, and Michel H Devoret. Fluxonium: single cooper-pair circuit free of charge offsets. *Science (New York, N.Y.)*, 326(5949):113–6, October 2009.
- [59] D Marcos, A Tomadin, S Diehl, and P Rabl. Photon condensation in circuit quantum electrodynamics by engineered dissipation. *New Journal of Physics*, 14(5):055005, May 2012.
- [60] Matteo Mariani, Frank Deppe, a. Marx, R. Gross, F. Wilhelm, and E. Solano. Two-resonator circuit quantum electrodynamics: A superconducting quantum switch. *Physical Review B*, 78(10):1–22, September 2008.
- [61] John Martinis, S. Nam, J. Aumentado, and C. Urbina. Rabi Oscillations in a Large Josephson-Junction Qubit. *Physical Review Letters*, 89(11):9–12, August 2002.
- [62] John M. Martinis and A. Megrant. UCSB final report for the CSQ program: Review of decoherence and materials physics for superconducting qubits. October 2014.
- [63] E. Menzel, F. Deppe, M. Mariani, M. Araque Caballero, a. Baust, T. Niemczyk, E. Hoffmann, a. Marx, E. Solano, and R. Gross. Dual-Path State Reconstruction Scheme for Propagating Quantum Microwaves and Detector Noise Tomography. *Physical Review Letters*, 105(10):1–4, August 2010.
- [64] VV Mikhailov. Ordering of some boson operator functions. *Journal of Physics A: Mathematical and General*, 3817, 1983.
- [65] Y. Nakamura, C. Chen, and J. Tsai. Spectroscopy of Energy-Level Splitting between Two Macroscopic Quantum States of Charge Coherently Superposed by Josephson Coupling. *Physical Review Letters*, 79(12):2328–2331, September 1997.

- [66] Y Nakamura, Yu A Pashkin, and J S Tsai. letters to nature Coherent control of macroscopic quantum states in a single-Cooper-pair box. 398(April):0–2, 1999.
- [67] T. Niemczyk, F. Deppe, H. Huebl, E. P. Menzel, F. Hocke, M. J. Schwarz, J. J. Garcia-Ripoll, D. Zueco, T. Hümmer, E. Solano, a. Marx, and R. Gross. Circuit quantum electrodynamics in the ultrastrong-coupling regime. *Nature Physics*, 6(10):772–776, July 2010.
- [68] Simon E. Nigg, Hanhee Paik, Brian Vlastakis, Gerhard Kirchmair, S. Shankar, Luigi Frunzio, M. H. Devoret, R. J. Schoelkopf, and S. M. Girvin. Black-Box Superconducting Circuit Quantization. *Physical Review Letters*, 108(24):240502, June 2012.
- [69] A Nunnenkamp, Jens Koch, and S M Girvin. Synthetic gauge fields and homodyne transmission in Jaynes-Cummings lattices. *New Journal of Physics*, 13(9):095008, September 2011.
- [70] A D O’Connell, M Hofheinz, M Ansmann, Radoslaw C Bialczak, M Lenander, Erik Lucero, M Neeley, D Sank, H Wang, M Weides, J Wenner, John M Martinis, and A N Cleland. Quantum ground state and single-phonon control of a mechanical resonator. *Nature*, 464(7289):697–703, April 2010.
- [71] Hanhee Paik, D. I. Schuster, Lev S. Bishop, G. Kirchmair, G. Catelani, A. P. Sears, B. R. Johnson, M. J. Reagor, L. Frunzio, L. I. Glazman, S. M. Girvin, M. H. Devoret, and R. J. Schoelkopf. Observation of High Coherence in Josephson Junction Qubits Measured in a Three-Dimensional Circuit QED Architecture. *Physical Review Letters*, 107(24):240501, December 2011.
- [72] Yu A Pashkin, T Yamamoto, O Astafiev, Y Nakamura, D V Averin, and J S Tsai. Quantum oscillations in two coupled charge qubits. *Nature*, 421:823–826, 2003.
- [73] J H Plantenberg, P C de Groot, C J P M Harmans, and J E Mooij. Demonstration of controlled-NOT quantum gates on a pair of superconducting quantum bits. *Nature*, 447(7146):836–9, June 2007.
- [74] B. Plourde, J. Zhang, K. Whaley, F. Wilhelm, T. Robertson, T. Hime, S. Linzen, P. Reichardt, C.-E. Wu, and John Clarke. Entangling flux qubits with a bipolar dynamic inductance. *Physical Review B*, 70(14):140501, October 2004.
- [75] David M. Pozar. *Microwave Engineering*. Wiley, 2004.
- [76] Georg M. Reuther, David Zueco, Frank Deppe, Elisabeth Hoffmann, Edwin P. Menzel, Thomas Weiß l, Matteo Mariani, Sigmund Kohler, Achim Marx, Enrique Solano, Rudolf Gross, and Peter Hänggi. Two-resonator circuit quantum electrodynamics: Dissipative theory. *Physical Review B*, 81(14):1–16, April 2010.
- [77] D. Ristè, S. Poletto, M. Z. Huang, A. Bruno, V. Vesterinen, O. P. Saira, and L. DiCarlo. Detecting bit-flip errors in a logical qubit using stabilizer measurements. November 2014.

- 
- [78] S. Schmidt, D. Gerace, A. A. Houck, G. Blatter, and H. E. Türeci. Nonequilibrium delocalization-localization transition of photons in circuit quantum electrodynamics. *Physical Review B*, 82(10):100507, September 2010.
- [79] D. I. Schuster, A. P. Sears, E. Ginossar, L. DiCarlo, L. Frunzio, J. J. L. Morton, H. Wu, G. A. D. Briggs, B. B. Buckley, D. D. Awschalom, and R. J. Schoelkopf. High-Cooperativity Coupling of Electron-Spin Ensembles to Superconducting Cavities. *Physical Review Letters*, 105(14):140501, September 2010.
- [80] I. Siddiqi, R. Vijay, F. Pierre, C. Wilson, L. Frunzio, M. Metcalfe, C. Rigetti, R. Schoelkopf, M. Devoret, D. Vion, and D. Esteve. Direct Observation of Dynamical Bifurcation between Two Driven Oscillation States of a Josephson Junction. *Physical Review Letters*, 94(2):027005, January 2005.
- [81] Mika Sillanpää, Jian Li, Katarina Cicak, Fabio Altomare, Jae Park, Raymond Simmonds, G. Paraoanu, and Pertti Hakonen. Autler-Townes Effect in a Superconducting Three-Level System. *Physical Review Letters*, 103(19):193601, November 2009.
- [82] Mika A Sillanpää, Jae I Park, and Raymond W Simmonds. Coherent quantum state storage and transfer between two phase qubits via a resonant cavity. *Nature*, 449:438–442, 2007.
- [83] A. Tomadin, V. Giovannetti, R. Fazio, D. Gerace, I. Carusotto, H. E. Türeci, and A. Imamoglu. Signatures of the superfluid-insulator phase transition in laser-driven dissipative nonlinear cavity arrays. *Physical Review A*, 81(6):061801, June 2010.
- [84] D. L. Underwood, W. E. Shanks, Jens Koch, and A. A. Houck. Low-disorder microwave cavity lattices for quantum simulation with photons. *Physical Review A*, 86(2):023837, August 2012.
- [85] C H van der Wal, A C ter Haar, F K Wilhelm, R N Schouten, C J Harmans, T P Orlando, S Lloyd, and J E Mooij. Quantum superposition of macroscopic persistent-current states. *Science (New York, N.Y.)*, 290(5492):773–777, 2000.
- [86] D Vion, A Aassime, A Cottet, P Joyez, H Pothier, C Urbina, D Esteve, and M H Devoret. Manipulating the quantum state of an electrical circuit. *Science (New York, N.Y.)*, 296(5569):886–9, May 2002.
- [87] Richard Voss and Richard Webb. Macroscopic Quantum Tunneling in 1- $\mu\text{m}$  Nb Josephson Junctions. *Physical Review Letters*, 47(4):265–268, July 1981.
- [88] A. Wallraff, D. Schuster, A. Blais, L. Frunzio, J. Majer, M. Devoret, S. Girvin, and R. Schoelkopf. Approaching Unit Visibility for Control of a Superconducting Qubit with Dispersive Readout. *Physical Review Letters*, 95(6):060501, August 2005.
- [89] A Wallraff, D I Schuster, A Blais, L Frunzio, J Majer, S Kumar, S M Girvin, and R J Schoelkopf. Strong coupling of a single photon to a superconducting qubit using circuit quantum electrodynamics. *Nature*, 431(September):162–167, 2004.

- [90] C M Wilson, G Johansson, A Pourkabirian, M Simoen, J R Johansson, T Duty, F Nori, and P Delsing. Observation of the dynamical Casimir effect in a superconducting circuit. *Nature*, 479(7373):376–9, November 2011.
- [91] J. You and Franco Nori. Quantum information processing with superconducting qubits in a microwave field. *Physical Review B*, 68(6):064509, August 2003.
- [92] David Zueco, Juan J. Mazo, Enrique Solano, and Juan José García-Ripoll. Microwave photonics with Josephson junction arrays: Negative refraction index and entanglement through disorder. *Physical Review B*, 86(2):024503, July 2012.